Optical Characterization of Doped Zinc Oxide Nanowires

by

Faezeh Mohammadbeigi

M.Sc., Shahrood University of Technology, 2010
B.Sc., Kahjeh Nasir Toosi University of Technology, 2007

Dissertation Submitted in Partial Fulfillment of the
Requirements for the Degree of
Doctor of Philosophy

in the
Department of Physics
Faculty of Science

SIMON FRASER UNIVERSITY
Spring 2017

Approval

Name: **Faezeh Mohammadbeigi**

Degree: **Doctor of Philosophy (Physics)**

Title: ***Optical Characterization of Doped Zinc Oxide Nanowires***

Examining Committee: **Chair:** Stephanie Simmons
Assistant Professor

Simon Watkins
Senior Supervisor
Professor
Department of Physics _____

Karen Kavanagh
Supervisor
Professor
Department of Physics _____

Steve Dodge
Supervisor
Associate Professor
Department of Physics _____

Gary Leach
Internal Examiner
Associate Professor
Department of Chemistry _____

Martin O. Henry
External Examiner
Professor
Department of Physical Sciences
Dublin City University _____

Date Defended: 24 Jan 2017

Abstract

ZnO is a promising semiconductor material with a direct band gap energy of 3.3 eV which makes it a good candidate for UV and visible range light emitting devices. The earth abundance of ZnO coupled with the use of lower toxicity precursors such as oxygen make it highly desirable from an industrial point of view. Metalorganic chemical vapor epitaxy (MOVPE) provides the possibility of industrial scale growth of ZnO, with very fine control of impurity dopants. Despite the vast recent literature on ZnO, there are very few studies of systematic intentional doping. ZnO nanowires (NWs) can be grown easily on various substrates with high crystalline quality and low defect densities and tend to exhibit reduced substrate induced strain. This enables us to perform careful spectroscopic analysis of impurity related optical transitions and identify the physical nature of various dopant species. A detailed study of low temperature photoluminescence (PL) transitions in doped ZnO NWs, thin films, and bulk crystals grown by MOVPE and chemical vapour transport (CVT) methods is presented. The standard group III donors were first investigated. Donor bound exciton (D^0X) transitions previously assigned to Ga, Al, and In were confirmed in intentionally doped samples. Group IV dopants such as carbon, and tin are interesting since they can act in principle as double donors or double acceptors. We report four new shallow D0X transitions (Z-lines), at 3360.8 (Z_1), 3361.2 (Z_2), 3361.7 (Z_3) and 3361.9 (Z_4) meV, which can be greatly enhanced by co-doping with carbon tetrachloride and hydrogen. These shallow donors appear to be due to carbon impurities complexed with other unknown defects in four distinct configurations. Carbon-doped samples also exhibit two distinct acceptors with binding energies of 133 $\pm$ 5 and 181 $\pm$ 5 meV. Doping concentration and temperature dependent PL studies of unintentionally doped and Sn-doped ZnO single crystals confirmed emission from the I_{10} D^0X transition which was recently proven to contain Sn on a Zn site. Sb-doped ZnO NWs were grown in an attempt to produce p-type material as reported by some groups. Our PL studies including Magneto PL, have shown that rather than p-doped material, the addition of small amounts of Sb-dopant resulted in a new PL transition at 3364.3 meV, which turns out to be the shallowest D^0X transition so far observed in ZnO.
Keywords: Zinc oxide, nanowires, photoluminescence, doping, donors, acceptors

Dedication

This thesis is dedicated to my family.

Acknowledgements

I would like to thank my supervisor, Prof. Simon Watkins, for providing me with the opportunity of doing research in his lab. I am grateful for all his guidance, useful discussions, valuable advice and support he gave me to work on my research.
I am also thankful to my supervisory committee members, Profs. Karen Kavanagh and Steve Dodge for all of their useful discussions and advice in my committee meetings.
I am thankful to my collaborators, Prof. Axel Hoffmann, Dr. Markus Wagner, Dr. Gordon Callsen and in particular, PhD candidate Thomas Kure, who helped me for part of my research in Germany at Technical University of Berlin.
I am grateful to the faculty and staff of Physics Department, Dr. Patricia Mooney, Dr. Sarah Johnson, Rose Evans, Ayako Nagassawa, Stephen Flach for their support and making it a good research environment for graduate students.
I want to thank all my labmates and friends particularly Dorna and Shima for their support during these five amazing and unforgettable years of my life at Simon Fraser University.
Last and for most, I want to thank my family for their endless love and support.

Table of Contents

List of Figures

List of Tables

Abbreviations

A^0X	Acceptor bound exciton
BX	Bound exciton
B	Magnetic field
CVT	Chemical vapor transport
D^0X	Neutral donor bound exciton
D^+X	Ionized donor bound exciton
DAP	donor-acceptor-pair
e,A^0	Free-to-bound transition
EMA	Effective mass approximation
FX	Free exciton
FWHM	Full width at half maximum
$\mathbf{g}_e$	Electron g factor
$\mathbf{g}_h$	Hole g factor
$\mathbf{I}_x$	Neutral bound exciton label (x is 6,7,8,9,10)
$\mathbf{I}_x^+$	Ionized bound exciton label (x is 6,7,8,9,10)
LED	Light emitting diode
LO	Longitudinal optical
MPL	Magneto photoluminescence
MOVPE	Metalorganic vapor phase epitaxy
NW	Nanowire
PL	Photoluminescence
PMT	Photomultiplier tube
SEM	Scanning electron microscopy

TES	Two electron satellite
UV	Ultraviolet

List of publications

1. Mohammadbeigi, F., Kure, T., Callsen, G., Kumar, E. S., M. Wagner, Hoffmann, A. and Watkins, S. P., "Acceptor related photoluminescence from carbon doped ZnO grown with MOCVD method", Accepted at Semicond. Sci. Technol. (2017)

2. Kumar, E. S., Mohammadbeigi, F., Boatner, L. and Watkins, S. P., "High-resolution photoluminescence spectroscopy of Sn-doped ZnO single crystals", J. of Lumin., 176, 47-51 (2016)

3. Mohammadbeigi, F., Kumar, E. S., Alagha, S., Anderson, I., and Watkins, S. P., "Carbon related donor bound exciton transitions in ZnO nanowires", J. Appl. Phys., 116(5), 053516 (2014)

4. Kumar, E. S., Mohammadbeigi, F., Alagha, S., Deng, Z. W., Anderson, I. P., Wintschel, T. and Watkins, S. P.,"Optical evidence for donor behavior of Sb in ZnO nanowires" Appl. Phys. Lett., 102(13), 132105 (2013)

5. Kumar, E. S., Anderson, I. P., Deng, Z., Mohammadbeigi, F., Wintschel, T., Huang, D. and Watkins, S. P., "Effect of group-III donors on high-resolution photoluminescence and morphology of ZnO nanowires grown by metalorganic vapour phase epitaxy", Semicond. Sci. Technol., 28(4), 045014 (2013)

Chapter 1

Introduction

The wide-bandgap semiconductor ZnO is a material with great potential for optoelectronic devices such as blue and ultraviolet light-emitting diodes (LEDs) and laser diodes. Its transparency to visible light makes it an excellent choice for transparent electrodes in solar cells. It is made from earth-abundant non-toxic materials and has the potential to replace gallium nitride, the current preferred material for UV and near-UV solid state light emitters. Size reduction in nanotechnology introduces new optical and electrical properties which lead to surface and quantum confinement effects. The study of one dimensional (1D) materials has become a leading research area in nanoscience and nanotechnology. A major advantage for ZnO is that nanostructures, such as nanowires (NWs) and nanowalls, can be easily grown on lattice-mismatched substrates. Nanowires grown on lattice-mismatched substrates have lower defect densities and higher crystalline quality compared with thin film layers grown on mismatched substrates due to the relaxation of internal stress [2].

The understanding of impurities and defects is critical to enable current and future semiconductor devices. Undoped ZnO is usually n-type and it is difficult to make it p-type because of the difficulty to form shallow acceptor levels, which is the main impediment to the commercialization of ZnO semiconductor devices. Although this material has been studied over fifty years [3, 4], many important questions remain, such as what is the main source of the residual n-type conductivity and what is the underlying cause of the difficulty of p-type doping.

In this chapter, we will provide an overview of ZnO and describe its crystalline and electronic-band structure. We will also give a general view on the low-temperature luminescence of ZnO single crystals.

1.1 Overview of ZnO

ZnO is a binary compound semiconductor comprising elements from group-II_b and group-VI of the periodic table. Compared to GaN, which is a III-V compound and already widely commercialized for LED devices, ZnO has interesting properties. They both crystallize in the wurtzite structure and have similar bandgaps at room temperature (GaN: 3.4 eV and ZnO: 3.3 eV) [5]. However, comparing exciton binding energies (60 meV in ZnO [6] compared to 25 meV in GaN [7]) and the cost of creating high-quality material, ZnO is potentially a better candidate for UV-blue light emitters at room temperature. ZnO can easily be doped n-type but it is difficult to make it p-type. The reasons for this are still the source of controversy. Although p-doping is the main impediment to make ZnO devices, the origin of the donors in nominally-undoped ZnO is still unresolved. For example, the cause of the residual n-type conductivity observed in most ZnO material has been attributed to hydrogen donors, as well as Zn interstitials [8, 9]. Fig. 1.1 shows the position of Zn and O (highlighted in pink) in the periodic table of elements along with the dopants that we have studied throughout this work. Impurities that are studied in this work and previously expected to act as acceptors (such as Sb) and donors (such as Al, Ga, In, C and Sn) are highlighted in blue.

		III	IV	V	VI
		B	C	N	O
I_B	II_B	Al	Si	P	S
Cu	Zn	Ga	Ge	As	Se
Ag	Cd	In	Sn	Sb	Te
Au	Hg	Tl	Pb	Bi	Po

Figure 1.1: The position of Zn and O in the periodic table of elements and highlighted chemical dopants from group-III, IV and V investigated in this work.

1.2 Defects in ZnO

Defects and impurities can form shallow donor or acceptor states and affect the optical spectrum near the bandgap. Intrinsic defects such as interstitials, vacancies, dislocations and stacking faults can cause undesired radiative and non-radiative recombination and result in the appearance of additional emission lines. Well-studied intrinsic defects in ZnO include Zn and O interstitials, Zn_i and O_i, and Zn and O vacancies, V_{Zn} and V_O. Janotti and van de Walle [10] have argued that V_O acts as a deep donor in ZnO with a binding energy of ∼1.0 eV and could be the dominant compensation center in p-type ZnO. Look et al. [8] suggested that Zn_i is the dominant shallow donor in ZnO and suggest that the PL transition named I_{3a} is related to it [11, 12].

Extrinsic defects in ZnO can be produced intentionally or unintentionally during the growth process. The Zn site is often the substitutional site for numerous impurities including group-III elements like Al, Ga and In. These behave as traditional semiconductor donors in which the extra valence electron is contributed to the conduction band at room temperature. On simple valence electron arguments, one would expect to obtain acceptors if group-V impurities substitute on O sites. However, previous studies [13–15] have shown that As and Sb occupy Zn sites. This was attributed to the large cost in strain energy of placing these large group-V elements on the oxygen sublattice. Nitrogen is thought to occupy the O site and has been widely investigated as a candidate for p-type doping in ZnO, since its ionic radius is similar to that of oxygen [16–19]. However theoretical calculations have predicted a very large acceptor binding energy for substitutional nitrogen on the ZnO lattice [20]. Despite several reports of p-type ZnO, the reproducibility and stability of these results is under question [3].

1.3 Crystal structure and electronic band structure of ZnO

ZnO crystallizes in the wurtzite structure as shown in Fig. 1.2. This is a hexagonal lattice with lattice parameters a = 3.2495 Å and c = 5.2062 Å [21]. Each Zn ion in the lattice is surrounded by a tetrahedron of O ions, and vice-versa. ZnO has polar surfaces which are the result of positively charged Zn^{2+} and negatively charged O^{2-} ions in planes perpendicular to the c-axis. The centers of positive and negative charges in ZnO do not overlap exactly, which leads to polarization along the c-axis. The c-axis and c-plane are called the polar

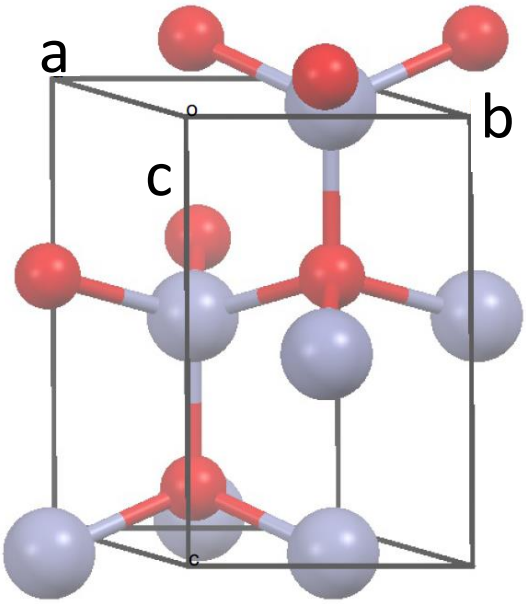

Figure 1.2: Wurtzite structure of ZnO.

axis and polar surface, respectively. If the ZnO crystals grow along the c axis, two different polar surfaces will be formed at the end of the crystal as a result of the termination of the structure and they are either Zn or O terminated surfaces. In the literature the (0001) c-plane is called the Zn-face, while the $(000\bar{1})$ c-plane is called the O-face.

ZnO is a direct bandgap semiconductor with a bandgap energy of 3.3 eV at room temperature [22]. The conduction band is generated from the 4s electrons of Zn atoms with s-like character and the valence band from 2p electrons of the oxygen atoms with p-like character. Having zero orbital momentum (L = 0), the conduction band is not affected by the spin-orbit interaction. On the other hand, the valence band, with a nonzero orbital momentum (L = 1) is affected by the spin-orbit (Δ_{so}) interaction and crystal field (Δ_{cf}). In the wurtzite structure of ZnO, the crystal field causes the splitting of the valence band and lifts the degeneracy between p_z-like states and the p_{xy}-like ones. The spin-orbit interaction is relatively weak in this material compared with other common direct gap materials like GaAs because of the relatively low atomic number of the anion atoms (oxygen) responsible for the valence band states.

The order of the valence-band splitting in ZnO by the crystal field and spin-orbit coupling has been under debate for decades [23–25] and recently was determined clearly [24, 26].

Group theory is used to describe the symmetry of the electron's wavefunctions in each band [27, 28]. Fig. 1.3 shows a schematic sketch of the ZnO band structure. The valence bands are labeled A (Γ_7), B (Γ_9) and C (Γ_7) [29]. The combined effect of the crystal field

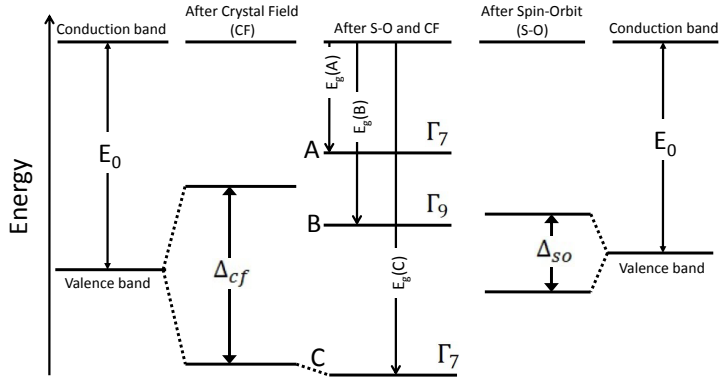

Figure 1.3: Schematic energy level diagram of the valence band splitting due to crystal field and spin-orbit interaction.

splitting energy of 41.7 meV and the spin orbit splitting of -8 meV results in a complete lifting of the degeneracy of the valence band as indicated in Fig. 1.3. The energy separation between the A and B valence bands and B and C valence bands are 4.9 and 43.7 meV, respectively [23]. It should be noted that the spin-orbit splitting in ZnO is different from the A-B band splitting [29].

1.4 Luminescence processes in ZnO

Because of the direct gap nature of ZnO, crystal momentum is conserved after electron-hole recombination without the need for a phonon. Optical emission can take place in three steps: i) absorption of an above-bandgap photon and creation of an electron-hole pair, ii) thermalization of the electron-hole pair to the conduction band minima and valence band maxima, respectively and iii) emission of a photon at or below the bandgap energy. The light emission is called photoluminescence (PL). PL is a nondestructive tool which enables us to directly probe a semiconductor's band structure and observe impurity-related emission lines. ZnO has a variety of different luminescence lines in the visible and near UV range, from 2.0 to 3.45 eV. In the following section an introductory overview of different PL emission processes in ZnO is provided.

1.4.1 Free excitons

In high-purity, high-crystallinity semiconductors, photoexcited electron-hole pairs feel a Coulomb interaction which can make them bind together to form a quasi-particle called a free exciton (FX). Absorption and emission due to FX are so-called intrinsic optical transitions as opposed to impurity-related or extrinsic transitions. The exciton is conceptually similar to the hydrogen atom. If we consider electrons and holes as point charges with effective masses, m_e^* and m_h^*, and taking into account the dielectric constant of the crystal, then a simple modified Bohr model of the hydrogen atom can be applied where FX bound states form just below the continuum band, as shown in the Fig. 1.4. This approach uses the so-called effective mass approximation (EMA) in which the effect of the crystal potential on an individual electron is incorporated by giving it an effective mass and a charge that is screened by the dielectric constant of the bulk crystal. The R_y^* in Eq. 1.1 is the effective Rydberg energy, which is modified by the relative dielectric constant ε_r and the reduced FX effective mass $\mu = [(m_e^*)^{-1} + (m_h^*)^{-1}]^{-1}$ and, corresponds to the exciton ground state (n = 1). The kinetic energy of a free exciton can be separated into two parts: the center of mass part due to its translational motion and a hydrogen-like part describing the relative motion of electron and hole. Then we have [27]

$$E_{FX}(n, K) = E_g + \frac{\hbar^2 K^2}{2M} - \frac{R_y^*}{n^2} \qquad R_y^* = \frac{-13.6(eV)}{\varepsilon_r^2}\frac{\mu}{m_0}, \tag{1.1}$$

where $M = m_e^* + m_h^*$ is the exciton effective mass, $\mathbf{K}$ is the wavevector of the exciton, E_g is the bandgap energy at $k = 0$, n is the principle quantum number.

Usually, it is easier to observe free excitons in optical transitions at low temperatures. However, in ZnO, because of the very large exciton binding energy, FX transitions can be observed up to room temperature. The sample quality is also very important to observe free excitons i.e. low impurity concentrations are needed.

Fig. 1.4 illustrates the typical energy dispersion of free excitons. In ZnO, different exciton states can be formed depending on which valence band (A, B and C) the hole is coming from. According to group theory, the ground state symmetry of the intrinsic exciton (which has a hole from the Γ_7 valence band and an electron from the Γ_7 conduction band) can be found from the product of group representations of the corresponding band symmetries as [27, 29]

$$\Gamma_7 \otimes \Gamma_7 = \Gamma_5 \oplus \Gamma_1 \oplus \Gamma_2 \tag{1.2}$$

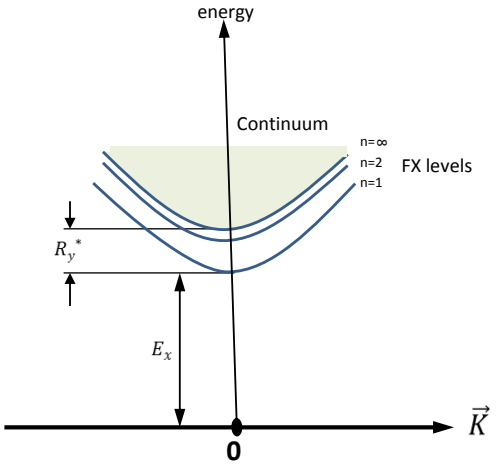

Figure 1.4: Energy dispersion spectrum of free exciton.

Thus, three exciton states are expected, with symmetries Γ_1, Γ_2 and Γ_5. The Γ_1 and Γ_2 states are believed to be accidentally degenerate, since no evidence of any splitting between them has been reported in ZnO [29]. There is a separation between the $\Gamma_{1,2}$ and Γ_5 states due to the different alignment of the electron and hole spins. In the case of the $\Gamma_{1,2}$ excitons, the spins are aligned parallel, whereas in the case of the Γ_5 exciton, the spins are anti-parallel. At the center of the Brillouin zone, recombination of Γ_5 and Γ_1 excitons is dipole-allowed with emission polarization perpendicular ($E \perp c$) and parallel ($E \parallel c$) to the crystallographic c-axis, respectively, while the Γ_2 exciton is dipole-forbidden and cannot be detected optically without an external perturbation like an applied magnetic field [29].

1.4.2 Bound-exciton transitions

At low temperatures, excitons may become bound to impurity defects in semiconductors, losing some of their energy in the process. Bound-exciton (BX) transitions can be observed by PL spectroscopy and are typically much sharper than free-excitons due to their localized atomic-like nature. The energy difference between BX and FX transitions defines the localization energy, E_{loc} of a given BX. BX have small localization energies (15-20 meV) and typically delocalize at temperatures above ∼50 K.

ZnO is usually n-type since the dominant impurities are donors. At low temperatures excitons can bind to these donor impurities and form neutral donor-bound excitons (D^0X). This is analogous to a hydrogen molecule except for the different binding energies due to

the much smaller hole mass compared to that of the proton. Excitons can also bind to ionized impurities, resulting in ionized donor-bound excitons (D^+X). They are the simplest bound-exciton system, consisting of an electron and a hole bound to an ionized donor. This system is analogous to a hydrogen molecular ion and has one electron and two positively charged particles. D^+Xs have small localization energies (a few meV) and they disappear quickly as the temperature of the sample is increased. The appearance of D^+X at low temperatures suggests the presence of residual acceptors that are partially compensating the donors. Fig. 1.5 shows schematic diagrams of the physical process of PL transitions for neutral and ionized donor-bound excitons.

In addition to D^0X and D^+X, an exciton can in principle also bind to a neutral acceptor forming the acceptor-bound exciton (A^0X). The energy position of the A^0X transitions in ZnO are suggested to be in the range of 16 to 25 meV for an acceptor binding energy of 165 meV [30]. There have been a few reports about A^0X transitions in ZnO [31–33]. However, none of these has been proven by detailed spectroscopic measurements, and most were later shown to be due to D^0X transitions. It is worth noting that the very closely related material GaN has a well documented A^0X due to Mg acceptors.

Several sharp impurity-related transitions have been identified in the near bandgap PL

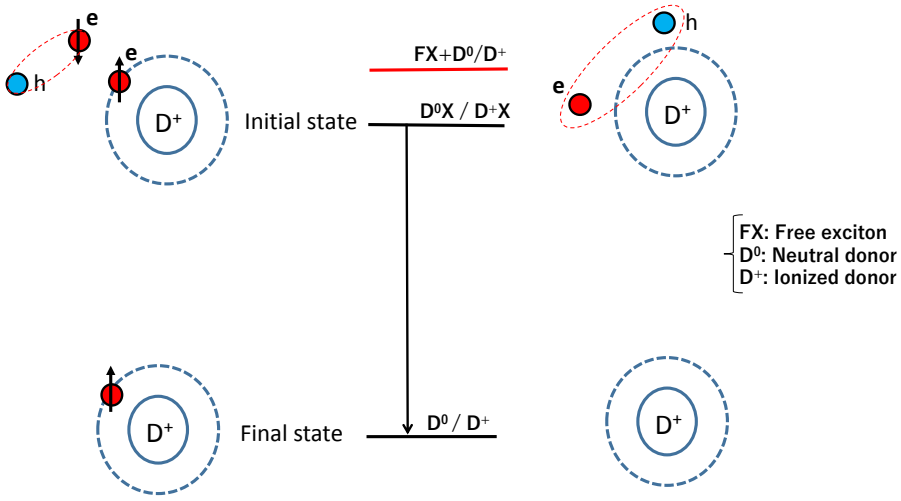

Figure 1.5: Schematic diagrams of the physical processes of PL transitions for neutral and ionized donor-bound excitons.

spectrum of ZnO. Reynolds et al. [34] established a labeling for these transitions from I_1 to I_{10}, where smaller indices are related to smaller localization energies. However, one must

read this early literature with care, since several of the lines were wrongly identified as A^0X, and others were wrongly identified as D^0X rather than D^+X.

Meyer et al. [23] studied these transitions in detail for ZnO single crystals and identified the origin of many of them. In particular, they were able to clarify the identity of the D^0X and D^+X transitions for the primary group-III donors. Muller et al. [35] identified In D^0X transition (I_9, 3356.8 meV) based on radioactive isotope implantation measurements in ZnO single crystals. Johnston et al. [13] reported PL measurements on ZnO implanted with radioactive isotopes of Ga and confirmed the Ga D^0X (I_8, 3359.9 meV) transitions in the PL spectrum. Based on implantation studies of Schilling et al. [36] and their successive annealing experiments, the Al D^0X transition (I_6, 3360.9 meV) increased in intensity and was strongest in samples with Al concentrations above 9 $\times 10^{16}$ cm^{-3}.
At temperatures about 4 K or lower, D^0X transitions involve holes from the lowest energy hole band, i.e. the A-valence band, however at higher energies excitons containing excited holes from the B-valence band can also form and are referred to as D^0X^B. These transitions occur 4.9 meV above their corresponding D^0X^A transition [23].

1.4.3 TES transitions and Haynes rule

When an exciton bound to a donor impurity recombines, the electron of the remaining donor can be in its ground state or be left in an excited hydrogenic state e.g. $2s$, $2p$, etc. and give rise to the so-called two-electron-satellite (TES) emission. The TES transition is red-shifted from the primary D^0X recombination line by the energy difference between the relevant donor excited state and the 1s level energy. Fig. 1.6 shows a schematic diagram of this process.

The EMA donor binding energy in ZnO is given by

$$R_y^*(\text{Donor}) = 13.6 \text{ eV} \frac{m_e^*}{m_0 \epsilon} \tag{1.3}$$

and is 50.15 meV where m_e^* and ϵ are the electron effective mass (0.28 m_0) and dielectric constant (8.75) in ZnO, respectively [5, 23]. Generally, the s-states tend to deviate from the EMA value because the approximation of a point-charge core is not strictly correct. Different donors have different core-electron structure which gives rise to a short-range potential in addition to the Coulombic part. This is often called the central-cell potential and it can be positive or negative. For group-III elements in ZnO the central-cell potential

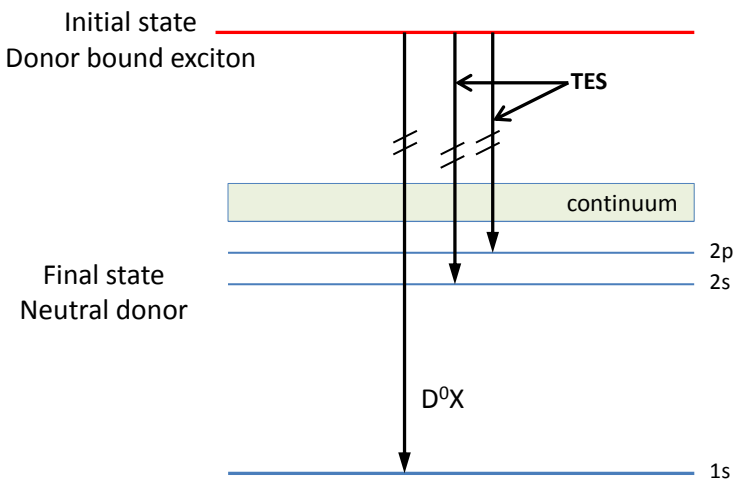

Figure 1.6: Schematic diagrams of TES transitions. $2s$ and $2p$ are excited states of the donor. It should be noted that the scales of the transition lines in the figure are not the same.

increases as we move down the periodic table. Despite several decades of study, there is no accepted theory of central cell interactions that explains all the trends in various semiconductors. The binding energies of the donor impurities in ZnO can be determined from $E_D = (E_{2p} - E_{1s}) + 12.61$ meV where 12.61 is the energy difference between the $2p$ energy level and the lowest conduction band energy [5]. The p-orbitals, having a node at the origin, have negligible central-cell shift.

In 1960, Haynes [37] found empirically that the energy required to free an exciton from a donor or acceptor impurity in silicon is a linear function of the donor or acceptor binding energy. Impurities with similar electronic structure often obey this rule, but some transitions due to structural defects in ZnO showed significant deviations [38]. These impurities might have significantly different central-cell structures. The physical origin of this behavior is not clear.

Despite the difficulty in achieving p-doped ZnO, there is considerable optical evidence for acceptors in ZnO with binding energies of 130 meV and higher. This is in a range where useful devices could be achieved if the doping concentration was sufficiently high. The EMA value for the acceptor binding energy in ZnO is 104.8 meV using m_h^*= 0.59 m_0 [23] in Eq. 1.3. However, there is still no credible report of A^0X transitions and this means that accurate measurements of acceptor binding energies in this material are not available since

the corresponding two-hole transitions cannot be detected. This is one of the unresolved issues in ZnO and is of high technological importance. In the very closely-related wide-gap material GaN, a relatively deep acceptor due to Mg has a binding energy of 164 meV and is sufficient to enable UV and blue LED technologies.

1.4.4 LO-phonon replicas

Phonons are quanta of the lattice vibrations and in ZnO there are 12 phonon bands, three of them acoustic and nine optical. Acoustic modes are due to the in-phase movement of the two atoms in the primitive cell while the optical modes are due to out-of-phase movements. In polar semiconductors, the opposite displacement of oppositely charged ions induce a long range electric field. The Coulomb interaction between the electron and the electric field produced by an LO-phonon is called the electron-LO-phonon interaction. There is a similar interaction for excitons that leads to the appearance of phonon-assisted emissions of free and bound excitons in the PL spectrum (Stokes line).

$$E_{m,n} = E_{ZPL} - mE_{LO} - nE_{TO} \tag{1.4}$$

where m and n are the number of created phonons, E_{ZPL} is the transition energy of the zero phonon line (ZPL), E_{LO} and E_{TO} are the energy of the longitudinal (LO) and transverse (TO) optical phonons, respectively. Coupling to TO-phonon replicas is so weak that they generally do not appear in the PL spectra of ZnO. The reported energy value of Brillouin zone center LO-phonons in ZnO is 71-73 meV [39, 40].

Optical transitions such as free and bound excitons are often accompanied by LO-phonon replicas, with an energy separation of 72.2 meV (1LO), 144.4 meV (2LO), etc. at the lower energy side. Thus, the first-order LO-phonon replicas of the donor-bound excitons in ZnO fall between 3290 and 3295 meV. However, the linewidths of the D^0X-LO transitions are $\sim$5 meV which makes the resolution of the peaks corresponding to each individual bound exciton challenging. In chapter 3, the phonon replicas of several D^0X transitions in ZnO are unambiguously identified using a series of systematically doped samples.

1.4.5 Donor-acceptor-pair and free-to-bound transitions

Another type of radiative recombination can occur in a semiconductor if both neutral donors and acceptors are present at sufficiently high densities. Fig. 1.7 shows a schematic diagram

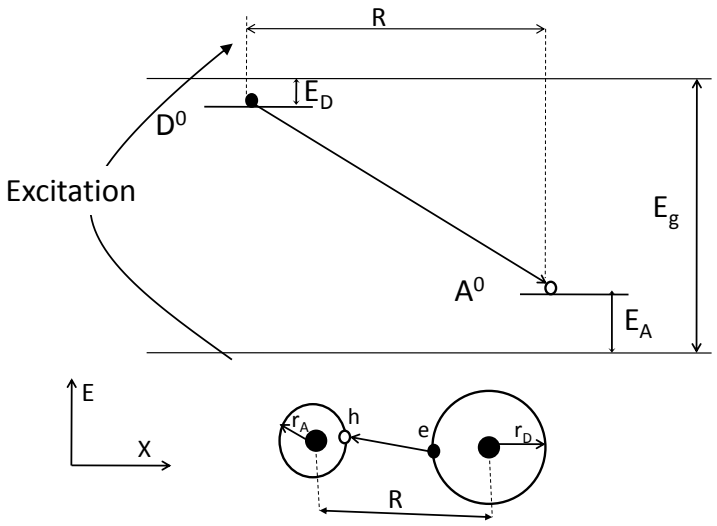

Figure 1.7: Schematic diagrams of DAP transition in the electron energy band structure as a function of the real space coordinate x. The donor and acceptor atoms are separated by the distance R.

of a donor-acceptor pair (DAP) transition. For sufficiently high densities of donors and acceptors the wavefunctions of the electron bound to the donor and the hole bound to the acceptor will overlap. The recombination energy of a DAP transition is given by

$$E_{DAP} = E_g - (E_A + E_D) + \frac{e^2}{4\pi\varepsilon R} \tag{1.5}$$

where E_g is the bandgap energy, E_A and E_D are the acceptor and donor binding energies, respectively and R is the pair separation. The last term on the right hand side of the equation is the Coulomb energy of the ionized impurities after recombination which lowers their energy. It can be seen from Eq. 1.5 that pairs with smaller values of R recombine with higher emission energies. These close pairs also recombine more quickly, so that the emission band becomes dominated by contributions from long-lived pairs in a pulsed excitation experiment (TRPL). In ZnO, transitions in the range 3310 - 3210 meV are often labeled as DAP, most of which coincide with the energy positions of phonon replicas in ZnO [19, 41, 42].

There are some reports about the observation of DAP bands in the energy range of 3.21–3.24 eV in ZnO [16, 31, 43]. The possible acceptor associated with these observations

was a nitrogen-related impurity of unspecified structural configuration.

Excitation-power and temperature-dependent PL measurements are useful tools to identify DAP transitions [16]. We will discuss them in detail in chapter 4 where we have observed DAP emission in the carbon-doped samples.

If a free electron present at the bottom of the conduction band recombines with a hole localized on an acceptor level, a photon with energy $h\nu = E_g - E_A$ can be emitted. This is called a free-to-bound transition (e,A^0). Fig. 1.8 shows a schematic diagram of the (e,A^0) transition.

These transitions dominate at intermediate temperatures or at room temperature when

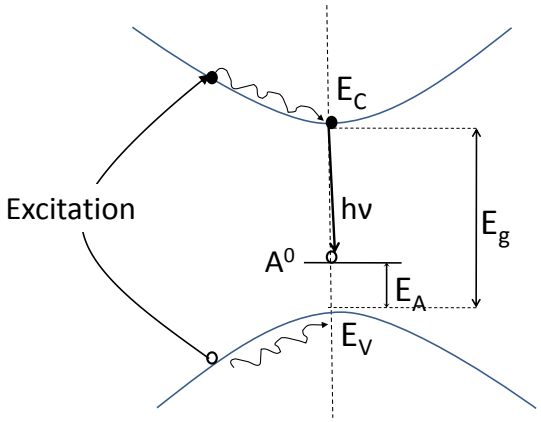

Figure 1.8: Schematic diagrams of (e,A^0) transition.

the lower-binding-energy donor electron is excited into the conduction band. This transition occurs at the high-energy side of the corresponding DAP peak at elevated temperatures.

e,A^0 is different from DAP since there is no Coulomb interaction and there is a free electron and a bound hole involved. Due to the involvement of at least one free particle (electron) in this transition it will have a Maxwell-Boltzmann lineshape and there will be an asymmetric line-broadening of the high-energy tail at higher temperatures.

An e,A^0 transition has been suggested to occur in ZnO PL spectrum around 3310 meV. This line has been the topic of controversy and has so far been attributed to various transitions including surface related bound excitons [44], and excitons bound to structural defects [4, 45]. We will discuss this transition in our carbon-doped samples in chapter 4 in more detail.

1.4.6 Temperature-dependence of PL transitions

The temperature-dependent behavior of bound-excitons in ZnO has been studied in this work and used in calculating their thermal activation energies. By increasing the temperature the bound-excitons are thermally dissociated and become free excitons. Using Boltzmann statistics and assuming a single bound-exciton level it can be shown that the intensity of a bound-excitonic recombination as a function of temperature is

$$I(T) = \frac{I(0)}{1 + g\exp(-E_g/k_BT)} \tag{1.6}$$

where $I(0)$ is the PL intensity at T = 0 K, E_a is the exciton thermal activation energy, k_B is the Boltzmann constant and g is the degeneracy ratio between the free exciton and the bound-exciton. Eq. 1.6 can be rewritten as follows for two bound-exciton levels [46]

$$I(T) = \frac{I(0)}{1 + g_1\exp(\frac{-E_{a1}}{k_BT}) + g_2\exp(\frac{-E_{a2}}{k_BT})} \tag{1.7}$$

where E_{a1} and E_{a2} are activation energies and g_1 and g_2 are degeneracy ratios. For $I(0)$ we use the PL intensity at the lowest temperature used in the measurements, which is typically 4.2 K.

Excited state transitions of the free or bound-excitons typically increase in intensity with temperature due to thermalization. One example of this situation is when the hole of the exciton is from the B-valence band instead of the A-valence band where the A-B band splitting is ~ 4.9 meV in ZnO. In this case the PL intensities for D^0X^A and D^0X^B will vary as

$$I(A) \propto \frac{1}{1 + \exp(-E_a/k_BT)} \tag{1.8}$$

$$I(B) \propto \frac{\exp(-\Delta E/k_BT)}{1 + \exp(-E_a/k_BT)} \tag{1.9}$$

where A and B are two excited states with a common ground state. Hence

$$\ln\frac{I(B)}{I(A)} = \ln C - \frac{\Delta E}{k_BT} \tag{1.10}$$

where C is a constant.

If the value of ΔE found from the slope of the graph intensity ratio vs. $1/T$ matches

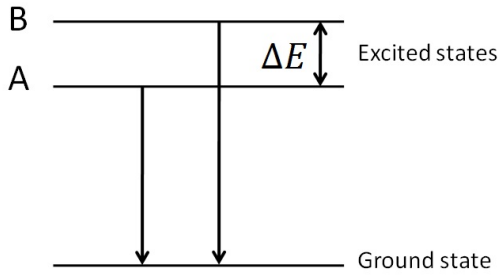

Figure 1.9: Schematic diagram of two excited states that terminate on a common ground state.

the spectral separation of the two close lines in the PL spectra, we can conclude that they both terminate on a common ground state of a defect.

Under an applied magnetic field when T is constant and the separation ΔE changes with increasing magnetic field strength, the graph of intensity ratios vs. ΔE gives the slope to be $-1/k_B T$. We will discuss this in more detail in chapter 5 when we determine the impurity type of the Sb-related D^0X center in Sb-doped ZnO NWs.

1.5 Influence of an external magnetic field

One of the powerful ways of investigating the physical nature of transitions in PL spectra is to apply magnetic fields to the sample along specific crystal directions. This enables the determination of charge state, electron and hole g-values, and impurity type (donor or acceptor) of bound-excitons.

In this section, we will provide a general overview of the effects of external magnetic fields on the ground and excited states of bound-excitons (D^0X and D^+X). Excitonic states can be considered as the initial (excited) states and the final (ground) state consists of the impurity electron or hole left after recombination (donor or acceptor) in the case of BX transitions. The splitting of the energy levels happens as a result of the interaction of the spin of the unpaired particle (hole/electron) with the external magnetic field. The Zeeman splitting energy is

$$\Delta E = \pm \frac{1}{2} \left| g_e \pm g_h \right| \mu_B B \ , \tag{1.11}$$

where μ_B is the Bohr magneton and g_e and g_h are the effective electron and hole g factors. It should be noted that depending on the type of BX, g_e and g_h can be related to the final

or initial states (see section 1.5.1.1). The excitonic g-value will be

$$g_{exc} = |g_e \pm g_h| \tag{1.12}$$

which is not isotropic. This means that its value can vary greatly depending on the crystal orientation with respect to the applied magnetic feild. In wurtzite ZnO, free electrons occupy an s-like conduction band and have an almost isotropic g value of 1.957 [47, 48]. For g_h, the absolute value of the anisotropic hole g factor is given by

$$g_h = \sqrt{\left|g_h^{\parallel}\right|^2 \cos^2\theta + |g_h^{\perp}|^2 \sin^2\theta} \tag{1.13}$$

where θ is the angle between the magnetic field B and the c-axis. It is clear from Eq. 1.13 that when B is perpindicular to c-axis ($B \perp C$) we have $g_h^{\perp}$ and when B is parallel to c-axis ($B \parallel C$) we have $g_h^{\parallel}$.

1.5.1 Zeeman splitting of excitonic states

According to Thomas and Hopfield's [49] study of the excitonic emission of CdS under a magnetic field, the Zeeman splitting behaviour of a BX strongly depends on the type of defect center that the excitons binds to, i.e., whether it is a neutral or an ionized donor/acceptor. In a neutral impurity center, D^0X, where there is only one unpaired electronic particle in the excited state, a simple linear Zeeman effect results. By contrast, in the ionized centers, D^+X, a more complex Zeeman pattern is observed.

1.5.1.1 Zeeman splitting of neutral impurity bound-excitons

In a donor/acceptor bound-exiton, the final ground state has a positive/negative core and an unpaired electron/hole which will split into two distinct energy levels in an applied magnetic field. The initial state of a D^0X contains two paired electrons and a hole and the splitting is determined by the anisotropic hole g-factor since it is the unpaired particle. In the case of an A^0X transition, the electron will be the unpaired particle and an isotropic electron g-factor determines the Zeeman splitting.

Figure 1.10 graphically illustrates the effect of magnetic field on neutral bound-excitons for the cases $\mathbf{B}\|\mathbf{C}$ (Faraday configuration) and $\mathbf{B}\perp\mathbf{C}$ (Voigt configuration). For D^0X, the magnitude of the hole g-factor depends on the direction of the magnetic field as given

by Eq. 1.13. In the Faraday configuration, the parallel-hole g-factor $g_h^{\parallel}$ is smaller than g_e. In the Voigt geometry the perpendicular-hole g-factor $g_h^{\perp}$ is small. In the acceptor-bound exciton case, apart from the differences mentioned earlier, the magnetic splittings and optical transitions are equal to those of D^0X. The energies of the Zeeman splittings of D^0X, for arbitrary angles θ between the magnetic-field $\mathbf{B}$ and the direction of the c-axis, can be determined by the equation

$$E = E_0 \pm \frac{1}{2}\mu_B B \left| g_e \pm |g_h| \right| \tag{1.14}$$

where E_0 is the spectral energy position of the bound-exciton without magnetic field and g_h is given in Eq. 1.13. Fitting Zeeman splittings in different directions of the magnetic field relative to the crystal c-axis with this equation provides the electron and hole g-factors.

It has been shown that the thermalization behavior of the emission components in the Voigt configuration can be used to determine whether a bound-exciton is a D^0X or A^0X [49]. Increasing the temperature will only affect the initial states of the PL transitions and under an applied magnetic field, any change in the ratio of the intensity of the split features will be from the initial states. As shown in Fig. 1.10, in the case of D^0X, when the magnetic field is perpendicular to the c-axis, the splitting in the initial state will be small due to a g-factor close to zero. Therefore, the ratio of the intensities of the split features will remain constant at different temperatures.

In the A^0X case, the electron g-factor is responsible for the splitting in the initial state and a change in the ratio of the intensities of the two split components will be observed. Thus, thermalization can be used to determine whether a line is D^0X or A^0X where a g-value close to zero applies in one case.

1.5.1.2 Zeeman splitting of ionized impurity bound-excitons

There is no unpaired spin in the final state of the D^+X ionized bound-excitons, thus they show no splitting in an applied magnetic field and in their initial state the electron and hole spin of the exciton are unpaired. Thus, the Zeeman splitting of a D^+X is determined by the splitting of the D^+X initial state and has a magnetic field dependence similar to the free exciton [5].

The Zeeman splitting for $\mathbf{B}\|\mathbf{C}$ and $\mathbf{B}\perp\mathbf{C}$ is displayed in Fig. 1.11 for the case of D^+X transitions. The most notable difference compared to D^0X transitions is that under a mag-

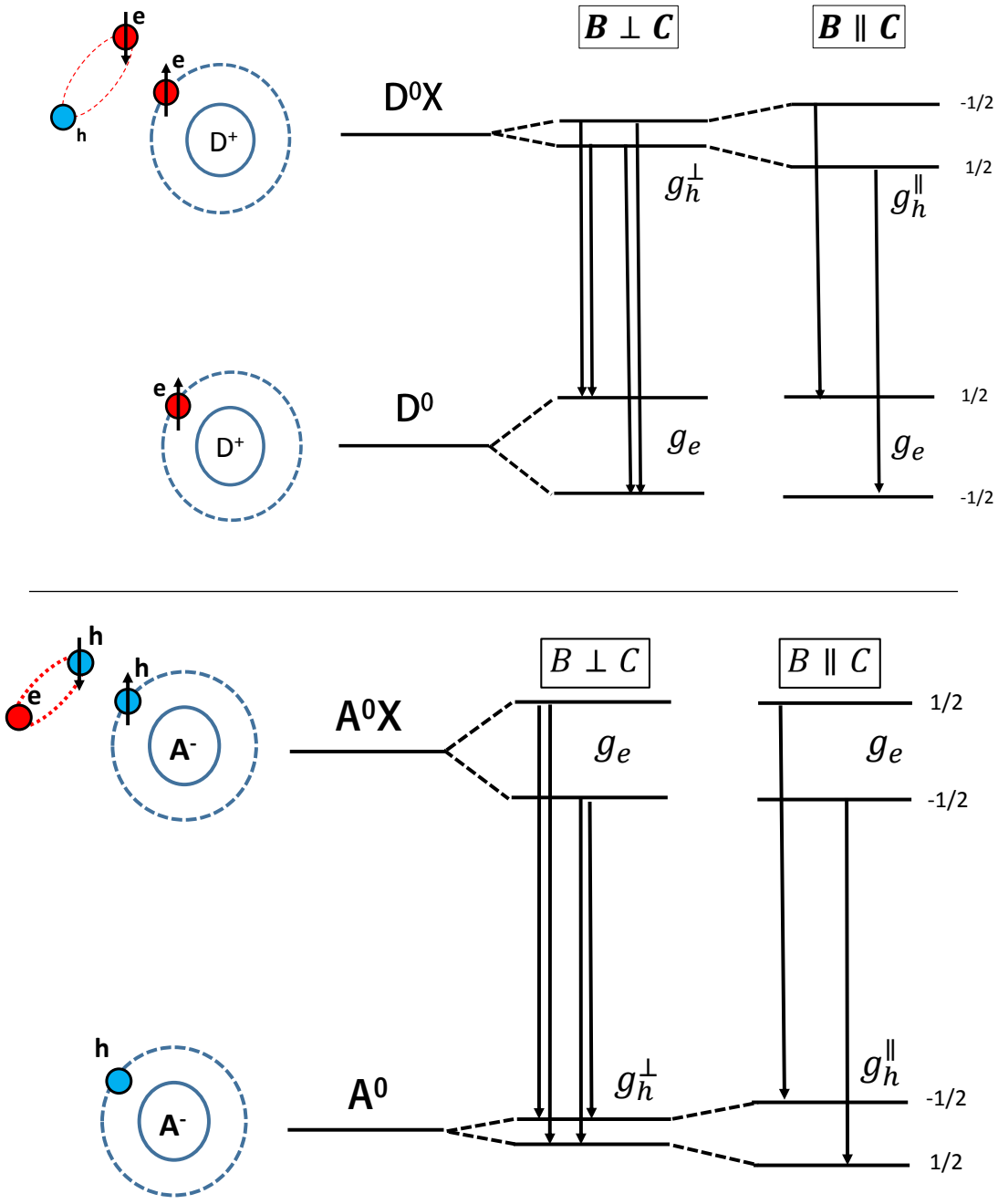

Figure 1.10: Zeeman splitting of neutral bound-excitons in an external magnetic field. The g-values in the initial and final states depend on the spin of the unpaired particles.

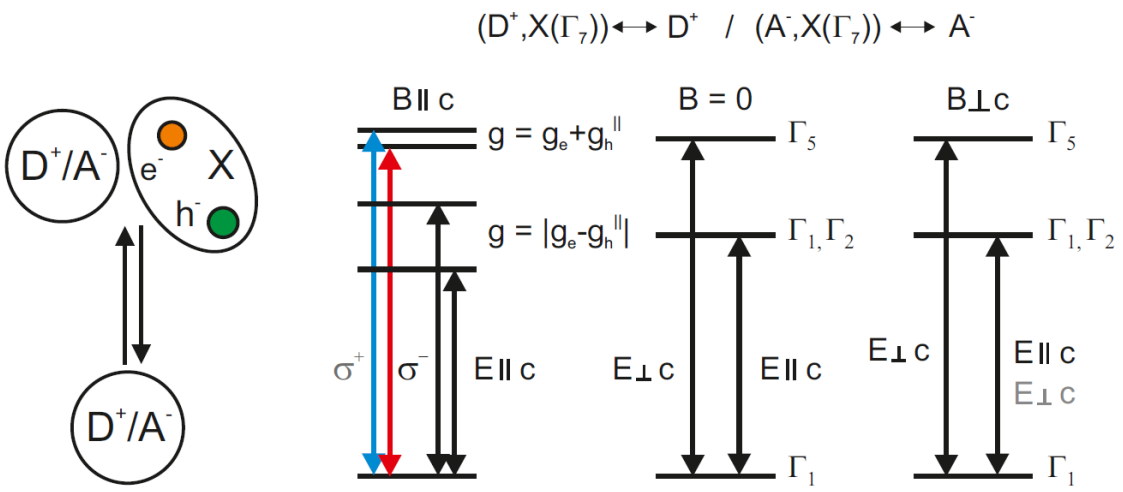

Figure 1.11: Zeeman splitting of ionized bound-excitons in zero field and under an external magnetic field. Taken from Ref. [5].

netic field perpendicular to the c-axis (Voigt configuration) a new lower energy line appears and its intensity increases at higher magnetic fields. This behavior clearly differentiates the D^+X from the D^0X transitions [49, 50].

1.6 Summary and thesis layout

This thesis provides a detailed study of the PL properties of different donor impurities in ZnO nanowires. The knowledge of the optical transitions related to dopant impurities in ZnO has been clarified and expanded. This study is focused on the properties of excitonic and non-excitonic transitions corresponding to various elements in the periodic table which had the potential to make ZnO p-type or n-type. In the first chapter of my thesis, I have presented an overview of ZnO band structure and its optical properties. Several topics have been identified and will be addressed later in this thesis.

The experimental techniques applied in this work are described in chapter 2. They include the growth method of the samples, low temperature photoluminescence, magneto photoluminescence (MPL) and time resolved photoluminescence spectroscopy (TRPL).

The experimental details and results are presented in chapter 3 to 5. In these chapters we have discussed exclusively the effect of doping impurities from group-III, IV and V of the periodic table on the PL spectra of ZnO nanowires.

Finally, in chapter 6 concluding remarks and future outlooks are provided.

Chapter 2

Experimental Techniques

This chapter provides an overview of the experimental methods used for ZnO nanowire (NW) growth and characterization. High-resolution low-temperature photoluminescence (PL) measurements were performed along with magneto-PL and time-resolved PL to optically characterize ZnO samples grown by metalorganic vapor phase epitaxy (MOVPE). Scanning electron microscopy (SEM) was used for structural characterization.

2.1 Growth of ZnO NWs and bulk crystals

The majority of the samples studied in this work were ZnO NWs (undoped and intentionally doped) grown at Simon Fraser University (SFU) by MOVPE. The growth was done by postdoc fellow, Senthil Kumar, in the MOCVD lab. Several bulk single crystals of ZnO (undoped and Sn doped) were received from Oak Ridge National Laboratory (ORNL) grown by chemical vapor transport (CVT) and their corresponding results are presented in chapter 4.

2.1.1 Metalorganic vapor pressure epitaxy (SFU)

One way to grow epitaxial single crystal NWs on single crystal substrates is by the MOVPE technique. In this process the precursors (organometallic chemicals) decompose in the vapor phase and react on a heated substrate to form a solid crystalline thin film. The precursor molecules, which are usually in the liquid state and stored in stainless bubblers, need to be transported to the growth chamber (reactor). A pure carrier gas such as nitrogen in our case flows into the liquid precursor through a bubbler dip tube, collects the reactant molecules and transfers the saturated mixture toward the reactor. The amount of the

precursor transported to the reactor can be adjusted by controlling the flow rate of the bubbler carrier gas as well as the temperature and pressure of the bubbler. The mixture of nitrogen and precursor gas is then mixed with a large nitrogen carrier gas flow, which transports the precursor gases to the hot growth zone. Fig. 2.1 shows a schematic diagram of the horizontal reactor chamber used to grow ZnO NWs for this study.

The substrate is placed on a slab of silicon carbide called the susceptor, and is heated by

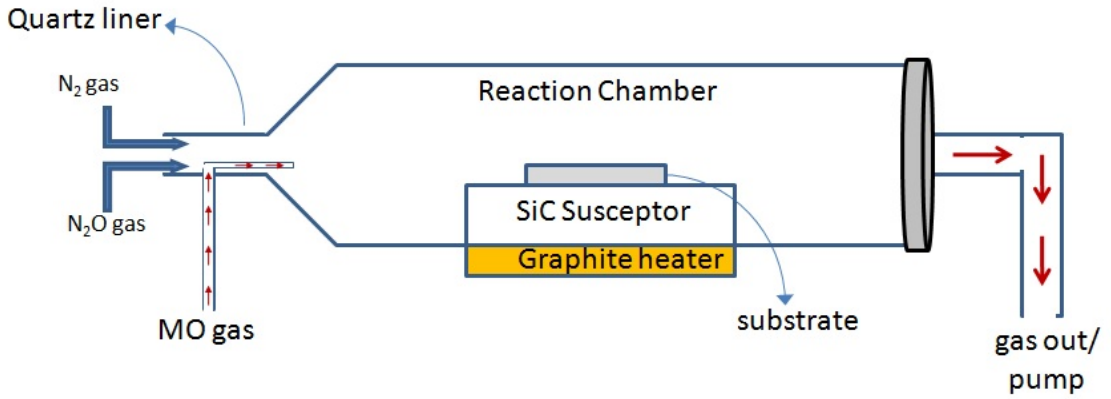

Figure 2.1: Schematic diagram of the MOVPE reactor chamber for the ZnO NW growth (SFU).

a resistance heater located below the suceptor. During the growth, a thin stagnant boundary layer of carrier gas resides directly adjacent to the heated substrate. The metalorganic chemicals diffuse through the boundary layer and approach the surface of the substrate and get heated and decomposed into organic radicals and source elements. After or during the decomposition, physisorption happens by weak Van der Waals forces between source radicals and the surface. These molecules can then migrate on the surface to form multiple chemical bonds and be incorporated into the crystal. The by-products of the reaction along with some of the precursor materials that did not decompose will reach the exhaust where they are oxidized by a large flow of air. In this work we have used dimethylzinc (DMZn) and nitrous oxide (N_2O) as precursors for Zn and O, respectively, and nitrogen was used as the carrier gas. ZnO NWs were spontaneously formed on sapphire c-plane substrates and the growth temperature and pressure were 605 ^oC and 700 Torr, respectively. For different doping experiments we have used different precursors as listed in Table 2.1. The details of the flow rates for each doping including the temperature and pressure of the bubblers and molar ratios are summarized in Appendix A.

Table 2.1: A summary of the organometallic precursors used in this study.

Abb.	Name	Chem. Form.
TEGa	Triethylgallium	$(C_2H_5)_3Ga$
TMIn	Trimethylindium	$(CH_3)_3In$
TMAA	Trimethylamine-alane	$AlH_3N(CH_3)_3$
	Carbon tetrachloride	CCl_4
TMSb	Trimethylantimony	$(CH_3)_3Sb$

2.1.2 Chemical vapor transport (ORNL)

In addition to the MOVPE ZnO NW samples grown at SFU, bulk Sn-doped crystals grown by chemical vapour transport (CVT) were provided by Dr. Lynn Boatner of Oak Ridge National Laboratory. The CVT growth was accomplished by the reduction of polycrystalline spheres of ZnO that are placed in a heated alumina tube. The process consists of two steps: the initial step involves the reduction of ZnO with hydrogen gas at the temperature of 1250^oC to provide a concentration of zinc in the region where the bulk crystal growth is to take place. The zinc vapor is transported to the cooler growth region by a nitrogen carrier gas. In the growth chamber, which consists of a larger tube of Al_2O_3, the crystals grow. Sn doping was achieved by mixing 0.15 mol% of SnO_2 with the starting ZnO polycrystalline material. The CVT process yielded needle shaped rods ranging in diameter from 0.2 mm to 2 mm and up to 15 mm in length.

2.2 Optical characterization techniques

PL spectroscopy is a nondestructive technique to characterize semiconductor materials. In a typical PL experiment laser light with an energy higher than the bandgap of the material excites electrons from the valence band to the conduction band creating electron-hole pairs which then thermalize rapidly to the band extrema, where they can form short lived bound states such as free excitons, and impurity bound excitons. These bound states can then recombine radiatively in the case of direct-gap materials. This recombination leads to optically detectable photons. In a PL experiment the number of photons emitted is measured as a function of energy.

Steady state, zero magnetic field PL measurements in this work were performed in our

lab at SFU while magneto PL and time-resolved PL measurements were performed at the Technische Universität of Berlin (TUB), Germany.

2.2.1 Photoluminescence

In this section, a general overview of the PL setup used in our lab is outlined. This PL system could collect signals ranging from ultraviolet (UV) to visible light. A schematic of the PL experimental set up is shown in Fig. 2.2.

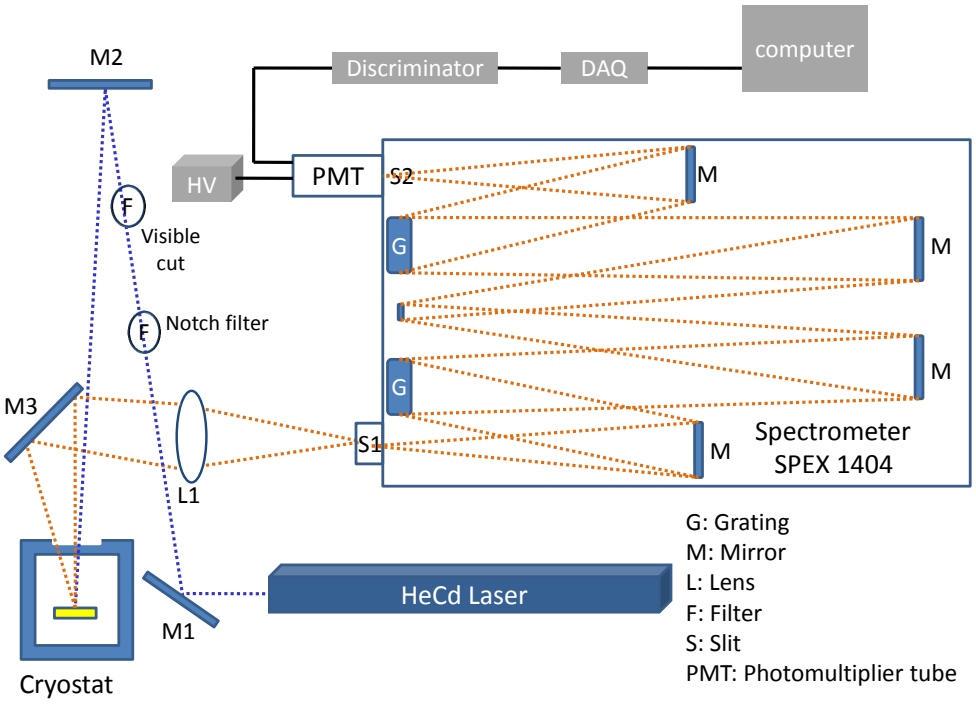

Figure 2.2: A block diagram of the optical setup for photoluminescence measurements carried out at SFU.

2.2.1.1 Excitation source and optics

PL was excited using the 325.031 nm line of a HeCd laser with a total power of 25 mW. M1 and M2 are reflecting UV laser mirrors with a diameter of 25.4 mm and were used to steer the laser light toward the sample. Two filters were used to cut off visible light and the other laser plasma lines so that highly narrow spectrum laser light was produced.

The luminescence coming from the sample was then collected by a 75 mm × 75 mm UV enhanced aluminum 1/4 wave mirror.

2.2.1.2 Cryostat

ZnO samples were mounted on a copper block in a dewar (Janis Corporation Varitemp) and were held in place by teflon tape. Liquid helium flow was maintained in contact with the bottom of the copper holder cooling the samples down to 4.2 K. The level of the liquid was maintained just below the sample laser spot so as to eliminate the bubbling that would be caused by direct immersion in liquid He. A temperature range from 4 to 325 K could be achieved during the PL measurement.

2.2.1.3 Spectograph and detector

The collected luminescence was then focused by a quartz lens with 50 mm diameter, and 150 mm focal length onto the entrance slit (S1) of the spectrometer. The spectrometer spectrally dispersed the light and a photomultiplier tube (PMT) detected the luminescence.

A SPEX 1404 double monochromator with a 0.85 m focal length was used for the PL measurements. The gratings used for this work (at SFU) had a ruling spacing of 1200 grooves/mm. The entrance and exit slits of the spectrometer were chosen according to the requirement of the specific measurements to control the resolution. The theoretical spectral resolution of a spectrometer is defined by the product of the linear dispersion of the grating and the slit width (in mm). The linear dispersion defines the extent that the spectrum spreads across the focal plane of the spectrometer and is equal to

$$\frac{d\lambda}{dx} = \frac{10^6 \cos(\beta)}{knL} \tag{2.1}$$

where β is the diffraction angle, k is diffraction order, L is the focal length, dx is the unit interval in mm and n is the groove density of the grating in lines per mm. The reported linear dispersion in the manual of the SPEX 1404, is 0.4 nm/mm at 514.5 nm wavelength. Thus for the 50 micron slit the slit-bandpass was 0.02 nm or 0.18 meV (Fig. 2.4).

Optical radiation detection in a PMT is based on the photoelectric effect. A PMT is an evacuated tube containing three main components: the photocathode, dynode chain and the anode (Fig. 2.3).

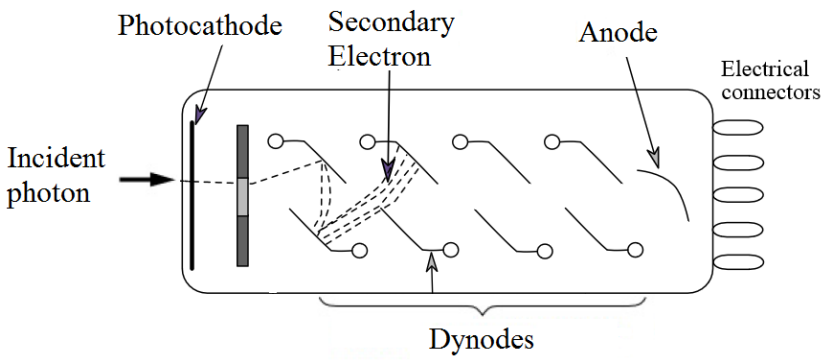

Figure 2.3: Schematic diagram of a photomultiplier tube [51].

When a photon hits the photocathode it can eject one electron by the photoelectric effect, generating one photoelectron. These primary electrons then accelerate towards a dynode chain and are multiplied through the emission of secondary electrons. A large number of secondary electrons are created for each incident electron. Generally, each primary electron generates 10^5 to 10^7 secondary electrons. These electrons are then collected by the anode as an output signal. In order to accelerate these electrons (primary and secondary) a high voltage is applied between the photocathode and anode. Finally, in single photon counting, the arrival of the electron pulse at the anode is detected as a single photon count and a current pulse is the output. A very important parameter for a PMT is its maximum anode current which is usually between 10 to 100 μA in order to avoid permanent damage to the PMT. Dark current due to thermoionic emission of electrons from the photocathode could be present even in the darkness and its typical value was between a few to hundreds of nA.

In this study a Hamamatsu R585 PMT was used, configured for photon counting, with a spectral response ranging from 160 nm to 650 nm and a maximum response wavelength of 420 nm. This tube has a 5 mm $\times$ 8 mm bialkali photocathode with a responsivity of 50 mA/W at 420 nm for photon counting. Because of the large photon energy in ZnO PL, detector cooling was not required.

The recorded wavelength was then corrected to the vacuum wavelength by accounting for the index of refraction of air (1.000289 at standard conditions) which was done by adding an average value of 0.106758 nm to all measured wavelengths. Wavelengths were then converted to eV using a conversion factor of 1239841.7 meV/nm.

Fig. 2.4(a) shows the spectrum of the Hg calibration lamp and the full width at half maximum (FWHM) for the most intense calibration line which was measured to be 0.08

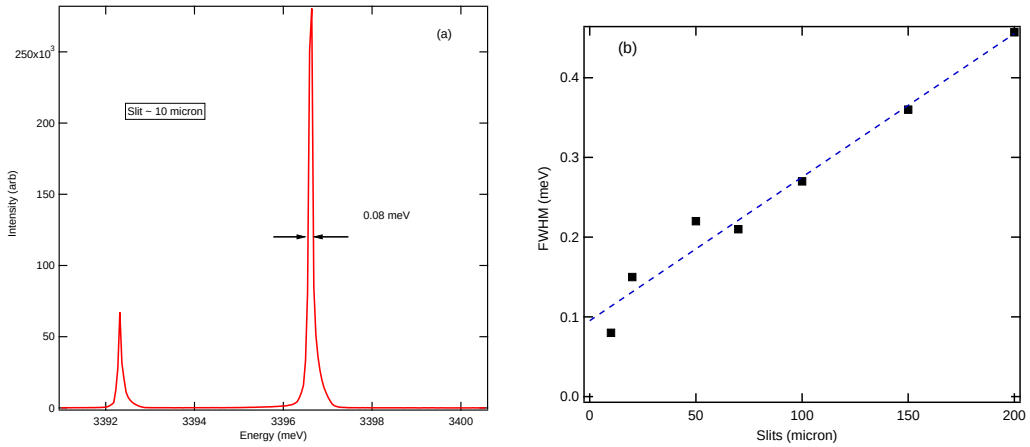

Figure 2.4: (a) Spectra of the Hg calibration lamp. The spectrometer resolution is 0.08 meV for the smallest slit width of 10 microns. (b) The measured FWHM at several spectrometer slit widths.

meV. Fig. 2.4(b) shows the measured FWHM for several spectrometer slit widths. One can reduce the slit opening to get higher resolution, at the cost of reducing the optical throughput.

2.2.1.4 Collecting electronics

Our system uses the photon counting method to acquire the optical signal. This technique is a good way of measuring low intensities since the number of output pulses from the PMT is proportional to the amount of incident light and it provides an excellent means of rejecting noise. Fig. 2.5 shows a block diagram of a photon counting apparatus. The output signal

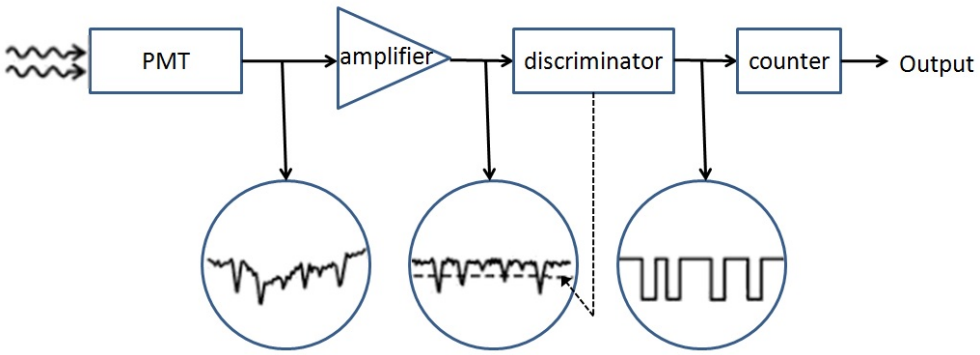

Figure 2.5: Block diagram of a photon counting system.

from the PMT is a series of pulses from emitted photoelectrons from the photocathode,

the thermionic emission in the cathode and dynodes and noise in the electronics. An input amplifier multiplies the signal then the amplified pulses enter a discriminator which eliminates pulses that are below a certain threshold. A voltage which is lower than this threshold would be considered as a noise current and therefore rejected. Finally the number of pulses is counted by a computer controlled counter.

2.2.2 Magneto-photoluminescence - Technische Universität of Berlin

A schematic set up of the MPL measurements is shown in Fig. 2.6. The PL set up used for MPL measurements at TUB is similar to the one in use at SFU but with some noteworthy differences. The sample was mounted in an Oxford magnetic field cryostat with a magnetic

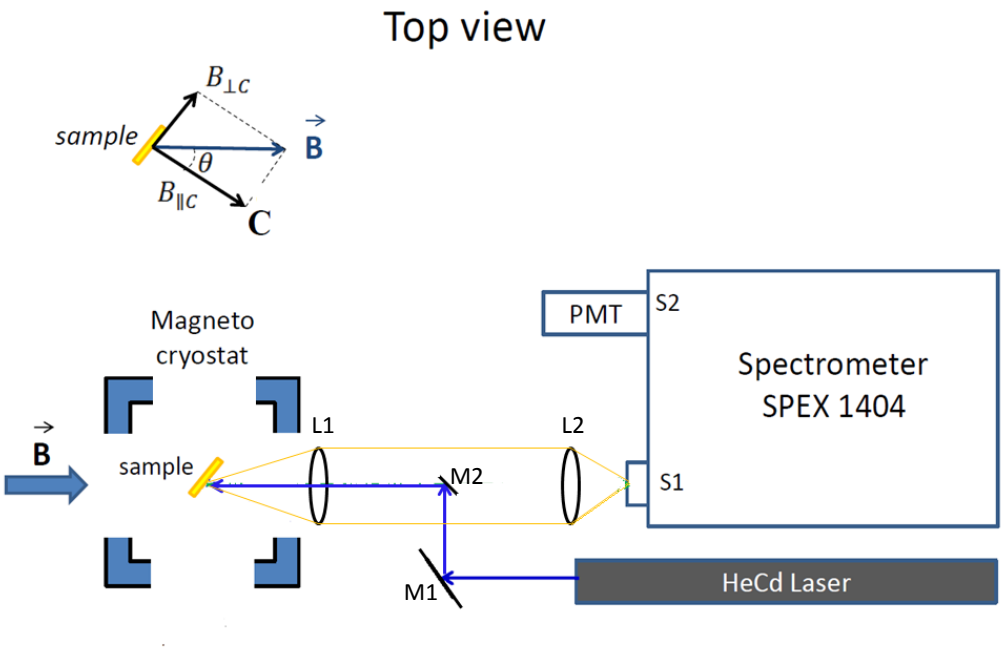

Figure 2.6: A schematic of the magneto-PL set up at Technische Universität Berlin (TUB). The inset shows the direction of magnetic field with respect to the crystal c-axis.

field strength up to 7 T at 2.2 K. The magnets consisted of a coaxial pair of solenoids separated by a gap to allow optical access perpendicular to the field.

The sample holder was rotatable which made it possible to do angular-resolved measurements by changing the sample c-axis with respect to the orientation of the magnetic field. The cryostat had two different pairs of windows on its four sides to allow straight through

optical access parallel or perpendicular to the magnetic field. To change from the Faraday (**k** parallel to magnetic field) configuration to the Voigt (**k** perpendicular to magnetic field) configuration, the whole cryostat had to be rotated. A HeCd laser with 5 mW power was used to excite the sample. Measurements were done in the backscattering geometry with a small 5 mm diameter mirror reflecting the laser on the sample. The PL was then collected with a 175 mm lens. Finally, a 200 mm lens focused the PL onto the entrance slit of the spectrometer. The spectrometer was similar to the SFU double spectrometer. For the detection, a Hamamatsu H10721-210 Mini-PMT was used.

2.2.3 Time-resolved photoluminescence - Technische Universität Berlin

Time-resolved PL measurements (TRPL) were also done at the Technische Universität Berlin. A schematic illustration of the set up is shown in the Fig. 2.7. The excitation source was a mode-locked Nd:YAG laser which produced 100 ps pulses with a frequency of 76 MHz at 1064 nm.

Since the bandgap of ZnO (3.4 eV) exceeds the energy of 1064 nm photons, a β-barium

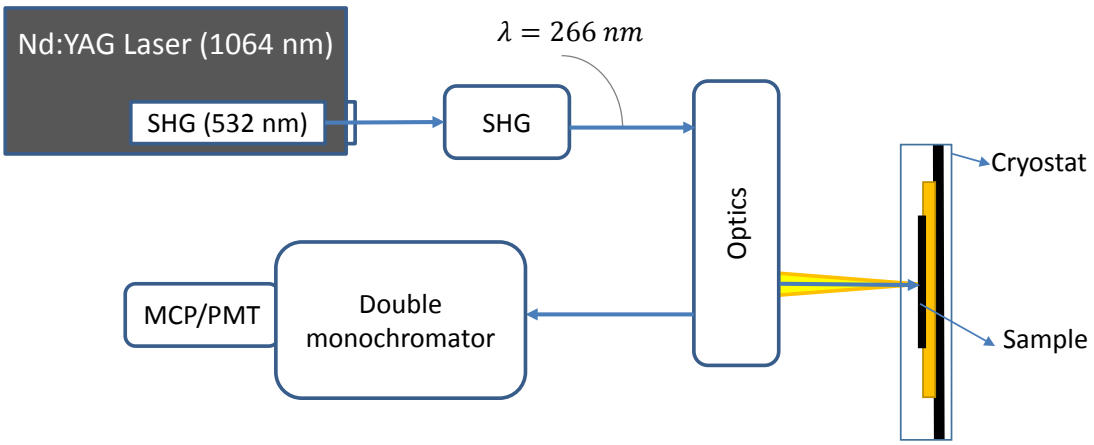

Figure 2.7: Illustration of the time-resolved PL measurements done at Technische Universität Berlin (TUB). Please see the text for details.

borate (BBO) crystal frequency doubles the laser beam, by second harmonic generation (SHG) where two photons having the same energy lead to a single photon with twice the original energy [52]. The Nd:YAG laser contains an internal SHG to obtain 532 nm. An

additional external cavity SHG crystal would then produce 266 nm laser pulses with 60 ps width.

The sample was located on a helium flow cryostat (Janis ST-500 microscope cryostat, 4–400 K) and the laser light was focused onto the sample surface using various optics. The TRPL signal is collected from the sample and is guided to a double spectrometer (McPherson, 2035, 0.35 m focal length) in combination with a multichannel plate (MCP) photomultiplier. A MCP is a plate consisting of small, parallel channels in a thin disk, with each channel acting as an independent electron multiplier. Since electrons only travel a short distance compared to that of a conventional dynode chain in a conventional PMT, the MCP PMT provides a much faster response.

Chapter 3

Study of Al, Ga, and In (Group III) Doped ZnO Nanowires

3.1 Introduction

It is necessary to produce high quality n-type ZnO in order to achieve high efficiency UV LEDs and laser diodes. Controlled doping of ZnO is the key for realizing electronic and optoelectronic devices. Several studies of implantation and backdoping of group-III elements (Al, Ga and In) in ZnO have demonstrated that they act as shallow donors and substitute on Zn sites [13, 35, 36].

There are few reports of the intentional doping of ZnO NWs using group-III impurities, particularly with the MOVPE growth method. The dopant concentration can be precisely controlled over a wide range using metalorganic sources in the MOVPE technique. The incorporation of donor impurities can be identified using low-temperature high resolution PL spectroscopy through their bound-exciton recombination lines. The nanowire geometry greatly reduces the effects of substrate lattice mismatch because of the very small contact between the substrate and the NW, and this results in very sharp transition lines. Despite the interest in this material for its potential optoelectronic applications, there have been very few reports of high-resolution PL measurements on intentionally-doped ZnO NWs. Park et al. presented the key early work on the growth of ZnO NWs by MOVPE, showing PL spectra with linewidths of 1–3 meV without any chemical identification [53].

A review paper by Meyer et al. [23]. confirmed the position of group-III related transitions in ZnO bulk crystal. There are several reports of doping ZnO NWs based on PL data

which were not high resolution nor low-temperature measurements [54, 55].

In this chapter we have studied the controlled addition of group-III donors into ZnO NWs grown by MOVPE by means of high resolution temperature and dopant concentration dependent PL measurements. PL spectra of D^0X transitions taken at 4.2 K revealed sharp linewidths (0.17 meV) and peak energies very close to those of bulk ZnO, confirming the absence of substrate induced strain and revealing the high crystalline quality of the ZnO NWs. We have clearly identified the D^+X transitions of different dopants by intensity correlation with corresponding D^0X transitions. The evolution of TES transitions of the Al, Ga and In donors with increasing dopant concentrations has been studied. This allowed us to precisely estimate the donor binding energies of group-III donors. We have also identified phonon replicas of group-III dopants unambiguously in our doped ZnO NWs. Transport measurements were done on some of the Ga-doped NWs by another student (Ali Darbandi). Part of this work was published in Semicond. Sci. Tech., 28, 045014 (2013).

3.2 Effect of group-III dopants on morphology

Group III dopants have a strong effect on NW morphology at higher doping concentrations, resulting in lateral growth especially at the tips of the NWs. High TMIn flow rates caused the morphology of NWs to change into planar films. Fig. 3.1 shows a comparison of SEM images taken for samples grown under identical growth conditions within each dopant series but with different dopant flows.

The details of the growth conditions for each sample are provided in Appendix A. The dopant flows are shown in nmol/min except for Al doping which is in sccm. The reason is that the vapour pressure of TMAA at room temperature (25°C) is 1.5 Torr, however, reliable vapor pressure data at a source temperature of -10 °C is unavailable. Thus we denote TMAA flow in volumetric units (sccm) [56]. The molar flow ratio is also shown in the Appendix A. The undoped nanowires have typical lengths of ∼2-3 μm with diameters of ∼200 nm. By increasing the doping concentration we observed an abrupt increase in the lateral growth which begins at the ends of the NWs while their diameters at the substrate interface are quite similar to those of the undoped wires. As can be seen from Fig. 3.1, for the In-doped samples, at the highest In dopant flows the morphology completely changes into a dense film with reduced total thickness (∼520 nm). A very similar result is observed for the Al and Ga doped NWs as shown in this figure.

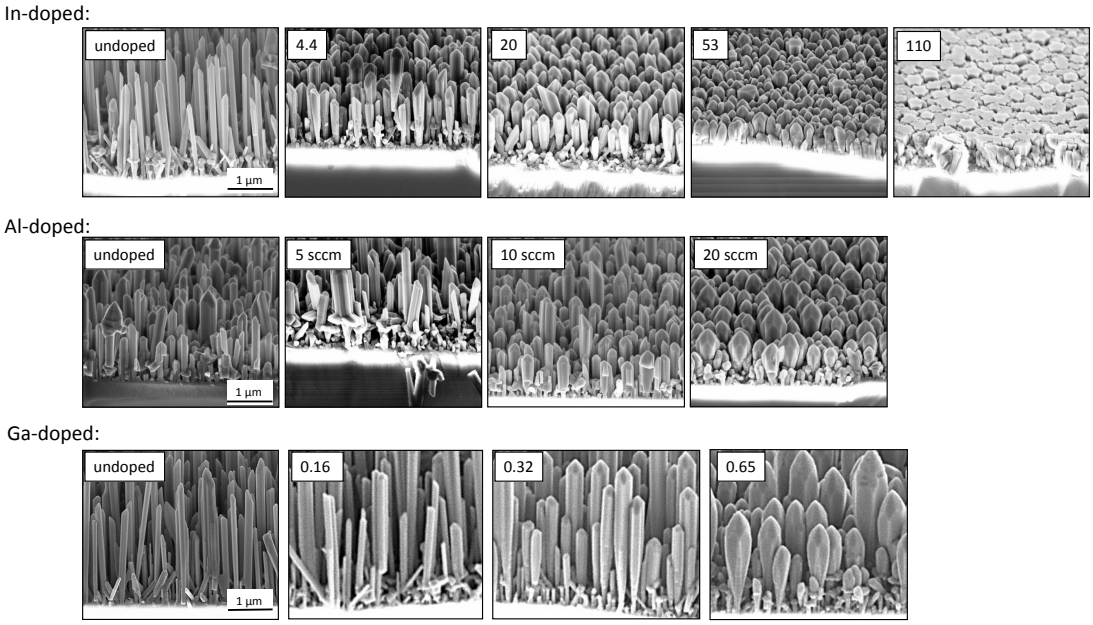

Figure 3.1: Effect of group-III dopant (TMIn, TMAA and TEGa) on the morphology of ZnO NWs. The units are in nmol/min except for Al doping. See Appendix A.

The c-plane (0001) facets have larger surface energy compared to the m-plane $(1\bar{1}00)$ sidewalls and this causes the formation of c-axis NWs in non-catalyzed ZnO grown by MOVPE [57].

As we add dopant impurities during the growth, they induce lateral growth which is the highest near the NW tip at higher doping concentration, while the basal diameters for low doping are similar to the undoped case. It is possible that the dopant adatoms increase the sticking coefficient for Zn adatom attachment on the m-plane sidewalls. The detailed mechanisms behind this unusual behavior are not yet clear. It is noteworthy that the group-III dopants show qualitatively similar behavior despite large differences in their atomic radii as well as the precursor chemistry.

3.3 Effect of group-III dopants on the photoluminescence spectra of ZnO NWs

Low-temperature PL lines associated with excitons bound to donor impurities (Al, Ga and In) were previously reported in bulk ZnO crystals [23]. In this work controlled doping of ZnO NWs by group-III elements over a wide doping range has been studied by high resolution low-

temperature PL spectroscopy. Doping of Al, Ga and In allowed us to unambiguously assign their corresponding two electron satellite and phonon replicas. The excitonic transition energies of these impurities are within 0.1 meV of previously reported values for bulk ZnO crystals, confirming the low level of residual strain in our samples. Since the growth of these samples occurred at different times, the undoped ones had a variety of residual impurities caused by contamination of the growth reactor and were observed in their PL spectra.

3.3.1 Excitonic transitions due to Al, Ga and In doped nanowires

Fig. 3.2 shows a comparison of PL spectra obtained at 4 K for undoped and lightly Al-doped NW samples (2 and 5 sccm). The PL from the undoped NW sample shows a very strong transition named I_8 and a very weak transition named I_9 due to excitons bound to residual Ga and In impurities, respectively. The extremely sharp I_8 linewidths of 0.17 meV is a sign of very low residual strain which indicates that lattice mismatch caused by the substrate is negligible, as expected for the NW geometry. The best homoepitaxial planar materials grown on ZnO substrates have a linewidth of around 0.08 meV [58].

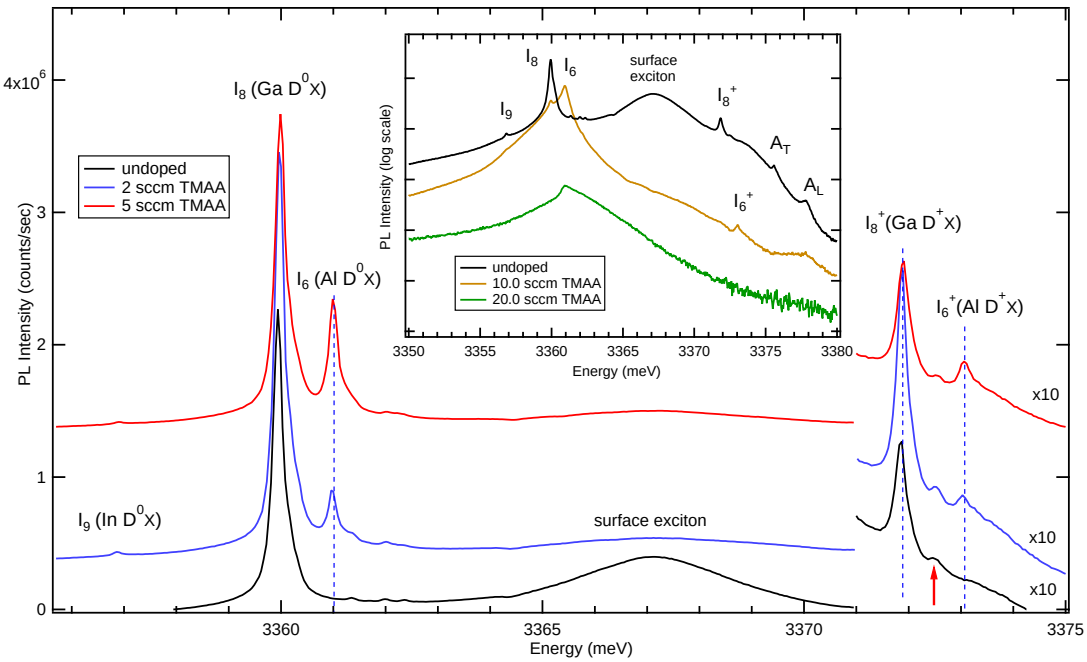

Figure 3.2: Comparison of PL spectra of undoped and lightly Al-doped ZnO NWs in the neutral and ionized donor bound-exciton region. The inset shows the PL spectra in a log scale. The arrow shows the position of the line previously attributed to Al D^+X.

The addition of a very small concentration of TMAA results in the appearance of a transition at 3360.9 meV. By increasing the TMAA doping concentration, the intensity of this peak increased relative to the I_8 transition. The previously reported energy position for excitons bound to Al donors in nominally undoped bulk ZnO single crystals is in agreement with our observation [23]. Thus, we unambiguously assign this line to excitons bound to neutral Al donors (I_6).

In the higher energy region of the PL spectra, another transition appeared after doping with TMAA at 3373.1 meV and increased in intensity relative to the Ga D^+X peak (I_8^+) with increasing TMAA flow. We have assigned it to the transition due to excitons bound to ionized Al donors (I_6^+). Meyer et al. [23] previously reported that D^+X of the Al occurs at 3372.5 meV. As can be seen from the Fig. 3.2, the transition at 3372.5 meV (shown by a red arrow) is also observed in the PL spectrum of the undoped sample and does not scale with Al doping concentration in the doped ones. Later in this chapter we show that the Meyer assignment is not correct and the transition at 3372.5 meV is the D^+X of the I_7 line which has an unknown origin. There are no studies to our knowledge about the high-resolution PL of systematically Al-doped ZnO reporting the position of D^+X of I_6. Therefore, we have revised the Al D^+X energy position to 3373.1 meV. Table 3.6, at the end of this chapter, shows the summary of the energies of D^+X and D^0X transitions reported here.

The inset of Fig. 3.2 shows the PL spectra for the heavily TMAA doped ZnO NWs on a logarithmic scale. The linewidth of the I_6 line is as sharp as I_8 and I_9 in the low-doped samples, while it increases from 0.17 to 2.5 meV for the higher doping concentrations. At the highest doping level only a broad line at 3360.9 meV is observed and the overall PL intensity is reduced. This could be due to the increased number of nonradiative recombination centers induced at higher doping concentrations. This reduction of PL intensity at high concentration is something that we observe with all dopants studied in this thesis. We attribute it later to the role of carbon-related impurity centers originating from the organometallic sources.

Fig. 3.3 shows a comparison of PL spectra at 4.2 K for undoped and very lightly Ga-doped NW samples. The PL from the undoped NWs is dominated by the transition at 3356.8 meV corresponding to a D^0X transition associated with In donors [23]. The presence of indium in the undoped NWs is due to a memory effect of the MOVPE reactor because of previous In-doped ZnO growth. The inset (a) in this figure is a blow up of the dashed rectangular region in the figure. In the undoped sample a weak transition at 3360.1 meV is

observed which agrees in position with the previously reported I_7 line, the chemical identity of which is unknown [23]. There is no observable Ga PL (I_8) in this sample.

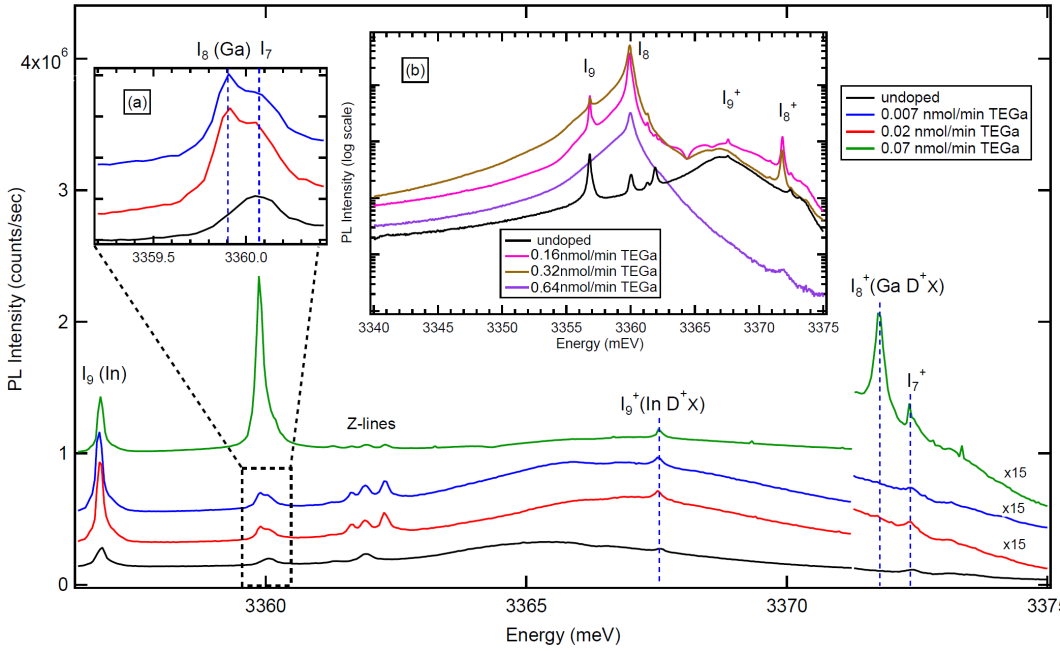

Figure 3.3: Comparison of PL spectra of undoped and lightly Ga-doped ZnO NWs in the neutral and ionized donor bound-exciton region. Insets show (a) blow up of the dashed rectangular region (b) the PL spectra of undoped and higher Ga-doped ZnO NWs in a log scale.

It is clearly seen from the inset (a) that a small addition of TEGa (0.007 nmol/min) results in a transition at 3359.9 meV, 0.2 meV below the I_7, which is absent in the undoped sample PL spectrum and associated with Ga dopant. This energy position is in agreement with the previously reported value for excitons bound to Ga donors, I_8, in bulk ZnO crystals [23].

A systematic correlation is observed between the I_8 transition intensity and the Ga doping concentration. At slightly higher Ga concentrations, the I_8 line intensity becomes comparable with the residual I_9 transition. In the higher energy region of the PL spectra another transition appeared with Ga doping at 3371.8 meV in agreement with the previously accepted position of the D^+X transition for Ga. [23] This line also scaled in intensity with increasing Ga doping concentration relative to the I_7 line intensity. Hence, we could unambiguously verify the position of I_8^+ in our Ga doping study and it is in agreement

with previous assignments which were based on the correlated occurrence of I_8^+ with its corresponding D^0X transition, I_8, in the bulk ZnO crystals [23]. It is noteworthy that the linewidth of I_8^+ does not change with increasing doping level in contrast to the I_8 transition. This indicates that the concentration of ionized Ga donors is low compared to neutral Ga donors. The I_8^+ transition is suppressed in the PL spectrum of the highest Ga-doped sample and the ratio of D^+X to D^0X intensity decreases.

Inset (b) shows a series of samples with a larger range of Ga dopant (0.16–0.64 nmol/min) with the PL intensity plotted on a log scale. The I_8 line shows significant broadening from 0.13 to 1.1 meV and has become the dominant line in the PL for the highest doped sample while an overall decrease in the integrated PL intensity was observed.

Very similar PL results are observed for In-doped ZnO NWs. Fig. 3.4 shows 4.2 K PL spectra of lightly In-doped NWs (1.0 and 4.4 nmol/min) in the bound-exciton region. The undoped NW sample shows dominant residual Ga D^0X transitions labeled I_8. Both undoped and lightly In-doped samples show a sharp peak at 3356.8 meV labeled I_9 which was previously identified as due to excitons bound to shallow In donors in ZnO bulk crystals [35].

Here also the observation of residual In impurities in the undoped sample is from the memory effects of the previous In doping experiments. A very clear correlation between In dopant concentration and I_9 transition intensity can be seen in Fig. 3.4.

In the D^+X region of the PL spectrum a strong increase in the sharp line at 3367.6 meV, labeled I_9^+, is observed corresponding to the excitons bound to ionized In donors in ZnO. By increasing the TMIn flow rate to 4.4 nmol/min, a significant broadening of the I_9 line with an overall increase in its integrated PL intensity is observed. As it can be seen from the inset figure, for dopant flows above 4.4 nmol/min the PL intensity has reduced strongly and suppression of all other PL peaks relative to the I_9 transition is observed. In the highest doping flows the PL intensity approaches zero. This could be the result of carbon contamination incorporating in the sample during the growth which may result in the incorporation of non-radiative centers. We will discuss C-doped ZnO NWs in Chapter 4.

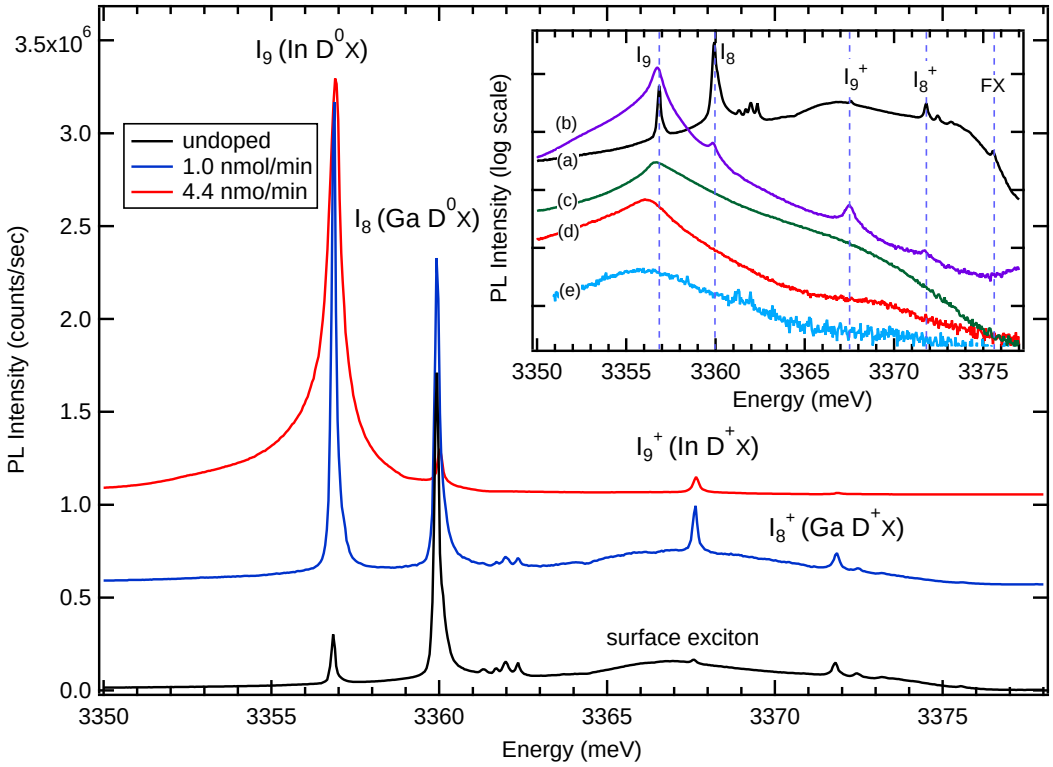

Figure 3.4: Comparison of PL spectra of undoped and lightly In-doped ZnO NWs. The inset shows the PL spectra of (a) undoped, (b) 21, (c) 53, (d)106 and (e) 213 nmol/min of In-doped ZnO NWs in a log scale.

3.3.2 Model of the asymmetric band tail in Ga-doped ZnO NWs

In this section we present a detailed analysis of PL lineshapes in order to estimate quantitative Ga donor concentrations. Table 3.1 gives a summary of the molar flows and gas phase [Ga]/[Zn] mole fractions for the samples presented in this section. As we have seen in the previous section, by increasing the group-III doping concentration the excitonic transitions exhibited an asymmetric broadening with a tail at the lower energy side.

Fig. 3.5 shows clearly that the lineshape changes asymmetrically with a tail at the lower energy side of the excitonic transition for higher doping flows. This was in coincidence with the change in the morphology of the wires shown in Fig. 3.1. The highest doped sample in this series is shown in blue and its overall PL intensity is decreased.

The inset figure shows the PL spectrum of the 0.07 nmol/min Ga-doped sample with a symmetric I_8 transition which is fitted with two Lorentzian functions representing I_8 and I_7 with FWHM of 0.17 and 0.3 meV, respectively. However, a Lorentzian function does not

Table 3.1: Molar flow ratio of Ga-doped ZnO NWs.

[Ga] (nmol/min)	Zn Bubbler T (^{o}C)	Zn Bubbler P (Torr)	[Zn] (nmol/min)	[Ga]/[Zn]
0.007	-20	800	2.24×10^4	3.1×10^{-7}
0.02	-20	800	2.24×10^4	9.9×10^{-7}
0.07	-20	800	2.24×10^4	3.1×10^{-6}
0.16	-20	800	2.24×10^4	7.1×10^{-6}
0.32	-20	800	2.24×10^4	1.4×10^{-5}
0.64	-20	800	2.24×10^4	2.8×10^{-5}

fit the observed asymmetric PL lineshape in the higher doped samples.

In the higher doped samples, we propose that there is a higher doping concentration in the shell of the wires compared to the core (Fig. 3.6). Hence, the superposition of the emission from the core (Lorentzian) and the shell of the NWs would be able to explain the excitonic lineshape. We had speculated before that by increasing the doping concentration during the growth the dopants accumulate at the shell of the wire resulting in increased lateral growth.

In this section we are trying to explain the asymmetric broadening of the excitonic transitions at higher doping concentrations for Ga-doped samples with a model based on exciton binding at donor pairs with variable separation in the shell region of the nanowires. The reason we chose Ga-doped samples is that their morphology does not change into films even at higher doping concentrations and this allowed us to check the model for a couple of doping concentrations. We start by assuming that for high enough doping concentrations, exciton wavefunctions can overlap more than one neutral donor impurity. We also assume that all donors are neutral at 4 K, i.e. the acceptor concentration is negligible in these samples. The change of binding energy of an exciton localized at two neutral donors can be estimated as [59]

$$\Delta E(R) \sim -2\epsilon_0 \exp(-\frac{R}{r_0}). \tag{3.1}$$

where R is the distance between the donors, ϵ_0 (15.6 meV) is the binding energy of an exciton bound to the isolated single donor and r_0 is the donor bound-exciton Bohr radius ($\sim$1 nm) [60]. Linear combinations of single D^0X states shared between two donors are assumed to form symmetric and antisymmetric superpositions which result in an increase or decrease in binding energy. The symmetric combination is expected to be favoured by thermalization and is given by Eq. 3.1.

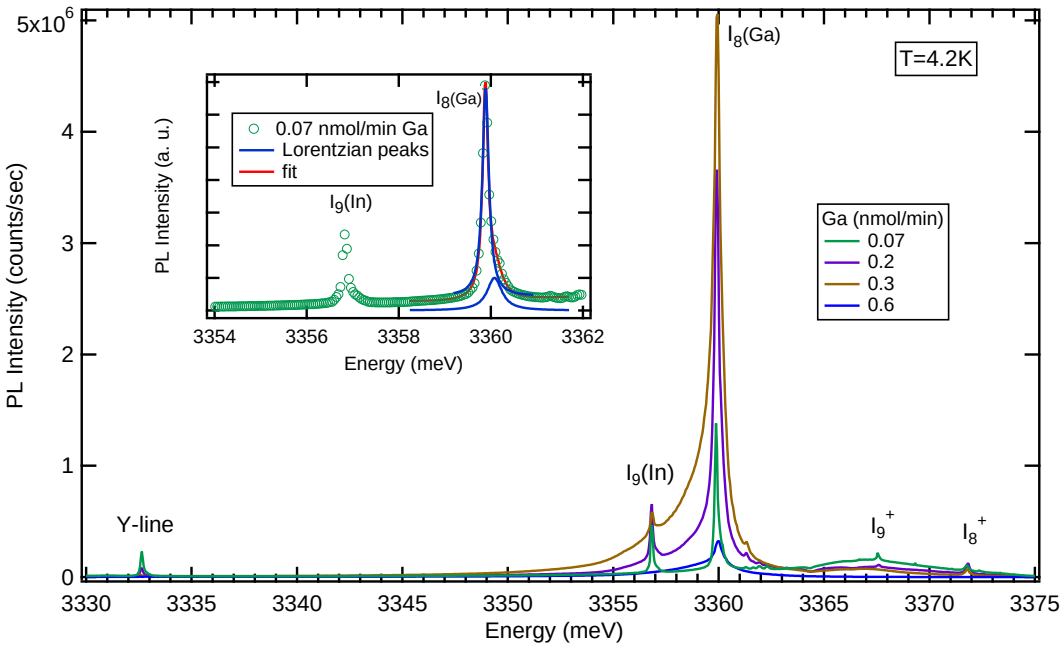

Figure 3.5: Comparison of PL spectra of Ga-doped ZnO NWs in linear scale. Inset shows the Lorentzian fit of the I_8 transition of the low Ga doped ZnO sample.

In higher doped regions, the excitonic transition energy changes from E_0 to $E_0+\Delta E(R)$. The probability of this transition also depends on the probability of finding another donor at a distance R from the original donor. If we consider that the distribution of intensity of emission for an exciton bound to a pair of donors with distance R is given by $I(E,R)$ then to obtain the total intensity distribution, $W(E)$, one must integrate over all such distributions weighted by the probability, $P(R)$, of a specific pair separation

$$W(E)dE = dE \int_0^\infty I(E,R)P(R)dR. \tag{3.2}$$

where $P(R)$ is the probability function calculated for a random distribution of impurities which is given by [61]

$$P(R) = \frac{3R^2}{R_0^3}\exp[-(\frac{R}{R_0})^3]. \tag{3.3}$$

and R_0 is the average distance between donors in the shell region of the NWs and is given by

$$R_0 = (4/3\pi N_d)^{-1/3}. \tag{3.4}$$

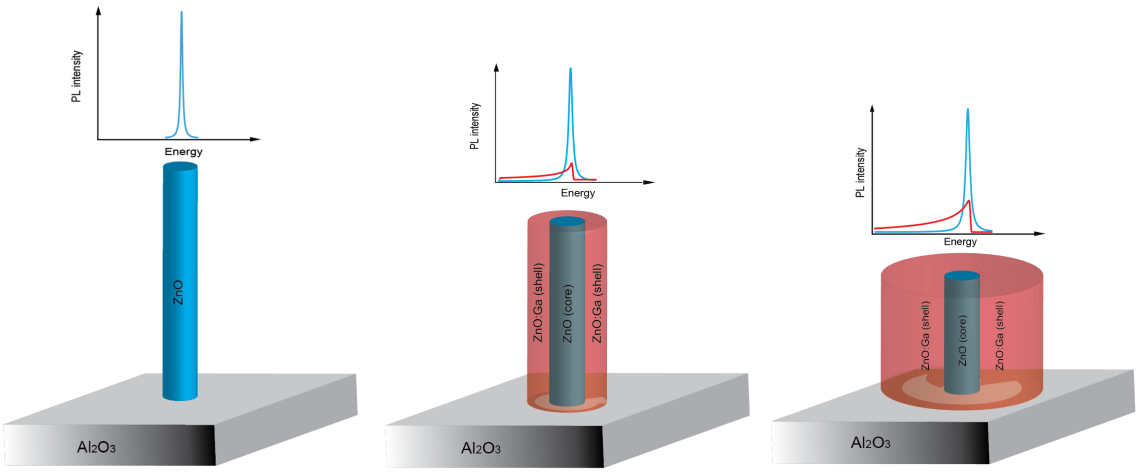

Figure 3.6: A cartoon explaining the contributions of the two different regions (core and shell) for doped samples to the PL spectra. From left to the right are diagrams of Ga-doped ZnO NWs with increased doping flow rate during the growth.

where N_d is the donor concentration.

Each component of the statistically broadened emission line will be treated as a sharp line, i.e. $I(E, R)$ in Eq. 3.2 will be replaced by a delta function.

$$W(E) = \int_0^\infty \delta(E - E(R))P(R)dR. \tag{3.5}$$

and

$$E(R) = E_0 + \Delta E(R) = E_0 - 2\epsilon_0 \exp(-\frac{R}{r_0}). \tag{3.6}$$

While this model is able to qualitatively reproduce the observed asymmetric lineshape at the tail of the excitonics transition, it was found that an additional Lorentzian component was required to fit all the PL line. The above integral gives the asymmetric lineshape in the excitonic PL emission due to the shell of the nanowires where the doping concentration is assumed to be higher. We solved this integral numerically considering R_0 as a fitting parameter. Then we fitted our experimental data with the superposition of this integral and the Lorentzian line profile contributing from the core of the NWs to find the doping concentrations in each sample.

Fig. 3.6 shows a schematic diagram illustrating assumptions of large lateral growth for three samples with different Ga flow rates, together with the corresponding schematic line shapes. Fig. 3.7 shows the PL data in the bound-exciton region for three samples with

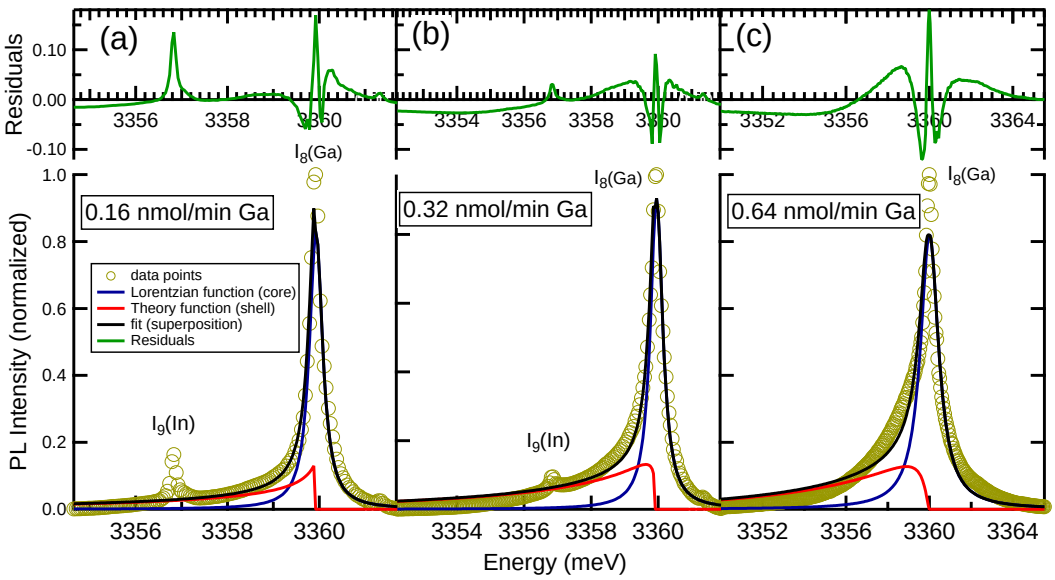

Figure 3.7: Comparison of PL spectra of undoped and higher Ga-doped ZnO NWs in linear scale.

different Ga flow rates fitted by the model at the position of I_8 transition. The average distance between donor pairs, R_0, estimated from the least squares fitting is in the range of 3.8 to 9.3 nm.

The Ga concentrations estimated from Eq. 4.2 are 2.9×10^{17}, 1.6×10^{18} and 4.3×10^{18} cm^{-3} for 0.16, 0.32 and 0.64 nmol/min flow rates, respectively. The residuals of the fits are shown in the top side of each plot. There is a better agreement for the lower doping concentrations while at higher doping the fit is not in a good agreement with the data. It is clear that the fit provides only an approximate description of the situation in these NWs. One possible source of the discrepancy is our lack of detailed accounting of the NW shape in the model. Assuming that the gas phase mole fraction of [Ga]/[Zn] holds for the solid also, we would expect Ga dopant incorporation of 7.5×10^{17}, 1.1×10^{18} and 2.3×10^{18} cm^{-3} for the 0.16, 0.32 and 0.64 nmol/min, respectively which are close to the estimated values from model.

3.3.3 Electrical characterization of Ga-doped ZnO NWs

Transport measurements on individual NWs were performed on different Ga-doped ZnO NWs with similar growth conditions. The only difference of these NWs are that the sapphire substrates were annealed under CCl_4 flow for 5 min prior to the growth. This resulted

in much narrower NWs with less lateral growth. Table 3.2 lists the dimensions of measured NWs in each sample along with their [Ga]/[Zn] flow ratios. The undoped NWs were about 10 micron long which made the electrical measurements feasible.

Table 3.2: Geometry of the NWs used in the electrical transport measurements

Ga flow (nmol/min)	Diameter(nm)	Length (μm)	[Ga]/[Zn] molar ratio
undoped	100	10	-
0.16	230	6	7.1×10^{-6}
0.32	300	2.85	1.4×10^{-5}

A nanoprobe with a sharp tungsten tip mounted inside a high vacuum chamber of a Strata DB235 field-emission scanning electron microscope (SEM) was used for these measurements by PhD candidate Ali Darbandi. The $I-V$ curves of the undoped and two Ga-doped ZnO NWs are shown in Fig. 3.8.

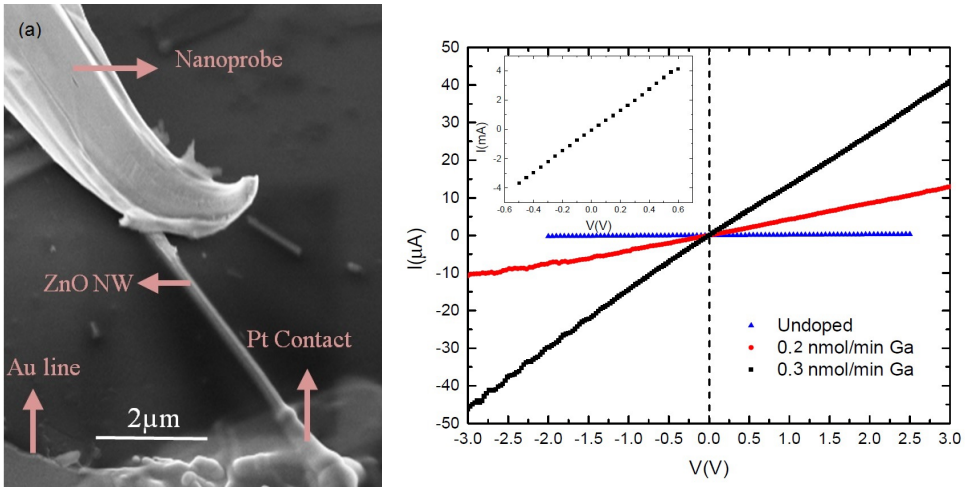

Figure 3.8: (a) SEM image of tungsten nanoprobe contacting the tip of a ZnO NW. (b) I-V characteristic of an undoped, 0.16 and 0.32 nmol/min Ga-doped ZnO NWs. The inset shows the $I-V$ characteristics with the probe directly on the grounded Pt contact and is an indicator of the parasitic contact resistances.

Electrical measurements were carried out at room temperature. The resistivities are calculated to be 0.78, 0.27 and 0.18 Ω-cm for undoped, 0.16 and 0.32 nmol/min Ga-doped ZnO NWs. Resistivity values have been calculated considering the NWs geometry like a cylinder.

Table 3.3: Values of fitted (R_0 and Lorentzian FWHM) and calculated parameters (N_d) in the model for three Ga-doped ZnO NW samples. Resistivity values are based on our electrical measurements. N_d values were also estimated from our measured resistivity values using Hall measurements from thin films in Ref. [1]. N_d values were also estimated based on the input gas phase [Ga]/[Zn] ratio assuming 100% incorporation of dopant.

Ga flow rate (nmol/min)	FWHM (meV)	R_0 (nm)	N_d (cm^{-3}) from model	Resistivity (Ω-cm)	N_d(cm^{-3}) Ref. [1]	N_d(cm^{-3}) (gas phase estimate)
undoped	no I_8	-	-	0.78	6×10^{16}	-
0.16	0.3	9.3	2.9×10^{17}	0.27	1×10^{17}	7.5×10^{17}
0.32	0.4	5.2	1.6×10^{18}	0.18	3×10^{17}	1.1×10^{18}
0.64	1	3.8	4.3×10^{18}	-	-	2.3×10^{18}

Then, the carrier concentrations for the 0.16 and 0.32 nmol/min samples were estimated from our resistivity data using previous reports of the resistivity vs. carrier concentration based on Hall measurements in bulk ZnO [1]. These carrier concentrations are also included in Table 3.3 which shows a summary of fitted (R_0) and calculated (N_d) parameters based on the model, as well as resistivity values obtained from transport measurement.

According to Table 3.3, the values of the doping concentrations estimated from our model are approximately one order of magnitude higher than the estimated carrier concentrations from our resistivity measurements [1]. Part of the discrepancy between the estimated doping concentrations from our model and the measured resistivity values in the NWs is because the electrical resistivities were calculated assuming the nanowires to be uniform cylinders, while the PL on which our model is based is likely dominated by a thin highly-doped shell layer. Finally, the gas phase [Ga]/[Zn] mole fractions were used to estimate the solid phase [Ga] concentration assuming 100% incorporation efficiency and the numbers are close to the values obtained from the our model.

3.3.4 Effect of doping on the Y-line transition

A narrow emission line is always observed in the PL spectrum of the undoped and lightly-doped ZnO samples at an energy position of 3332.6 meV. This line previously was observed in the PL spectrum of the bulk ZnO single crystals has been attributed to the recombination of excitons bound to extended structural defects is often labeled as the Y-line [23, 62]. This assignment was based on cathodoluminescence measurements which confirmed that the Y-line emission was localized at certain regions of the crystal. Fig. 3.9 shows the so called Y-line region of the PL spectra for group-III doped ZnO NWs.

Recently, magneto-PL measurements have shown that the Y line is due to emission of shallow donors that deeply bind excitons [38]. As it can be seen from Fig. 3.9, the intensity of this transition is very strong in the undoped and low-doped samples. There is also a correlation between the presence of the Y-line and the absence of lateral growth in these NWs. All samples with non-tapered NWs and without lateral growth had strong Y-line emission in their PL spectra. This includes the undoped, two lowest In and Al-doped and three lowest Ga-doped samples. In contrast, in the higher doped samples an abrupt decrease in the Y-line intensity to zero is observed. However, the reason for this is not clear yet. It might be due to the sudden removal of the structural defect to which it is attributed [38] at higher doping concentrations or it may be due to the fact that the shallow donor PL is dominating the Y-line PL.

3.3.5 Two-electron-satellites (TES) and Haynes rule in group-III doped ZnO NWs

When bound-excitons recombine, they generally leave the donor impurity in its ground state, which results in the principle $1s$ D^0X transition. However, the recombination of the excitons can also leave the donors in excited states (2s, 2p etc). Transitions corresponding to bound-exciton recombination with the final state of the donor in an excited state are called two electron satellites (TES) (see Chapter 1). However, the TES transition probability is lower, and hence the TES transitions are much weaker than the 1s transitions. Hence, it is often difficult to locate the TES energy positions of the donors when compared with 1s transitions. We found no reports on the correlation of TES energy positions with dopant species for doped ZnO. Available reports on the TES energy positions of the Al, Ga and In donors are mainly based on the residual impurities in the bulk ZnO single crystals [23, 30, 63].

In the energy range between 3323 meV and 3305 meV we have observed an increase in integrated PL intensity of the TES emission peaks with increasing Al, In and Ga doping. Fig. 3.10 shows the 1s (D^0X) transitions and corresponding TES (2s and 2p) doublet of Ga, Al and In donors of the undoped, 10 sccm Al and 20 sccm In-doped ZnO NWs. Undoped ZnO NWs show a dominant Ga 1s transition at 3359.9 meV. Ga- 2s and 2p transitions are observed at 3319.2 meV and 3317.9 meV, respectively. D^0X *1s* transitions of the Al and In donors are observed at 3360.9 meV and 3356.8 meV for the 10 sccm Al and 20 sccm In

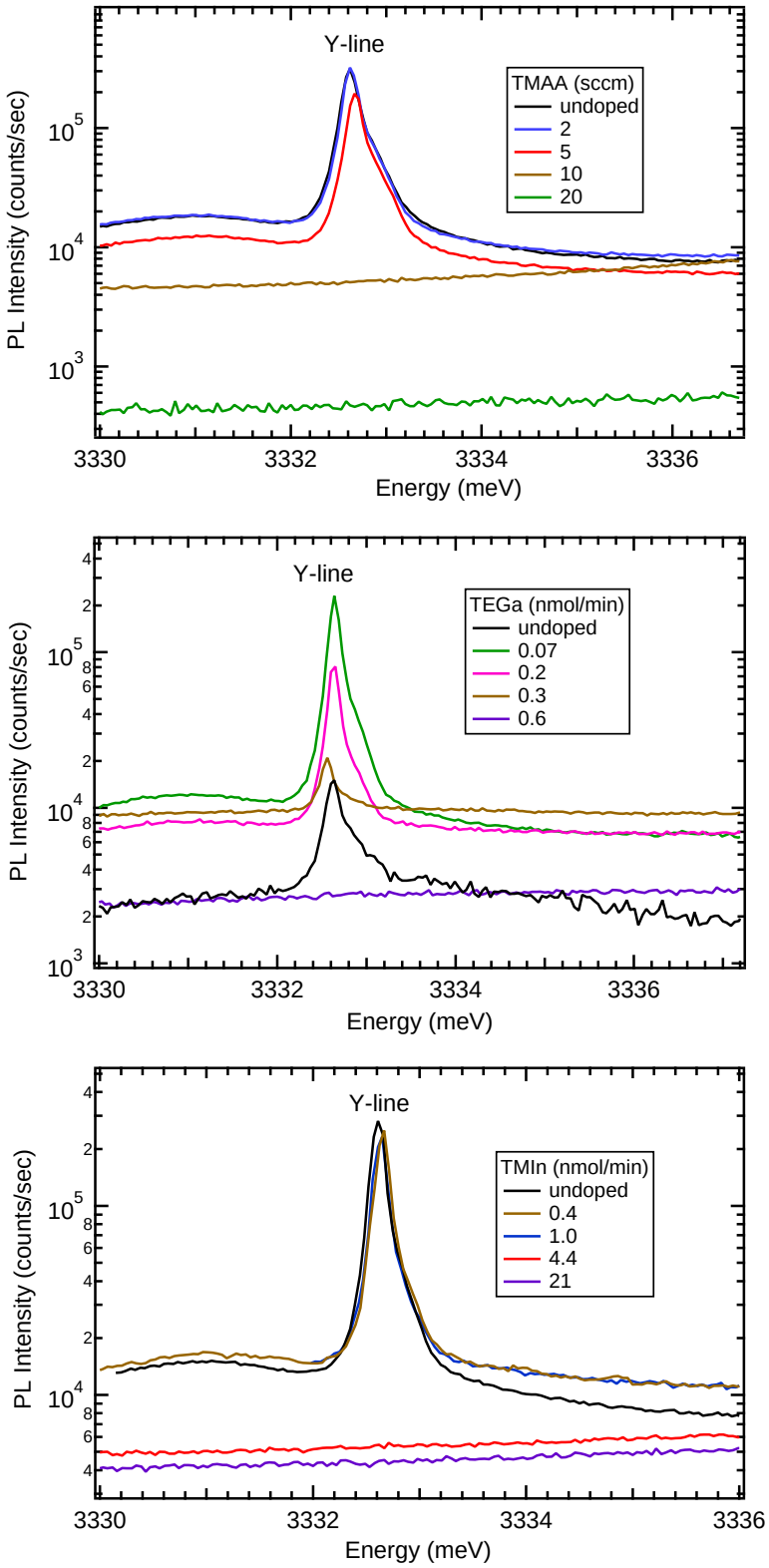

Figure 3.9: Effect of group-III doping on the Y-line luminescence.

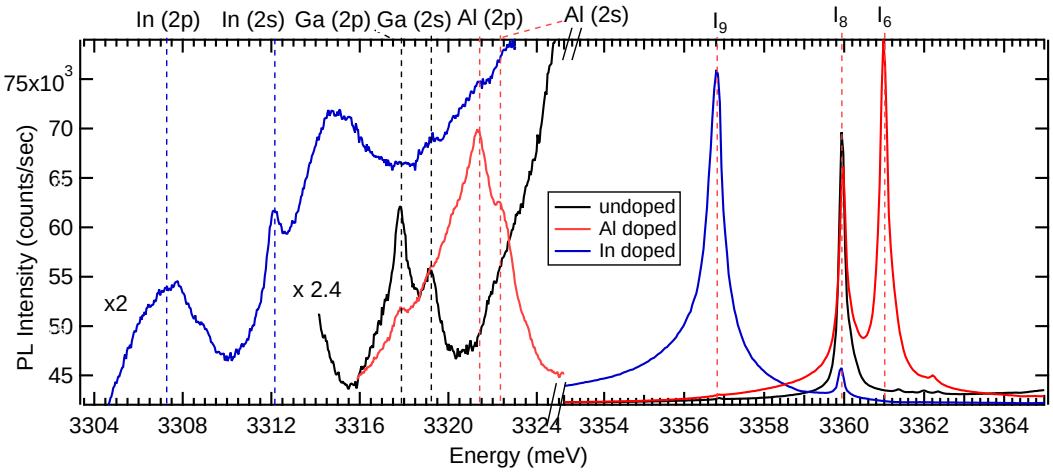

Figure 3.10: Principal 1s (D^0X) transition and corresponding 2s and 2p transitions of the Al, Ga and In donors.

doped NW samples, respectively. Al D^0X-2s and 2p transitions were observed at 3322.2 meV and 3321.3 meV, respectively. In D^0X-2s and 2p transitions were observed at 3312.1 meV and 3307.5 meV, respectively.

The binding energy of different donors can be estimated from the TES transition energy positions 1s and 2p as we discussed in Chapter 1. The accuracy of the donor binding energy estimate primarily depends on the TES energy position, since the D^0X, 1s, energy position can be measured very accurately because of its narrow linewidth. Thus, systematic group-III donor doping allowed us to unambiguously assign the TES energy positions of Al, Ga and In donors.

Table 3.4: Summary of the TES transitions of the group-III donors (Al, Ga and In) in ZnO NWs.

Donor	*1s* (meV)	*2s* (meV)	*2p* (meV)	$E_{2p} - E_{2s}$ (meV)	$E_{1s} - E_{2p}$ (meV)	E_D (meV)	E_L (meV)
I_6 (Al)	3360.9	3322.2	3321.3	1.1	39.6	52.2	14.6
I_8 (Ga)	3359.9	3319.2	3317.9	1.3	42.1	54.7	15.6
I_9 (In)	3356.8	3312.1	3307.5	4.6	49.3	61.9	18.7
Y_0-line	3332.6	3273.5	3270.1	3.4	62.5	75.11	42.9

Table 3.4 summarizes the TES energy positions and donor binding energies of the Al, Ga and In donors. Low-doped NWs samples show TES transitions of the Y_0-line at 3273.5 meV

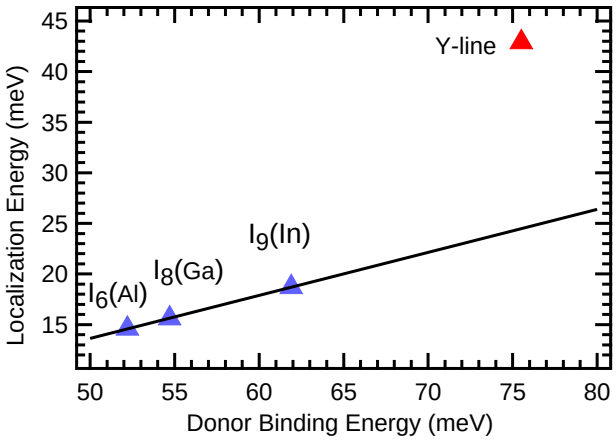

Figure 3.11: Plot of localization energy vs. donor binding energies of the Al, Ga and In donors as well as the Y-line. The data point related to Y-line does not fall on the straight line.

and 3270.1 meV for 2s and 2p transitions, respectively. These values are very close to the reported Y_0-TES energy positions for the ZnO bulk crystals [38]. The Y-line binding energy is estimated assuming a singly-charged donor final state with an effective mass excited state.

Fig. 3.11 shows D^0X localization energy vs. donor binding energy for the Al, Ga and In donors as well as the Y-line. The exciton localization energies increase linearly with donor binding energies for the group-III shallow bound-excitons. This empirical result is usually referred to as Haynes rule. The difference in the donor binding energies is due to the different core electronic structure of the group-III impurities. The reason for the linear correlation with exciton localization energy is not understood, but is well obeyed in many semiconductors. However, the Y-line does not follow this linear trend. This indicates that the core electronic structure of this defect is very different from that of the group-III donors.

Fig. 3.12 shows a plot of localization energy for the D^+X transitions studied in this chapter vs. the corresponding D^0X transitions. The D^+X transitions also obey Haynes rule for the group-III donors (shown in 4.6), hence it is not surprising that the D^+X vs. D^0X plot is linear for the group-III donors.

Previously reported values for excitonic transitions due to group-III donors for bulk samples are shown in this graph as circles for comparison. Our new assignment for the D^+X transition of Al falls into a strict linear relationship between D^+X and D^0X energy positions. There is a data point in this plot related to I_7 transition, the chemical identity

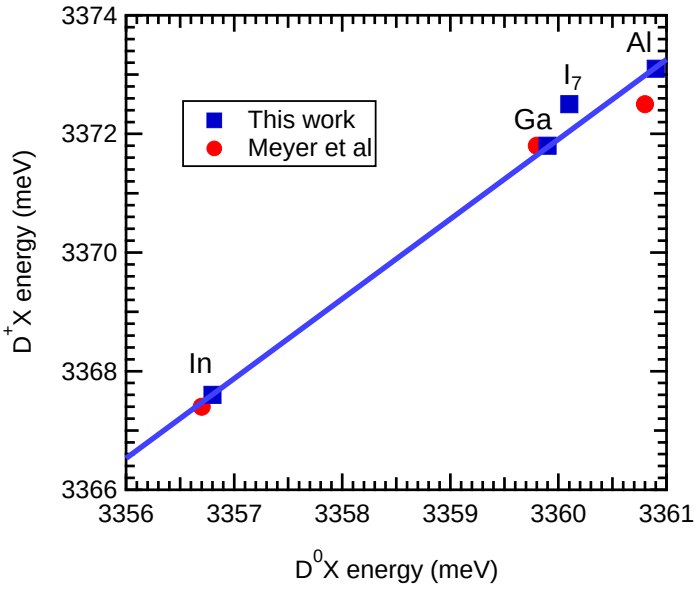

Figure 3.12: Plot of D^+X versus D^0X energy positions for In, Ga, and Al donor transitions along with I_7 line which has an unknown origin. Circles show previously reported data for bulk ZnO samples from [23].

of which is unknown [23]. At this point we have not observed any TES corresponding to the I_7 transition and we could not estimate its donor binding energy.

3.3.6 Phonon replicas of D^0X transitions

D^0X transitions in ZnO are often accompanied by phonon side bands (LO-phonon replicas), with an energy separation of 72.2 meV (1-LO), or 144.4 meV (2-LO), etc to lower energy. These transitions arise from emission of integer numbers of optical phonons (72.2 meV for ZnO) during exciton recombination [23, 38]. Generally, the linewidths of the D^0X-LO transitions are about 5 meV which is larger than the energy separation between the Al, Ga and In D^0X transitions. Thus, D^0X-LO transitions of the Al, Ga and In donors are often merged to a single peak, which makes it difficult to assign them to a specific donor. Chemical assignment of the phonon replicas of the D^0X transitions to a specific donor is not previously reported to the best of our knowledge.

In the same energy region other transitions are often observed and assigned to donor acceptor pair (DAP) transitions and these are regarded as the fingerprint for the presence of acceptor impurities in ZnO [16]. We have explained DAP transitions in Chapter 1.

D^0X LO phonon replicas can be misinterpreted as DAP transitions since both appear in the same region in the PL spectrum. Phonon replicas are very common in ZnO; the free exciton, and all of the common bound-excitons (D^0X, TES and Y-lines) can couple with optical phonons. However, DAP transitions can be observed only if there are acceptor impurities present in the sample.

In this section the energy positions of the LO phonon replicas of the D^0X transitions of specific donors are unambiguously identified. Fig. 3.13 shows the PL spectra of undoped, Al- and In-doped ZnO samples at the lower-energy phonon replica region.

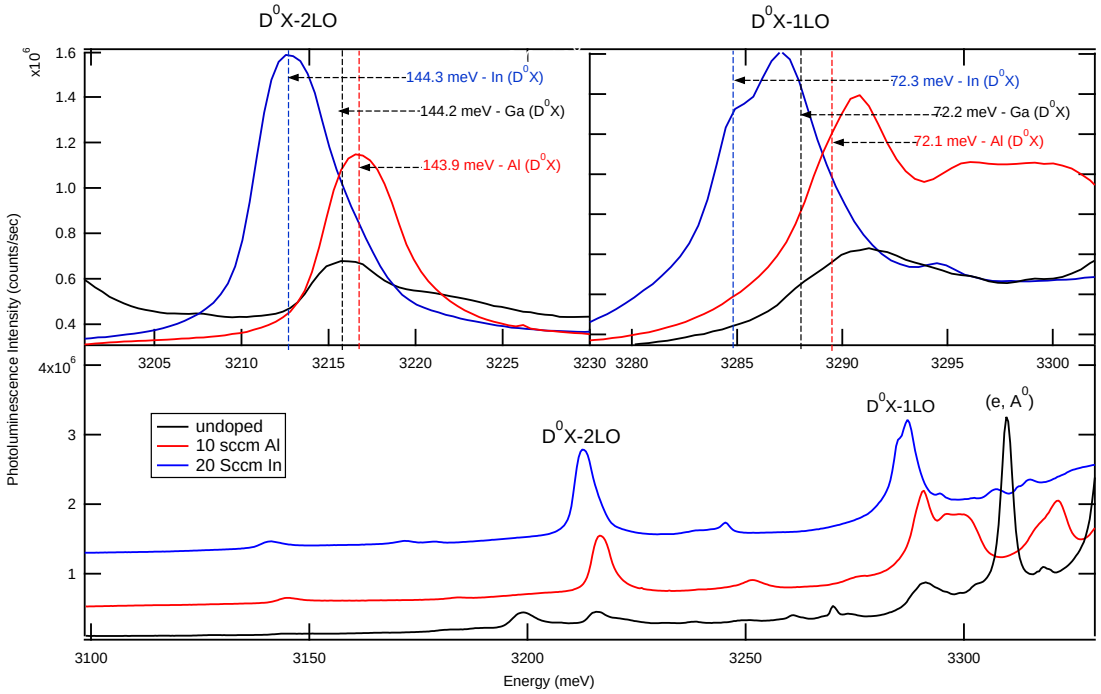

Figure 3.13: Comparison of the low energy region PL spectra of the undoped, 20 sccm In-doped and 10 sccm Al-doped ZnO NWs. Left and right insets are blowup at 2-LO and 1-LO phonon regions, respectively.

The energy spacing between LO phonon replicas and the principle zero-phonon line (D^0X) is 72.2 meV in ZnO. We could unambiguously identify the energy position of 2-LO phonon replicas in ZnO by systematic doping experiments. The inset on the left side of the Fig. 3.13 is a blow-up of the 2-LO transition. The dashed lines in the figure show the expected positions of the second phonon replica of the Al, Ga and In D^0X transitions. At 72.2 meV above this region we observe the 1-LO region which is shown in the right inset

Table 3.5: Summary of the zero phonon line (ZPL), 1LO and 2LO of the various donor bound-exciton transitions.

Transition	Energy		
	Zero phonon line (ZPL) (meV)	1st phonon replica (meV)	2nd phonon replica (meV)
I_6 (Al)	3360.9	3288.8	3216.8
I_8 (Ga)	3359.9	3287.7	3215.7
I_9 (In)	3356.8	3284.5	3212.8

figure. The 1-LO transitions are not very clear for Ga and Al related transitions due to appearance of other unknown lines in this region.

The undoped sample has a strong Ga D^0X transition in the excitonic region while in the Al and In-doped samples Al and In transitions are observed above and below the Ga line, respectively. The left inset in Fig. 3.13 shows that the transition in the undoped NWs around 3215.7 meV undergoes a blue shift with Al doping and a red shift with In doping, respectively, to have 144.4 meV energy difference with their corresponding D^0X transitions. The shift depends on which donor impurity has the highest concentration.

From the above arguments it is clear that the transitions at 3212.6 meV, 3215.7 meV and 3216.7 meV are associated with the 2LO replicas of In, Ga and Al-D^0X transitions, respectively. The energies of the phonon replicas of the group-III impurity transitions are summarized in Table 3.5.

3.4 Conclusion

The effect of group-III doping on the optical and morphological properties of ZnO NWs was investigated over a wide range of impurity doping concentrations. High-resolution PL spectra with linewidths as low as 0.17 meV for undoped NWs with peak energies very close to those of bulk ZnO crystal are obtained which is confirming a remarkable absence of substrate induced strain. Neutral and ionized donor bound-exciton transitions of various impurities were unambiguously identified. The addition of group-III dopants was correlated with the appearance of corresponding neutral and ionized donor bound-exciton transitions. This helped us to revise the energy position of Al related transition I_6^+ to 3373.1 meV in contrast with previous reports for bulk crystals.

Table 3.6 shows the energy position of group-III related transitions in the excitonic

region along with the I_7 transition which has unknown origin as yet. By increasing dopant concentrations, lateral growth becomes significant. The lateral growth at higher doping flow rates coincided with the suppression of the structural defect related transition so-called Y-line.

In addition, a large increase in D^0X linewidth is observed with doping concentration. At higher doping levels an asymmetric broadening is observed with a tail at the lower energy side. We have developed a model based on the pairing of donor impurities at the shell region of the highly-doped NWs to explain this in Ga-doped ZnO NWs. Based on our model we could estimate the donor concentration in ZnO NWs. Electric transport measurements confirms the increase in doping concentration.

In the lower energy region of the ZnO PL spectra, We have clearly observed the two electron satellite peaks of the Al, Ga and In donors and estimate the donor binding energies. Doping with group-III impurities has allowed us to unambiguously assign the corresponding phonon replicas of donor bound-exciton transitions.

Table 3.6: Summary of the energy position of group-III related transitions in the excitonic region along with the I_7 transition which is of unknown origin.

Transition	Impurity	energy position (meV)
I_6	Al	3360.9
I_8	Ga	3359.9
I_9	In	3356.8
I_7	unknown	3360.1
I_6^+	Al	3373.1
I_8^+	Ga	3371.8
I_9^+	In	3367.6
I_7^+	unknown	3372.5

Chapter 4

Study Of Group IV (C and Sn) Doped ZnO

4.1 Introduction

Group IV impurities, such as C, Si, Ge and Sn can in principle acts as donor impurities in ZnO, but have been much less studied [64, 65] and the microscopic details of these elements and their electrical properties have not been conclusively clarified. Among these elements carbon is a common unintentional impurity in MOCVD growth and it is important to understand its effects on the optical properties of ZnO in more detail [66–68]. There are relatively few reports of intentional carbon doping of ZnO.

Theoretical studies show that carbon most likely occupies cation sites and acts as a shallow double donor [69] since it contributes four valence electrons when substituting for a Zn atom which has only two valence electrons. Lyons et al. [69] have found that C_{Zn}^{2+} is the most stable configuration for carbon impurities in ZnO. However, experimental reports attribute both p-type [66] and n-type [70] doping characteristics to carbon-doped samples, and therefore, a systematic understanding of the electronic properties of C-doped ZnO is still lacking.

Lyons et al. [20] theoretically investigated the role of the group-IV impurities Si and Ge in ZnO and proposed that both impurities were n-type dopants occupying Zn sites. Having four valence electrons, Si and Ge could substitute for Zn and act as double donors (Si_{Zn}^{2+}, Ge_{Zn}^{2+}). The electronic nature of double donors in ZnO has not yet been explored. Cullen et al. [65] observed a transition at 3324 meV which they labeled DD_2 and attributed to

Ge impurity complexes in ZnO acting as donors. This transition was similar to the Y-line in that it exhibited a much larger spectroscopic binding energy than its thermal binding energy. This transition was previously observed in radiotracer techniques in a study of ZnO implanted with radioactive As and Ga (which decayed to Ge) [13, 71] and was therefore conclusively shown to contain Ge. There have been some reports on Ge-doping of ZnO during the growth by mixing ZnO by GeO [72] and Ge related luminescence [73, 74].

Si doping of ZnO [75] was also shown to produce changes in electrical conductivity. Recently Cullen et al. [64] have shown that the I_{10} line at 3353 meV, which had been observed several years earlier, actually contains substitutional Sn. This assignment was conclusive, based on the implantation of radioactive ^{117}Ag which eventually decays into stable ^{117}Sn. Meyer et al. [23] have also observed this line in Li- and Na-doped ZnO single crystals and suggested that it contains Li or Na, however this remains to be proven.

In this chapter we will study the effect of C- and Sn-doping on the optical properties of ZnO nanowires and bulk crystals, respectively. We have divided this chapter into three main sections. In section 4.2 we discuss carbon-doped ZnO NWs and the effect of carbon doping on the excitonic PL transitions. In section 4.3 we describe our studies of the lower energy regions in the PL spectra where two transitions (DAP and e,A^0) were observed in our carbon-doped ZnO NWs. Section 4.4 will focus on Sn-doping in ZnO bulk crystals grown at Oak Ridge National Laboratory. Part of this work is published in the J. Appl. Phys. 116, 053516 (2014) and J. Luminescence, 176,47 (2016).

4.2 Optical characterization of C-doped nanowires

Carbon is a common unintentional impurity during ZnO MOCVD growth, especially for the metalorganic vapor phase epitaxy (MOVPE) technique at low growth temperatures. It may act as an important compensating impurity during efforts to achieve n- or p-doping. It can in principle act as a double donor or double acceptor, or as a complex with other impurities or native defects [66–68]. However, a systematic understanding of the electronic properties of C-doped ZnO is still lacking. In this work we performed careful intentional carbon doping by the MOVPE method using a dilute mixture of carbon tertrachloride (CCl_4) gas in nitrogen (1000 ppm). CCl_4 has been widely used as a p-dopant in III-V semiconductors; its use in ZnO has not been previously reported. We also performed co-doping experiments in which small amounts of hydrogen were added to the gas mixture in order to enhance the

PL emission from the carbon-related defects. The carbon source available for this study was contained a mixture of natural carbon (CCl_4) diluted in nitrogen to 1000 ppm.

4.2.1 Effect of carbon doping on the excitonic region of the PL spectrum

Fig. 4.1 shows typical high-resolution PL spectra of the undoped and lightly C-doped ZnO NWs, in the bound-excitonic region, recorded at 4.2 K. The PL spectrum of the undoped

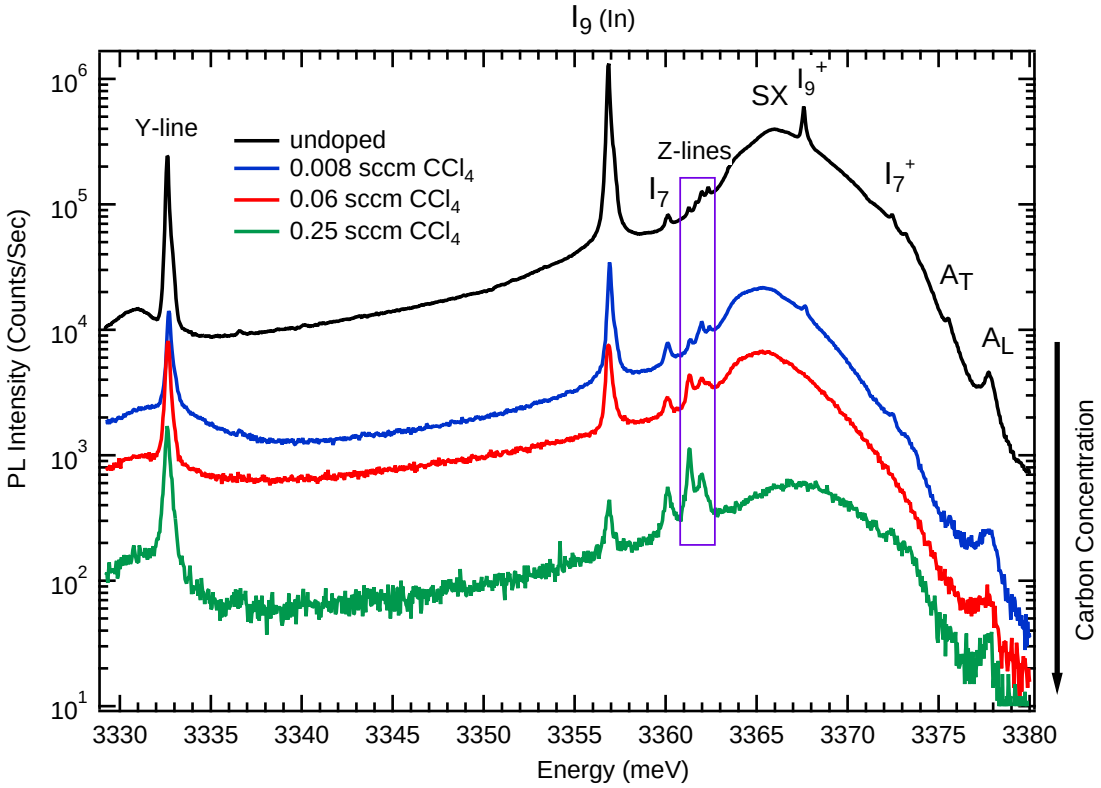

Figure 4.1: 4.2 K PL spectra of undoped and lightly carbon-doped ZnO NWs in the bound-exciton region. C-doping increases the intensity of the Z-lines relative to the I_9 PL intensity, while decreasing the overall intensity of the PL.

ZnO NWs shows several previously unreported emission lines in this region in addition to familiar lines. Among them we can identify the previously known donor bound-exciton transitions such as I_9 (In), I_7 (unknown), and their corresponding ionized bound-excitons along with Y-line, SX (surface exciton) and free excitons (FX). The bound-excitonic transitions are extremely sharp with linewidths as low as 0.15 meV, indicating the high quality of these NWs, and a very low level of inhomogeneous broadening due to strain. These exciton transitions are close to a set of four lines previously reported by Lautenschlaeger

et al. in unintentionally-doped bulk crystals, however, the exact energies are distinct from the present carbon-related features [76].

In addition to these well-known bound-excitonic transitions, several unidentified weak transitions are observed in the energy range 3360.8–3362.0 meV of the spectrum. These transitions show an increase in PL intensity relative to the residual I_9 transition as a function of increasing C concentration, suggesting that they may be associated with a defect containing carbon. We denote these unknown lines as Z-lines in order to distinguish them from the previously reported X-lines at slightly different energy positions for bulk ZnO crystals [76]. The overall PL intensity strongly decreases with increasing carbon concentration and no PL is observed for the NWs with CCl_4 flow $\geq$1.25 sccm. Mechanisms for this reduction in intensity will be discussed later.

4.2.2 Effect of hydrogen-carbon co-doping

The addition of small amounts of hydrogen together with the carbon dopant greatly enhances the intensity of the photoluminescence of carbon-doped ZnO NWs, as shown in Fig. 4.2. The hydrogen flow has been varied from 2 to 50 sccm in three steps with a fixed CCl_4 flow of 0.25 sccm. The PL spectrum of a sample doped only with 0.25 sccm CCl_4 is also shown for comparison. The overall PL intensity of all lines, not just the Z lines, increases monotonically with H concentration. The fact that all exciton emission increases with hydrogen concentration suggests that the effect of hydrogen is to reduce the concentration of nonradiative traps in the sample.

To further investigate the effect of H co-doping at higher carbon concentrations on the PL spectra, we have grown a series of C and H co-doped ZnO NWs with a fixed H_2 flow of 50 sccm while varying the CCl_4 flow from 0.25 sccm to 50 sccm. Fig. 4.3 shows 4.2 K PL spectra of the C and H co-doped ZnO NWs (c) –(g), as well as undoped and Al-doped control samples for the reference transitions Al (I_6), Ga (I_8), and In (I_9) D^0X lines (a) and (b). For the undoped (a) and lightly C-doped (c) NW samples, I_9 dominates and the intensity of the Z-lines is relatively low. With increasing C concentration, the PL intensity of the Z-lines increases relative to I_9 and becomes dominant at higher C concentrations. We can clearly identify four lines at 3360.8, 3361.2, 3361.7, and 3361.9 meV for highly C-doped NWs and denote them as Z_1, Z_2, Z_3, and Z_4, respectively. Increasing the carbon concentration in the presence of hydrogen not only enhances the overall PL signal but also increases the

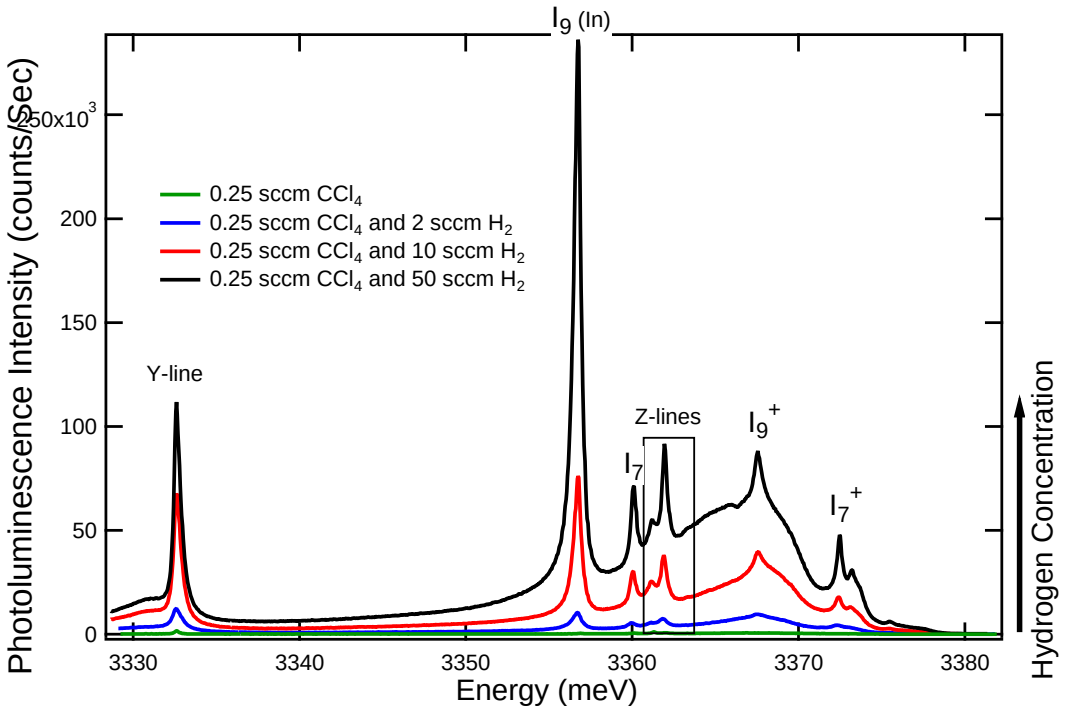

Figure 4.2: Effect of hydrogen codoping on the 4.2 K PL spectra of the 0.25 sccm CCl_4 doped ZnO NWs with H_2 concentration varying from 0 to 50 sccm.

integrated PL intensity of the Z-lines. This is in contrast to the case of samples doped only with carbon.

Fig. 4.3(b) shows the position of the Al D^0X transition in an intentionally Al-doped NW sample. The energy of the Z_1 transition is only 0.1 meV below the Al donor bound-exciton line (I_6, 3360.9 meV) as shown by the vertical lines in Fig. 4.3. The increase in integrated PL intensity of Z_1 with increasing C concentration confirms that Z_1 is not due to Al. Details of the effect of Al-doping on the PL spectra of ZnO NWs have been discussed in Chapter 3.

In addition to the Z-lines, we have also clearly observed the I_7 transition at 3360.1 meV. Unlike the Z-lines, the increase in I_7 PL intensity seen in some samples is not systematic with C concentration. Although the impurity associated with the I_7 transition is unknown, recent magneto PL studies confirmed that this transition is likely due to a D^0X transition [77] in agreement with our observation that I_7 has a D^+X transition as discussed in Chapter 3. Lavrov et al. [78] have recently reported a transition at 3360.1 meV, which exactly coincides with I_7 line position, and assigned it to excitons bound to hydrogen donors in the bond-centered lattice position, H_{BC}. However, it is worth mentioning that our sys-

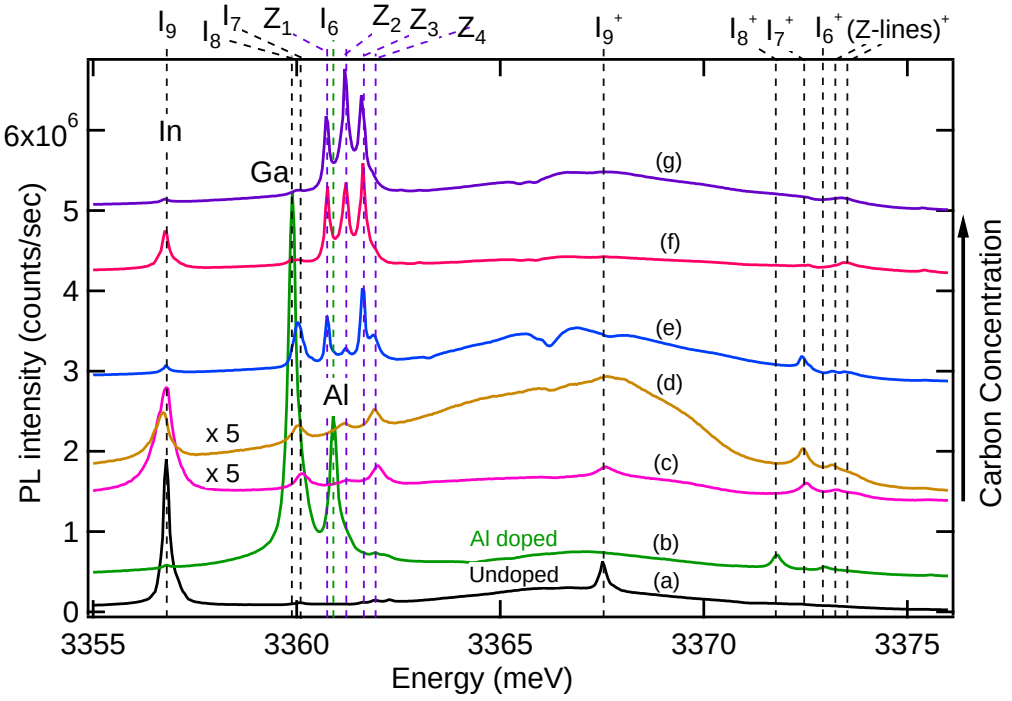

Figure 4.3: 4.2 K PL spectra of (a) undoped NWs, (b) Al-doped NWs. Spectra (c)–(g) were grown with a fixed flow of 50 sccm H_2 and varying CCl_4 flows of (c) 0.25 sccm, (d) 2.3 sccm, (e) 10 sccm, (f) 30 sccm, and (g) 50 sccm co-doped ZnO NWs.

tematic PL studies of NWs doped only with H showed no increase in PL intensity of the I_7 line. Hence, I_7 is unlikely to be associated with H_{BC} centers.

4.2.3 Thermalization behavior of the Z-lines

Given that there are four closely spaced Z-lines, it is important to determine whether they originate from the same impurity center or arise from excited states of a common defect. The fact that Z-lines have different intensities in different samples demonstrates that the lines are due to distinct complexes. Temperature dependent PL measurement is a useful tool to determine the thermal activation energies of excitons and compare to their spectroscopic localization energies. For this purpose we carried out temperature-dependent PL measurements for the highest C and H co-doped NWs that showed very strong Z_1, Z_2, and Z_3 lines.

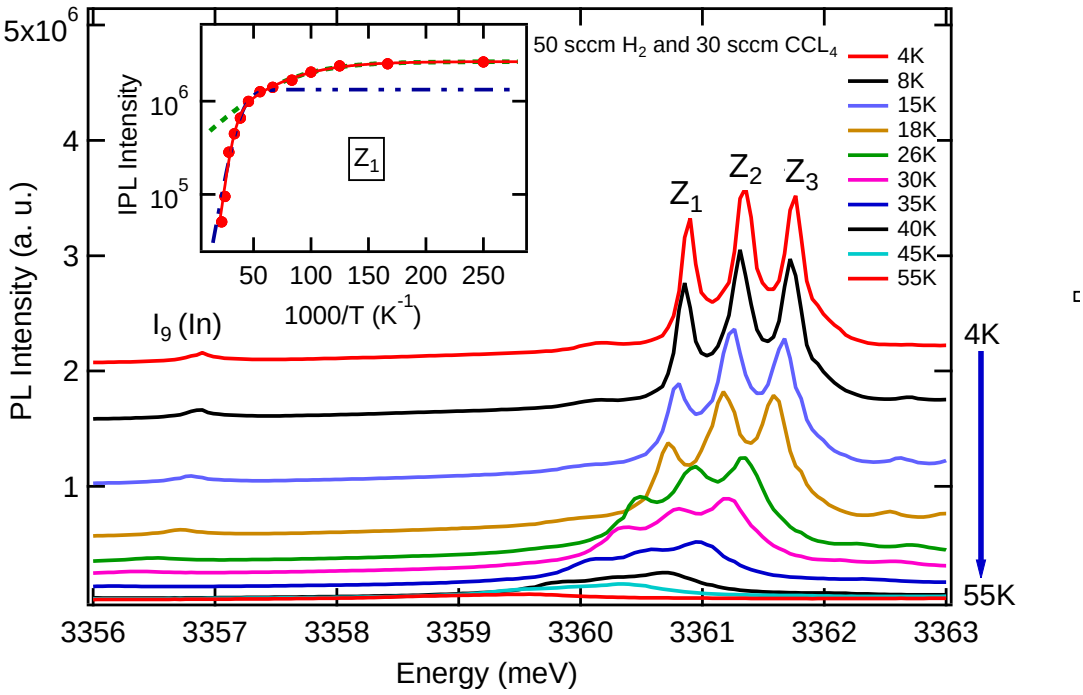

Figure 4.4: Temperature dependent PL spectra of 30 sccm C and 50 sccm H codoped ZnO NWs from 4.2 to 55 K. Inset shows the integrated PL intensity versus inverse temperature for Z_1.

Fig. 4.4 shows the PL measurements of the 30 sccm C and 50 sccm H co-doped ZnO NWs at different temperatures from 4.2 to 55 K. Typically excited states of D^0X transitions, such as D^0X^B, where the hole is from the B valence band should exhibit very low intensity at the lowest temperatures, with increasing intensity at intermediate temperatures as the excited state becomes occupied [60]. At T = 15 K a new transition at 3362.6 meV appears and increases in intensity at higher temperatures. This transition is 1.4 meV above the Z_2 line and is likely an excited state of Z_2. However, the integrated PL intensity of the Z-lines (Z_1, Z_2, and Z_3) has a maximum at the lowest measurement temperature of 4.2 K, slowly decreasing with increasing temperature up to around 20 K, and falls rapidly for temperatures above 20K. This is the typical thermalization behavior of the ground state D^0X transitions as observed for I_6, I_8, and I_9 [23].

The inset of Fig. 4.4 shows that the integrated PL intensity of Z_1 versus inverse temperature could not be fitted for the entire range with one activation energy given by the simplified Boltzmann statistics. We have therefore used Eq. 1.7 to fit the data and obtained

Table 4.1: Thermal activation energies obtained from the temperature-dependent PL measurements.

BX	E_1 (meV)	E_2 (meV)	C_1	C_2	E_{loc} (meV)
Z_1	2.6 ± 0.2	19.7 ± 3.5	6.34	5420.4	14.7
Z_2	1.5 ± 0.3	17.7 ± 1.3	0.92	5905	14.3
Z_3	1.7 ± 0.8	16.8 ± 2.4	0.7	505	13.8

the fitting parameters as listed in the Table 4.1. The first activation energy of the Z_2 line (E_1) is about 1.5 meV which is close to the 1.4 meV separation between Z_2 line and the above mentioned excited state transition. Similar thermalization behavior was observed for the other Z-lines (Z_2 and Z_3), which are shown in the Fig. **??** in the Appendix. C. The localization energies (E_{loc}) are shown in Table 4.1 as well which are just about in agreement given the uncertainties in the values of the thermal activation energies (E_2).

With increasing temperature, the Z-lines exhibit a redshift as observed for the I_9 transition. The observed red shift of 1.3 meV, when increasing the temperature from 4.2 to 45 K, is identical to that of the I_9 transition. This is very much different from the behavior of the much deeper Y-lines, which showed more red-shift compared with the I_6 transition for the same temperature range [38]. Hence the dependence of the energy positions of the Z-lines with increasing temperature is very similar to the characteristics of shallow D^0X transitions.

4.2.4 Two-electron-satellites (TES) and deviation from Haynes rule

As we discussed in Chapter 2, when an exciton bound to a donor impurity recombines, it may leave the donor in one of its excited states. The observation of these TES transitions is the signature of a D^0X and not a D^+X or isoelectronic transition, for example. In the previous chapter we have unambiguously identified the TES transitions of the group-III donors in systematically doped ZnO NWs. Fig. 4.5 shows the principal (1s) D^0X transitions of I_8 (Ga), the Z-lines, and the corresponding TES region for undoped and highly C and H co-doped NW samples.

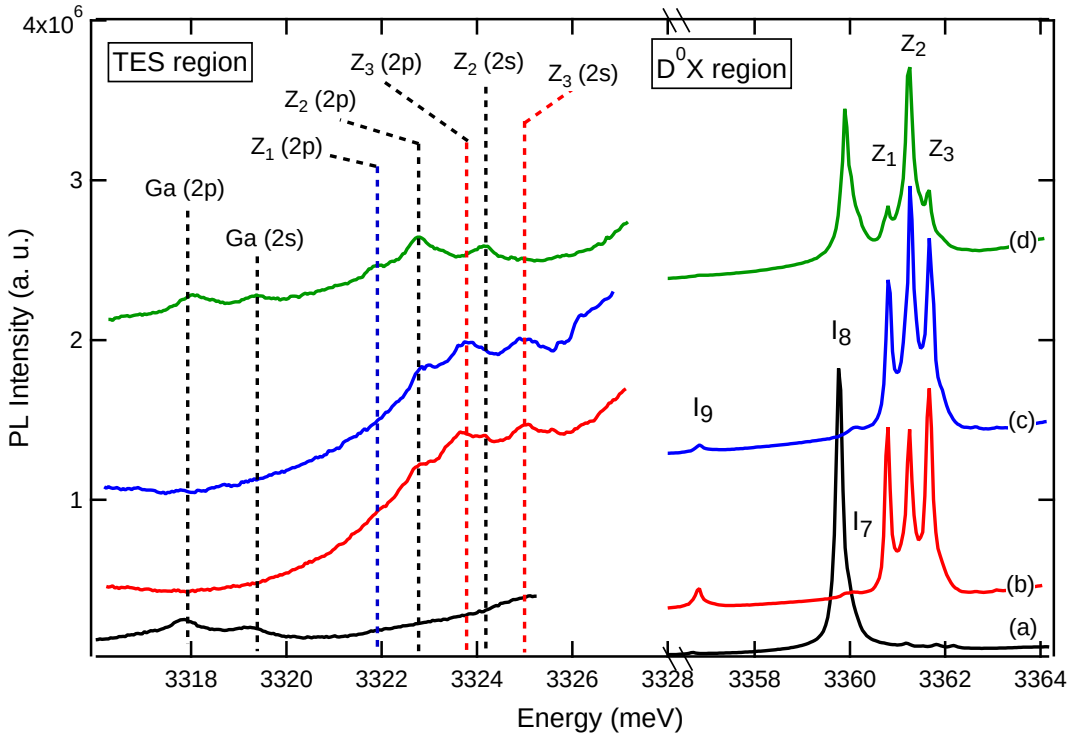

Figure 4.5: TES transitions of (a) undoped and (b), (c) and (d) highly carbon and hydrogen co-doped ZnO NW samples.

The PL spectrum of undoped NWs (Fig. 4.5(a)) exhibited a very strong I_8 transition and corresponding Ga 2p and 2s TES transitions at 3317.9 and 3319.3 meV, respectively, consistent with previously reported energies [23]. Fig. 4.5(d) shows strong I_8 and Z_2 lines as well as Ga 2s and 2p TES transitions and new transitions at 3322.8 and 3324.1 meV. Considering the strong PL intensity of the Z_2-line, we assign these new lines to TES transitions of Z_2 with energies 3322.8 meV (Z_2- 2p) and 3324.1 meV (Z_2-2s). Another weak transition at 3321.9 meV may be related to Z_1, most likely Z_1-2p. It is worth mentioning that these TES transitions of Z_1 and Z_2 lines are distinct from the known Al-TES transitions, observed at 3321.3 meV (Al-2p) and 3322.3 meV (Al-2s) and reported in Chapter 4. PL spectra shown in Fig. 4.5(b) and (c) exhibited relatively strong Z_3 line emission compared with the sample in Fig. 4.5(d) and thus, in addition to Z_2-TES, we have observed new transitions at 3323.6 meV and 3324.9 meV. These transitions are 0.8 meV above the TES of Z_2 and we have assigned the former to Z_3- 2p (3323.6 meV) and the latter to Z_3-2s (3324.9 meV). We did not observe any TES line related to Z_4 in any of these samples. The donor binding

energy can be estimated from the relation $E_D = (E_{1s} - E_{2p}) + 12.6$ meV. Therefore the binding energies of the impurities associated with the Z_1, Z_2, and Z_3-lines are calculated to be 51.5±0.3 meV, 51.0±0.2 meV, and 50.7±0.2 meV, respectively.

Fig. 4.6 shows a plot of D^0X localization energy vs. donor binding energy for I_6, I_8, I_9, and the Z-lines (Z_1, Z_2, and Z_3). The group-III donors show highly linear behavior (Haynes

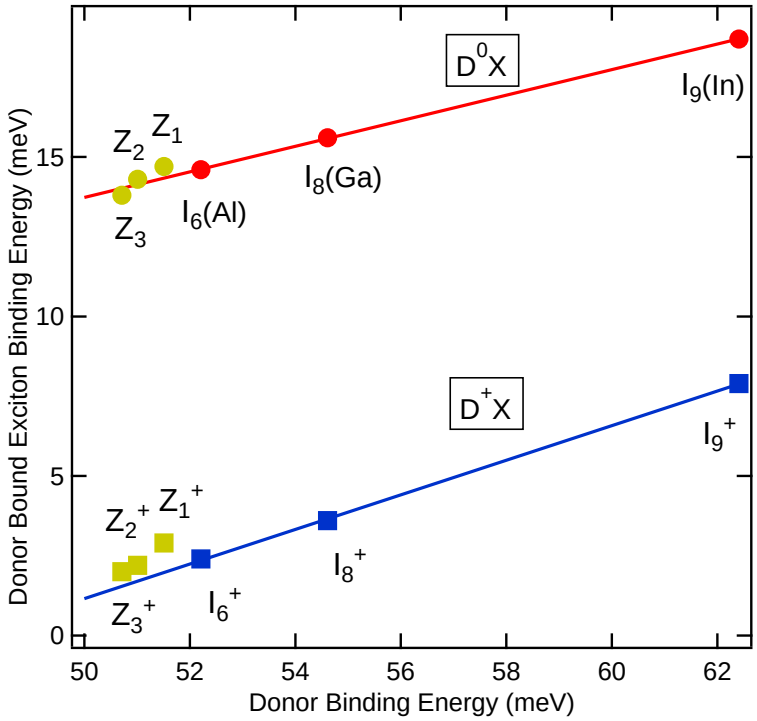

Figure 4.6: Localization energy vs. donor binding energy for Al, Ga, and In-D^0X transitions and Z-lines (estimated from TES lines).

rule) and the data points for Z_1, Z_2, and Z_3 fall close to the same straight line. Table 4.2 lists a summary of the TES transitions and binding energies of Z-lines.

4.2.5 Excitons bound to ionized centers corresponding to Z-lines

Additional lines corresponding to D^+X transitions of the Z-line transitions were also observed in a large number of samples. Fig. 4.7 shows high-resolution PL spectra of Al-doped and C- and H- co-doped ZnO NWs measured at 4.2 K measured in the D^0X and D^+X region. As we showed in chapter 4, the D^+X transitions of Ga (I_8^+), Al (I_6^+) and In (I_9^+) donors are observed at 3371.8, 3373.1 and 3367.6 meV, respectively. The C-doped samples (Fig. 4.7-(b) and (d)) showed only the I_7 transition and no signature of I_8 was observed.

As expected, we do not observe I_8^+, but only the transition at 3372.5 meV which we have assigned unambiguously to the I_7^+ in the discussion in Sec. 4.2.2.

The intensity of some of the transitions shown in the D^+X region in Fig. 4.7 has a strong correlation with different Z-lines. For example, the samples that showed only Z_2

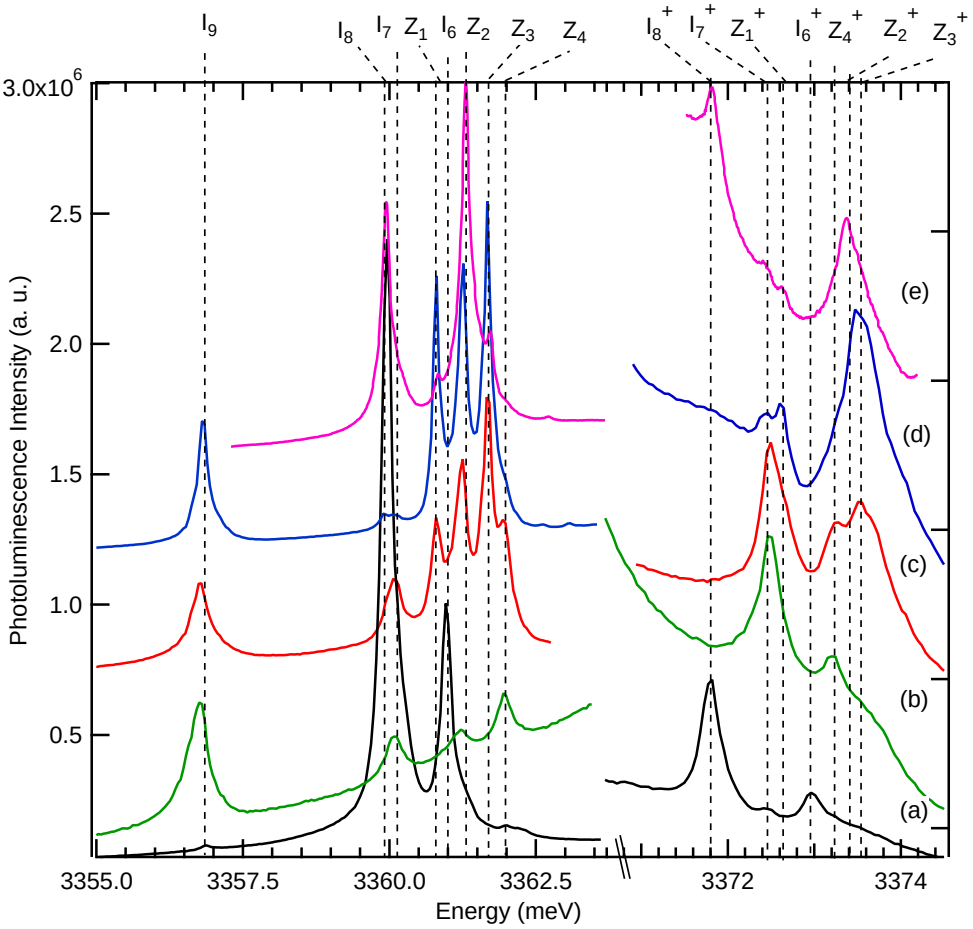

Figure 4.7: High-resolution PL spectra of (a) Al-doped and (b)–(e) C- and H- codoped (50 sccm) with C concentration varying from (b) 2.3 sccm, (c) 10 sccm, and (d)–(e) 50 sccm CCl4.

and Z_4 lines (Fig. 4.7-(b)) exhibited transitions at 3372.5 meV (I_7) and 3373.2 meV. The fact that the Z_4 line is relatively strong compared with the Z_2 line for this sample indicates that the transition at 3373.2 meV corresponds to the D^+X transition of the Z_4 line. This is confirmed for sample (d) that showed a very weak Z_4 line, and hence the Z_4^+ at 3373.2 meV was also very weak. However, the sample (e) showed a very strong Z_2 line and no Z_4 line and a new transition at 3373.3 meV in the D^+X region. This transition at 3373.3 meV

is not present when the Z_2 line is relatively weak. Hence the transition at 3373.3 meV is assigned to Z_2^+, the D^+X of the Z_2 line.

Samples (c) and (d) showed strong Z_1, Z_2, and Z_3 lines, whereas the Z_4 line is weak. We have also observed a doublet at 3372.5 meV and 3372.6 meV. The former is I_7^+ and the latter must be associated with Z_1^+, which are 0.1 meV below I_6 and 0.7 meV above I_7. Moreover, the transition at 3372.6 meV is observed only when the Z_1-line is present. Similarly, the transition at 3373.5 meV shows a very strong correlation with the Z_3-line. As we can clearly see in samples (c) and (d), the integrated PL intensity of the Z_3-line increases while going from samples (c) to (d) and we also observed an increase in PL intensity of the transition at 3373.5 meV. We do not observe this transition (3373.5 meV) when the Z_3-line is absent, while the Z_2 and Z_4 are present (see Fig. 4.7-(b)). This reveals that the transition at 3373.5 meV must be associated with the Z_3-line. Therefore, we assign the transitions at 3372.6 meV and 3373.5 meV to Z_1^+ and Z_3^+, respectively.

The D^+X versus D^0X energy positions are plotted for the Z-lines, I_7, and those of the group-III donors in Fig. 4.8.

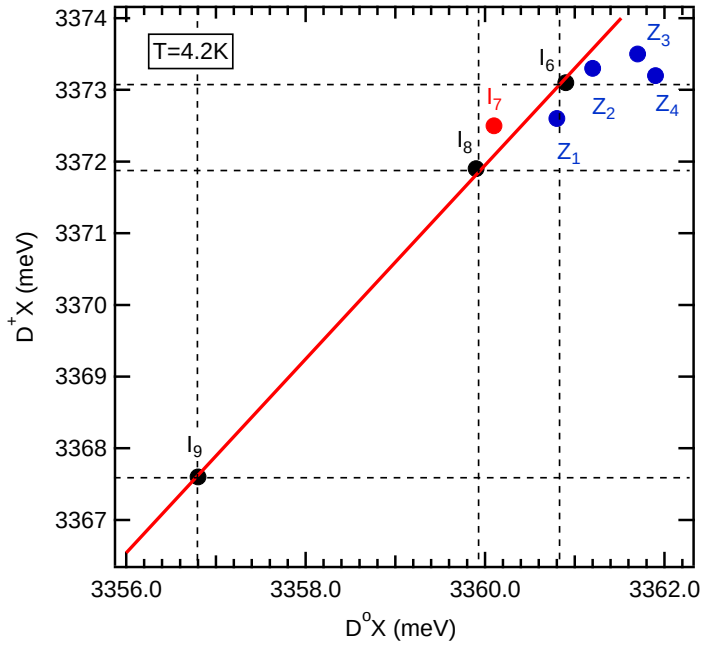

Figure 4.8: D^+X versus D^0X of group-III dopants, Al, Ga and In (I_6, I_8, I_9) showing almost linear behavior. The I_7 and Z-lines show a clear deviation from linear behavior.

A linear fit was applied only to the Al, Ga, and In donor related transitions and they all fall on the straight line [23]. The data points related to I_7 (red spot), Z_1 and Z_2 (blue spots) fall very close to this line while not true for Z_3 and Z_4.

4.2.6 Discussion

As shown in Fig. **??** in Appendix. B, NWs grown with higher carbon concentrations exhibited carbon-related graphitic D and G modes, at 1356 and 1598 cm^{-1}, respectively, in Raman spectra which were not present in the undoped sample. Graphitic (sp^2) carbon has been observed by several groups in unintentionally-doped ZnO grown by MOVPE, typically at low growth temperatures [66–68]. Park et al. [79] also observed a reduction in the intensity of photoluminescence of C-doped ZnO films compared to undoped material, which they attributed to non-radiative centers containing carbon. We observed similar results for heavily Sb-doped ZnO NWs that exhibited D and G modes and a simultaneous reduction in overall PL intensity at high Sb-doping levels (Chapter 5).
In the case of the Sb-doped samples, it is likely that the carbon originated from the trimethyl antimony precursor used as the doping source.
On the other hand, the increase in PL intensity after H co-doping coincides with the suppression of graphitic D and G modes observed by Raman spectroscopy. For example, the 10 sccm C-doped sample without hydrogen exhibited strong graphitic D and G modes, and no PL was observed (Fig. **??**). Co-doping with 50 sccm of H resulted in complete suppression of the D and G modes and strong PL emission. These results are in agreement with recent reports showing a reduction in graphitic Raman modes by annealing ZnO planar films in hydrogen [80]. The fact that all exciton emission increases with hydrogen concentration suggests that the effect of hydrogen is to reduce the concentration of non-radiative traps in the sample. Although it is known that hydrogen has been known to have passivating effect in Si [81], its role in our samples is not yet clear.

There are several theoretical and experimental reports of hydrogen in ZnO. Van de Walle [82] suggested that hydrogen can form a shallow donor in ZnO and acts as a source of conductivity. Hydrogen can be substituted in an oxygen site and forms an H_O defect [23, 78, 83]. Even at the maximum hydrogen flow (50 sccm) for these co-doped NW samples, there was no evidence of the I_4 line in the PL spectra. This indicates that the hydrogen co-doping does not generate the H_O defects although we cannot rule out the pos-

sibility of hydrogen incorporation at other lattice sites.

Meyer et al. showed that the hydrogen related I_4 line can be completely annealed out by heating the bulk ZnO crystals above 600^oC [23]. There are several reports about other forms of hydrogen defects in ZnO which also anneal out at temperatures above 190^oC [78] and 300^oC [84]. In contrast, the Z-lines are highly stable even after annealing at 900^oC under N_2O. Hence, it is highly unlikely that the donor defects responsible for the Z-lines contain hydrogen. It is likely that hydrogen plays a role at the surface, for example, by reducing the formation of non-radiative carbon clusters, or by modifying the concentration of native defects at the growth surface.

It is worth noting that chlorine is also one of the chemical components of the carbon-doping source used in this study (CCl_4) and it could be involved in the combination of some of the Z-lines complexes. Cl was identified as a shallow donor in the electron paramagnetic resonance studies [85]. This needs to be investigated further by careful doping of ZnO with Cl. To date, there are no confirmed reports of shallow D^0X from Cl donors. The donor binding energy of Cl is also unknown.

The deviation of the Z-lines from Haynes rule is negligible compared to other reported defects like the Y-line and Ge DD_2 center. However, there is a systematic shift from the group-III donor behavior that suggests some differences in the core electronic structure of the defect responsible for the Z-lines. Based on the correlation of PL intensity with carbon doping concentration it is highly likely that the defects related to Z-line transitions contain carbon in addition to some other native constituents, such as Zn_i and O_V. The fact that several Z-lines are observed in the PL spectra of these samples with varying intensity ratios coupled with the lack of thermalization between the individual Z-lines suggests that they are different defects. Table 4.2 gives a summary of the D^0X and D^+X transitions of the Z-lines discovered during the course of this thesis.

Table 4.2: Summary of the D^0X and D^+X transitions of the Z-lines and their corresponding TES transitions. Absolute energy uncertainties are ±0.1 meV.

D^0X transitions		TES transitions and donor binding energies (meV)			D^+X transitions	
Line	Energy	2s	2p	E_b	Line	Energy
Z_1	3360.8	3321.9	-	51.5±0.3	Z_1^+	3372.6
Z_2	3361.2	3324.1	3322.8	51±0.2	Z_2^+	3373.3
Z_3	3361.7	3324.9	3323.6	50.7±0.2	Z_3^+	3373.5
Z_4	3361.9	-	-	-	Z_4^+	3373.2

4.3 Free-to-bound and donor–acceptor–pair emissions

Free-to-bound (e,A^0) and donor-acceptor-pair (DAP) transitions in ZnO are particularly interesting since they have been observed in a variety of ZnO samples, undoped or intentionally doped with various dopant species, particularly group-V elements. The knowledge of the dependence of these emission lines on the growth conditions is desirable since they offer insight into the physics of acceptors in ZnO, which are urgently needed for device applications.

Conclusive evidence for acceptor impurities in ZnO comes from two PL signatures: DAP emission and e-A^0 emission . For example, a DAP band in the range 3.21-3.24 eV has been observed in N-doped ZnO materials [31, 42, 43, 86], corresponding to an acceptor binding energy in the range 160-180 meV. Additional PL evidence for acceptor behavior in ZnO comes from reports of free-to-bound PL emission in ZnO at around 3310 meV [45]. Based on a localization energy of the bound-particle of around 130 meV, it was concluded that the band originates from free electrons recombining with holes bound to acceptors (e,A^0) in the vicinity of crystal defects, e.g. basal plane stacking faults.

In this section, we have studied two distinct transitions in carbon and carbon-hydrogen co-doped ZnO nanowires, and have assigned them to previously identified DAP and (e,A^0) transitions from two distinct acceptor impurities, based on excitation power-dependent,

temperature-dependent, and time-resolved PL measurements. The time resolved photoluminescence was done at Technical University of Berlin in Germany.

4.3.1 Steady state photoluminescence

Fig. 4.9(a) shows typical high-resolution 4.2 K PL spectra of undoped and doped ZnO NWs, in the (D^0X) region. These samples are undoped, 0.5 sccm carbon doped (sample A) and 30 sccm carbon and 50 sccm hydrogen co-doped (sample B). The PL spectrum of the undoped ZnO NWs shows excitonic lines at 3360.1 and 3356.8 meV (I_7 and I_9), respectively. Their corresponding D^+X are also observed at 3372.5 and 3367.6 meV, respectively. The sharp linewidths indicate the high purity of these NWs.
In addition to these transitions, Z-lines and Y-lines are also observed. According to our discussion in section 4.2.1, carbon doping increases the intensity of the Z-lines relative to the I_9 transition, while decreasing the overall intensity of the PL. As can be seen from Fig. 4.9(a), the Z-lines are much more intense in the co-doped samples and dominate the PL spectrum.

First we will discuss the lower energy region of the sample doped only with carbon. We will show that the observed bands are consistent with DAP emission. The PL spectra of the lower energy range for these samples are shown in Fig. 4.9(b).

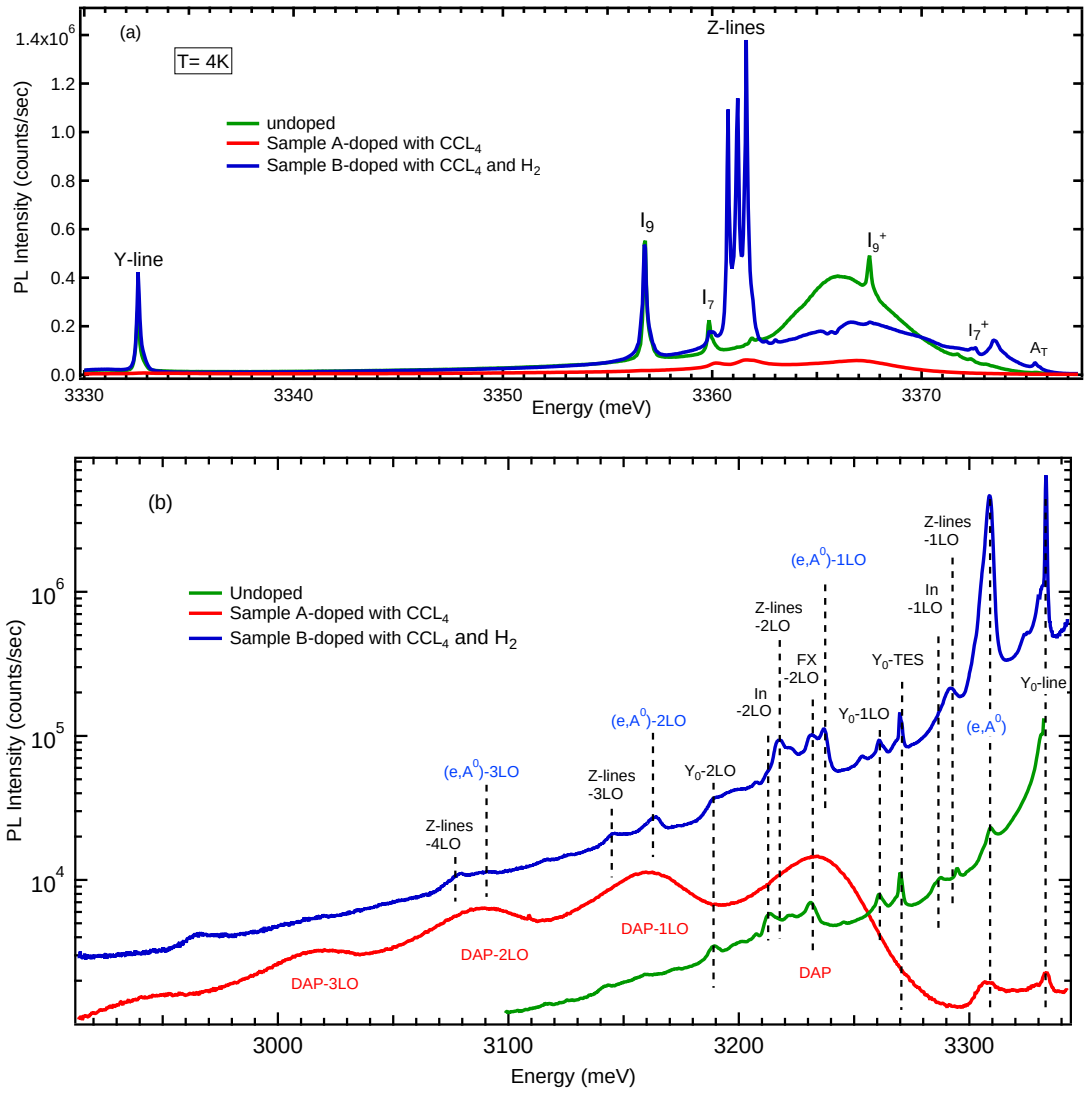

Figure 4.9: 4.2 K PL spectra of the undoped, carbon doped (sample A) and carbon and hydrogen co-doped (sample B) ZnO NW in the (a) bound-excitonic and (b) lower energy regions.

The PL spectrum of sample A (carbon doping only) exhibited a transition at 3236.7 meV with its clearly structured phonon replicas at a multiple of 72 meV lower energy. Strong phonon replicas are typical of DAP in compound semiconductors and originate from the electron-LO phonon coupling of the donor/acceptor states to the polar lattice. Both sets of samples exhibit an extra transition at 3308.8 meV. This transition is several orders of magnitude stronger in the hydrogen co-doped sample B. For this transition the phonon replicas are much weaker, consistent with a different physical recombination mechanism.

We will show that the transitions at 3308.8 and 3236.7 meV in samples A and B are due to free-to-bound (e,A^0) and donor-acceptor pair (DAP) recombination at two distinct acceptors. In order to further investigate the origin of these peaks, they are characterized in terms of their dependence on temperature, excitation power, and time decay dynamics.

4.3.2 Temperature and power dependent measurements

The temperature-dependence of the PL spectra of sample A is plotted in Fig. 4.10 in the temperature range from 4 to 200 K. The thermal quenching of the DAP luminescence happens at temperatures higher than 160 K. No evidence of free-to-bound transitions (e-

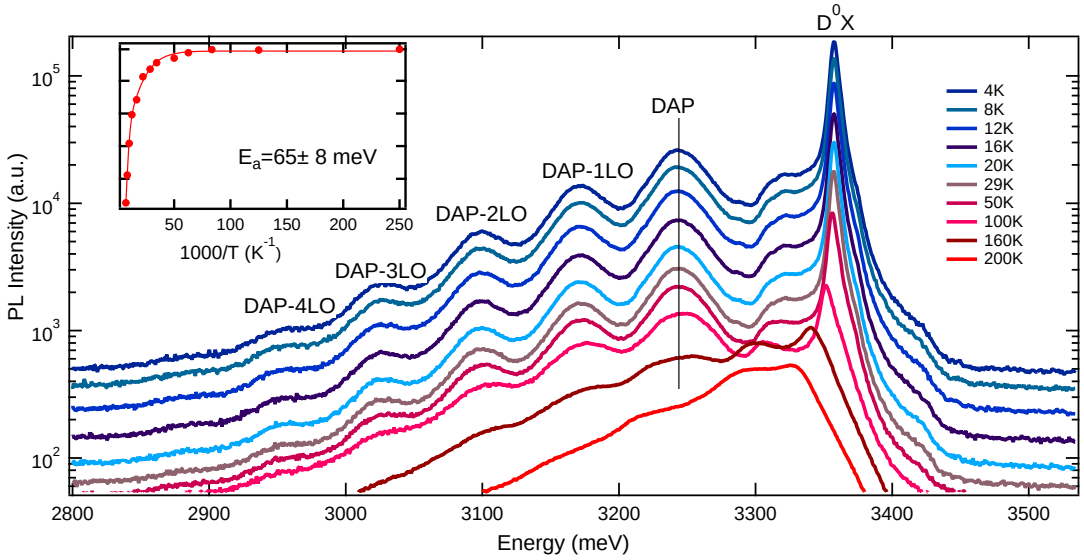

Figure 4.10: Temperature-dependence of the DAP transition in carbon doped ZnO NWs from 4.2 K to 200 K. Inset: Integrated PL intensity versus inverse temperature

A^0) related to this transition is observed at higher temperatures.

The integrated intensities of the zero phonon DAP lines vs. temperature is plotted in the inset of the Fig. 4.10. These results have been fitted with a simple Boltzmann statistics model, $I_{PL}(T) = \frac{I_0}{1+C\exp^{-E_a/k_BT}}$ where I_0 and C are constants, k_B is Boltzmann's constant and E_a is the activation energy. After fitting, the activation energy of the DAP line is estimated to be 65 $\pm$ 8 meV. This value is in the range of typical shallow donors in this sample such as In and C with donor binding energies of 61.9 and 51 meV.

Fig. 4.11 shows PL measurements as a function of excitation power for sample A (left

panel) and sample B (right panel). At low temperatures, the energy of the emitted photon

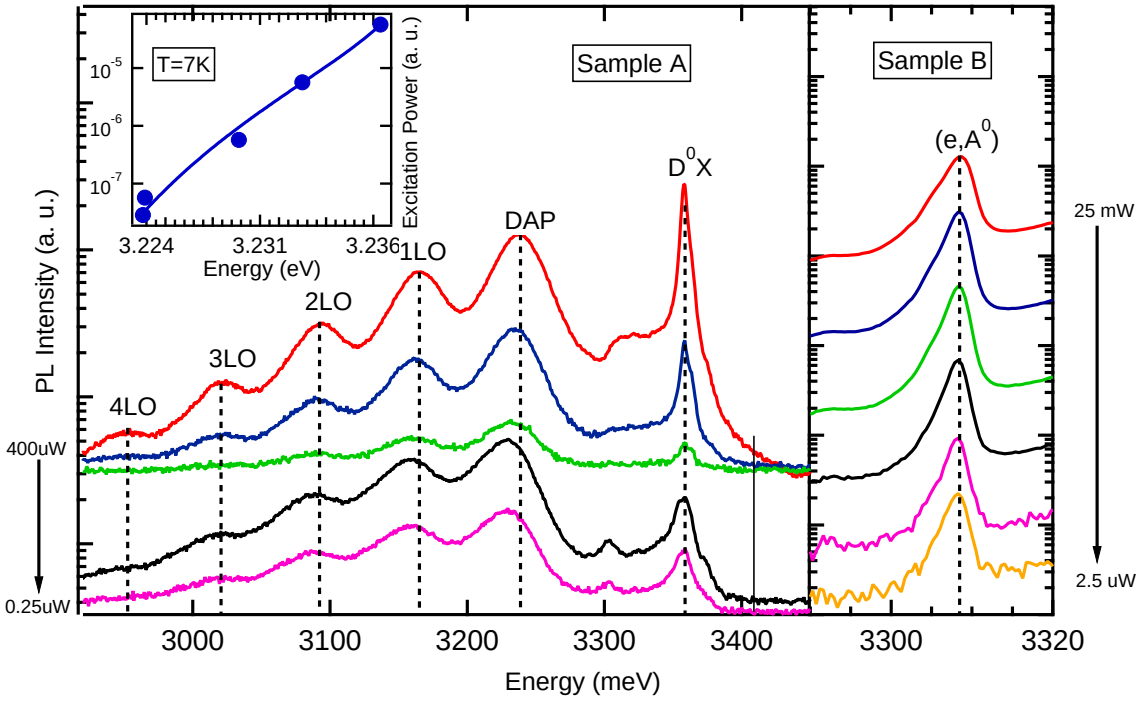

Figure 4.11: Excitation power dependent PL measurements done for sample A (left) and sample B (right). The inset figure is variation of peak energy position with excitation power in sample A (log scale) and the solid line is a fit to Eq. 4.2.

$E_{DAP}(r)$ of a DAP recombination is given by [87]

$$E_{DAP}(r) = E_g - (E_A + E_D) - E(r). \tag{4.1}$$

where E_A and E_D are the acceptor and donor binding energies, respectively. $E(r) = -\frac{e^2}{4\pi\epsilon r}$ is the Coulombic interaction energy of the ionized donor-acceptor pair separated by distance r, and ϵ is the dielectric constant.

Fig. 4.11 clearly shows that the DAP transition energy blueshifts with increasing excitation power intensity because of the saturation of long distance DAP as follows from Eq. 4.1. This behavior unambiguously confirms the presence of a DAP recombination process. The dependence of peak energy of a DAP band on excitation power provides information about the binding energies of the relevant donors and acceptors. The peak energy of the DAP emission $h\nu_m$ is related to the excitation intensity I_{ex} by [88]

$$I_{ex} = \left[\frac{(h\nu_m - h\nu_\infty)^3}{(h\nu_B + h\nu_\infty - 2h\nu_m)}\right] \exp\left(-2\frac{h\nu_B - h\nu_\infty}{h\nu_m - h\nu_\infty}\right). \tag{4.2}$$

where $h\nu_\infty = [E_g - (E_A + E_D)]$ is the photon energy corresponding to an infinitely distant donor-acceptor pair, $h\nu_B$ $[= E_g - (E_A + E_D) + e^2/\epsilon R_B]$ is the emitted photon energy of a donor-acceptor pair separated by a shallow impurity Bohr radius R_B. The solid line in the inset of Fig. 4.11 is a nonlinear least square fit to the experimental data giving the values of $h\nu_\infty$ and $h\nu_B$. The fit parameters obtained from a fit of experimental data to Eq. 4.2 are listed in Table 4.3.

Table 4.3: Values of fitting parameters of Eq. 4.2.

DAP (meV)	$h\nu_\infty$ (meV)	$h\nu_B$ (meV)	E_A (meV)
3236.7	3209.9	3268.4	176

We obtained an acceptor binding energy of 176 meV from the fit assuming the dominant donors in this sample are carbon-related with a binding energy of 51 meV [89] based on the observation of the Z-line D^0X peak. This acceptor binding energy is in agreement with the previously reported values for acceptor binding energies in nitrogen-doped ZnO [16, 17, 42]. On the other hand, the energy position of the line at 3308.8 meV did not change with the excitation power density measurements as shown in Fig. 4.11 (right figure).

Next we turn our attention to the sample B, co-doped with hydrogen and carbon which exhibits a dominant broad peak at 3308.8 meV (fig. 4.9). We will show that the dominant emission here is due to a free-to-bound (e-A^0) transition. There is uncertainty in assigning the transition at 3310 meV to (e,A^0) or DAP or A^0X [33, 41, 45, 90]. There are some claims that (e,A^0) in ZnO is due to recombination of free electrons with acceptors located at basal plane stacking faults [91]. Schirra et al. presented evidence based on cathodoluminescence and transmission electron microscopy (TEM) that the 3.31 eV line is due to the recombination of free electrons to bound acceptors localized at stacking faults [45]. Tainoff et al. suggested, according to the emission from their microcrystalline samples, that this defect is of crystalline origin [92]. Fig. 4.12 shows temperature-dependent photoluminescence of sample B in the range of 4 to 105K. The emission line at 3308.8 meV is the strongest line. It is noteworthy to mention that as we added hydrogen in the presence of CCl_4 the emission at 3308.8 meV greatly increased and is several orders of magnitude stronger compared to

the PL of undoped ZnO at this energy.

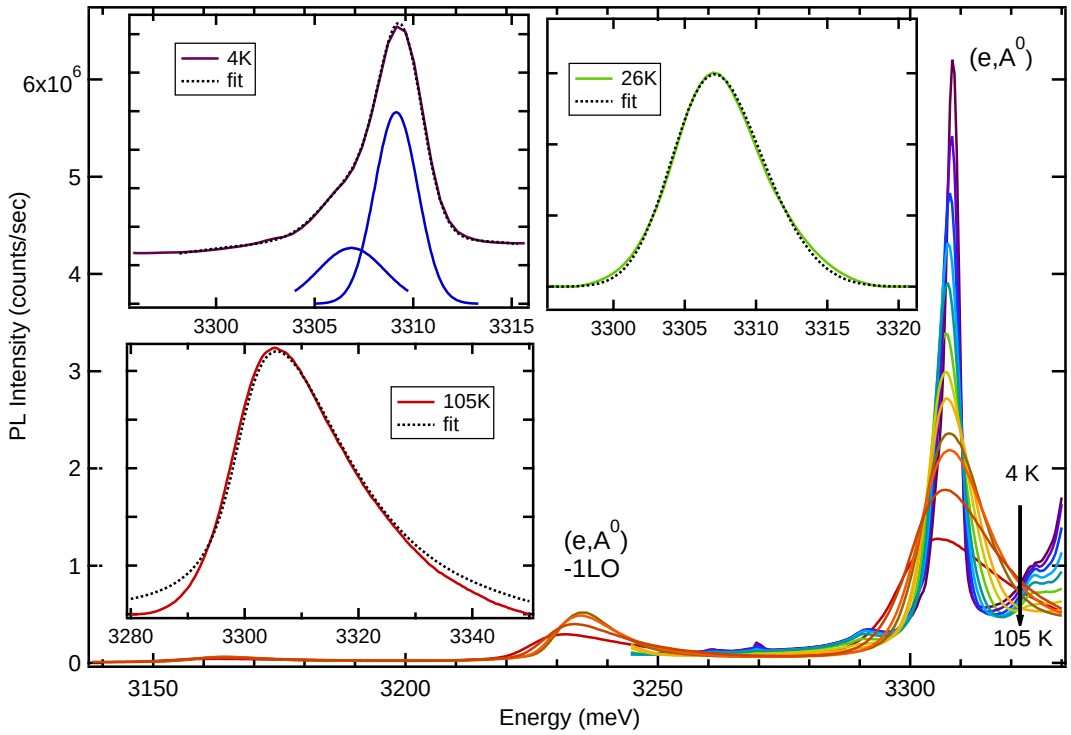

Figure 4.12: Selected temperature-dependent PL of sample B in the lower energy region. The inset figures are (e,A^0) transition at 4, 26 and 105 K with the fitted lines which are the convolutions of Eq. 4.1 with Gaussian (for 26 K) and Lorentzian (for 105 K) functions.

The assignment of this line to an (e-A^0) transition is based on the rather asymmetric lineshape observed at higher temperatures, coupled with its temperature-dependence.

In order to evaluate the validity of the (e-A^0) model to our data, we began with a lineshape analysis at different temperatures as shown in Fig. 4.12. For low temperatures (4.2 K) we fit the line with the superposition of two Gaussians, where the first one corresponds to a weak unidentified peak at low energy, and the dominant one (FWHM = 2.5 meV) reproduces the statistical energy distribution of the acceptor states. For higher temperatures we used the ideal line shape equation for an (e,A^0) transition convoluted with a Gaussian. This is given by the product of the density of the electron states in the conduction band and the Fermi distribution, which can be approximated by the Boltzmann distribution for

nondegenerate doping, [93]

$$I(h\nu) = \sqrt{h\nu - (E_g - E_A)}e^{-[h\nu-(E_g-E_A)]/kT} \tag{4.3}$$

where $I(h\nu)$ is the intensity, E_g is the temperature-dependent bandgap and E_A is the acceptor binding energy.

In the higher temperature fits (T > 4.2 K) we assumed the electron temperature was the same as the experimental lattice temperature. In order to fit the line better, especially at the lower energy tail, we used the convolution of a Gaussian (for 26 K with FWHM = 3.5 meV) or a Lorentzian (for 105 K with FWHM = 9.4 meV) with Eq. 4.3. From these fits we derived an acceptor binding energy of 133 ± 5 meV which is in agreement with the value of 130 meV reported by Schirra et al. [45] This is significantly different from the acceptor binding energy estimate obtained for the DAP band in the carbon doped samples, and points to a different physical origin. In addition, no DAP band corresponding to the 130 meV acceptor was observed even at 4.2 K.

The strong (e,A^0) transition at low temperature indicates that the donors are being saturated more easily in these samples, resulting in excess free electron density. This may indicate possible p-type behavior in these samples, or at least a high degree of compensation. During the SEM microscopy of these samples a strong charging effect was observed which could be related to the high degree of compensation in these samples.

4.3.3 Time resolved photoluminescence

In order to further verify our assignments of the 3236.7 and 3308.8 meV transitions to DAP and (e,A^0) in samples A and B, respectively, time resolved PL (TRPL) measurements were performed. I begin with a discussion of the DAP band in sample A doped only with carbon. Fig. 4.13 displays the PL transients (open circles) at fixed spectral energy positions of the DAP band marked with labels A to I in the inset figure for sample A. Due to the statistical distribution of donors and acceptors in the crystal every acceptor will be in a different environment, which causes a distribution of lifetimes.

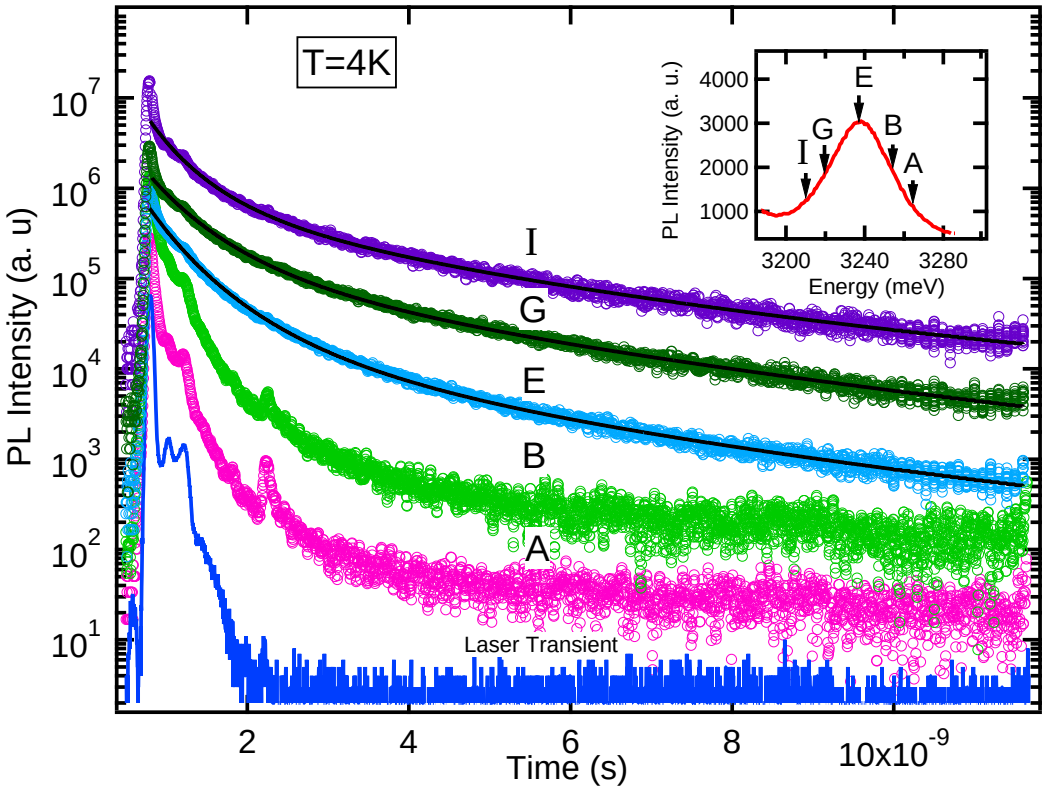

Figure 4.13: Decay of DAP photoluminescence intensity at 3262.9, 3255.06, 3233.5, 3219.81 and 3208.27 meV (marked A-I) as can be seen from the inset in sample A. The solid lines are the fits to Eq. 4.2, see text.

As shown in Fig. 4.13, all the measured transients show multi exponential behavior as well as the expected longer decays for distant pairs due to decreased wave function overlap.

Thomas and Hopfield [87] analyzed the decay kinetics of DAP recombination and their analysis has been applied to other materials like GaN [94], ZnSe [95] and ZnO [88]. Based on their theory, the intensity, $J_E(t)$, of the emitted DAP photons with energy E at a time t is given by

$$J_E(t) = W(r)\exp(-W(r)t) \times \exp\left[4\pi N_D \int_0^\infty \{\exp[-W(r)t] - 1\}\, r^2 dr\right] \qquad (4.4)$$

The recombination rate is $W(r) = W_0 \exp(-2r/a_D)$, where W_0 is the recombination constant and a_D is the Bohr radius of the shallow donor. The dynamics of the DAP decay according to Eq. 4.4 are determined by the parameter set of W_0, N_D, a_D and E_A. The pair

separation r was calculated from the DAP recombination energy, given by Eq. 4.1.

We assumed E_g=3436 meV [43] and E_D=51 meV [89]. The solid lines in Fig. 4.13 represent the best fits to the data using $W_0 = 2.8\times10^{12}$ s^{-1}, $N_D = 3.6\times10^{18}$ cm^{-3}, $a_D = 1.6$ nm and E_A =181±5 meV. The estimated acceptor binding energy is in agreement with the 176 meV calculated from the excitation power intensity analysis presented earlier in the previous section.

The decay transients were also measured for higher energy positions, like the position labeled A in the DAP band (inset, Fig. 4.13), and showed shorter lifetimes compared to the lower energy positions, confirming the DAP assignment.

Fig. 4.14 shows time resolved data for the (e-A^0) line in the carbon-hydrogen doped sample (sample B). Transients from I_9 at 3356.8 meV and the free-to-bound transition at

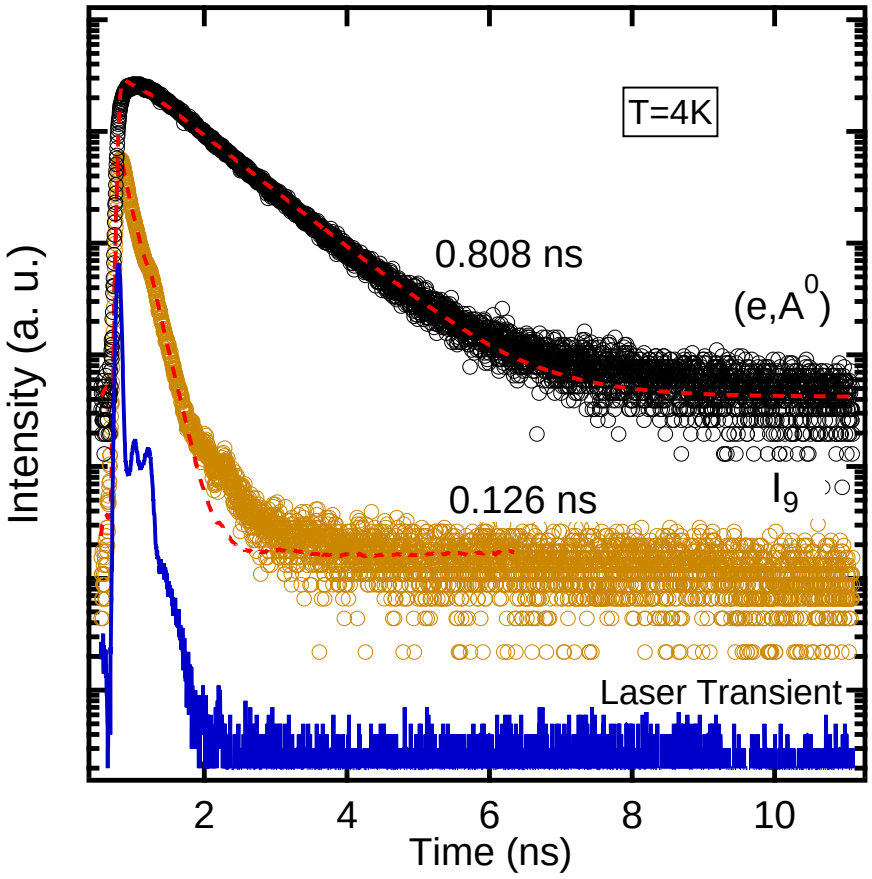

Figure 4.14: Low-temperature time-dependent PL intensity at I_9 and (e,A^0) positions for sample B. The symbols are experimental data and the solid lines are the fitted curves assuming monoexponential decay.

Table 4.4: Energy position and binding energies of the acceptor related transitions in samples A and B

sample doping	Energy position (meV)	Line identity	Acceptor binding energy (meV)
Carbon (sample A)	3236.7	DAP	181±5
Carbon-hydrogen(sample B)	3308.8	(e-A^0)	133±5

3308.8 meV at 4 K are compared. The experimental results (symbols) are fitted with exponential decays (dashed lines) of the form $I(t) = \sum_i A_i \exp(-t/\tau_i)$. The lifetime of the (e,A^0) transition is well described by a single exponential time constant of 808 ps. The D^0X lifetime is considerably shorter than the (e,A^0) transition. Urgessa et al. [96] reported similar behavior for transitions at ∼3316 meV which were assigned to recombination at basal plane stacking faults, and had a lifetime of ∼ 500 ps. Fallert et al. [44] also observed a monoexponential decay of the transition at 3.31 eV for their ZnO nanocrystals being around three to five times longer than the decay time for the dominant shallow bound-excitons in their different samples. It should be noted that they assigned this transition to surface defect states.

The longer lifetime of the (e,A^0) transition compared to the I_9 transition in this sample can be explained by the decreased overlap of the wave functions of electrons and bound holes in a free-to-bound transition. The decay behavior of the 3308.8 meV further excludes the possibility that it is due to a $1-LO$ phonon replica. Taken together the previous data strongly support the identification of the 3308.8 meV lines as an e-A^0 transition.

4.3.4 Discussion

The preceding results are consistent with the formation of two distinct acceptor species in the presence of carbon dopant, or carbon/hydrogen co-dopant. Table 4.4 shows a summary of the transitions with their corresponding binding energies in the samples studied in this work. Considering the case of doping with CCl_4 only, and given the fact that the DAP band at 3237 meV occurs at the same position as the DAP reported previously in nitrogen doped ZnO samples [16, 31, 43], it is likely that nitrogen related defects are responsible. Lautenschlaeger et al. observed a DAP band very similar to our results, despite the use of carbon free precursors [16]. This suggests that carbon is not responsible for the DAP band

in our carbon doped samples.

It is likely that the carbon source facilitates the decomposition of nitrogen in the gas phase since a N2O precursor is used during the growth. The question of why we do not see an (e-A^0) transition corresponding to this DAP may be explained by the obviously higher concentration of non-radiative traps in the CCl_4-only samples, based on the very weak PL intensity (Fig. 4.9). Such a high density of traps would greatly reduce the free electron concentration available for (e-A^0) recombination.

Turning to the case of the carbon/hydrogen co-doped samples, the situation is quite complex. Hydrogen clearly suppresses the formation of the DAP emission, which could be due to the suppression of the NO formation mechanism which we postulated earlier, however the details are yet to be determined. It is clear that the co-doping of carbon and hydrogen leads to strong excitonic emission from the Z-lines, which have been identified as D^0X emission associated with possible carbon-related donors as discussed earlier in this chapter. Whether carbon can also incorporate as a relatively shallow acceptor complex consistent with the observed 3309 meV (e-A^0) transition remains an open question.

The presence of a strong (e,A^0) transition in the carbon/hydrogen co-doped samples indicates a high concentration of free electrons in these samples. This indicates that the donor defects responsible for the D^0X transitions are fully saturated, resulting in a net buildup of free electrons, but not free holes. This could arise either from strong compensation or perhaps is evidence of net p-doping.
This would also explain the absence of any DAP band corresponding to this acceptor in these samples. The other possibility of a free-hole to bound-donor (h-D^0) transition can be ruled out since simple considerations show that it should occur at a much higher energy, close to the bound-exciton region for the known shallow donors in ZnO. Further work is required to investigate the transport properties of these NWs.

4.4 Study of Sn-doping in ZnO

Very little is known about the behavior of Sn in ZnO. It is a group-IV impurity and it acts like other heavier atoms with similar atomic mass to occupy Zn sites (Sn_{Zn}) in ZnO [14, 71, 97]. Cullen et al. [64] have recently shown that radioactive ^{117}Ag implanted ZnO single crystal resulted in the observation of the I_{10} PL line at 3353 meV. Based on the radioactive decay of In to Sn, it was conclusively confirmed that the center in I_{10} contains Sn on a

Zn site. Meyer et al. also observed the I_{10} emission line in the PL spectrum of Li- and Na-doped ZnO single crystals [30]. Since Li is postulated to give rise to an acceptor state, one model for I_{10} could be the formation of a Sn-Li nearest neighbor double donor-acceptor pair, which would act as a single donor. A recent report [98] on Li diffusion in ZnO has shown the blue band in the PL spectra and this will be an evidence of the role of Li in these samples. However, the nature of impurity associated with Sn-related transition in photoluminescence is not clear yet.

In this section, we have studied the effect of Sn-doping on the photoluminescence of ZnO single crystals. The samples under study were grown at Oak Ridge National Laboratory by the chemical vapor transport (CVT) method as explained in chapter 3. Part of this work was published in Journal of Luminescence 176 (2016) 4748.

4.4.1 Effect of Sn-doping on the excitonic region of the PL spectrum

Fig. 4.15 shows typical high-resolution PL spectra of the undoped (A) and Sn-doped ZnO single crystals (B-E), in the bound-excitonic region, recorded at 4.2 K. The PL spectrum of the undoped sample (A) shows several emission lines in this region. Among them are previously identified transitions such as I_9 (In), I_8 (Ga), I_7 (unknown origin), I_6 (Al) and their corresponding D^+X transitions along with I_{11} (one of the Y-lines) and free excitons (FX). These transitions have linewidths as low as 66 μeV (I_{10}), 170 μeV (I_9) and 260 μeV (I_8) revealing the low concentrations ($\leq 10^{16}$ cm^{-3}) of residual impurities in these crystals.

Another transition with relatively weak PL intensity at 3353.2 meV was observed in the PL spectrum of this unintentionally-doped crystal, which is very close to the previously assigned I_{10} line position at 3353.1 meV [23]. This transition shows an increase in PL intensity relative to the residual I_9 transition as a function of increasing Sn-doping, suggesting that it may be associated with a defect containing Sn. However, the actual Sn concentration is not known and appears to be quite low based on the sharpness of the observed PL lines. The unintentionally-doped ZnO crystals (e.g. A in Fig. 4.15) are highly transparent, with no apparent color. The doped samples exhibit different ranges of blue color changing from sample to sample within the same growth run. Regarding the change in the color of the single crystals with different Sn-doping levels, the darker ones exhibit high relative intensity of I_{10} compared with the other residual donors. Also, the linewidth of the I_{10} line increases from 66 μeV for the undoped sample to 500 μeV for the darkest blue samples.

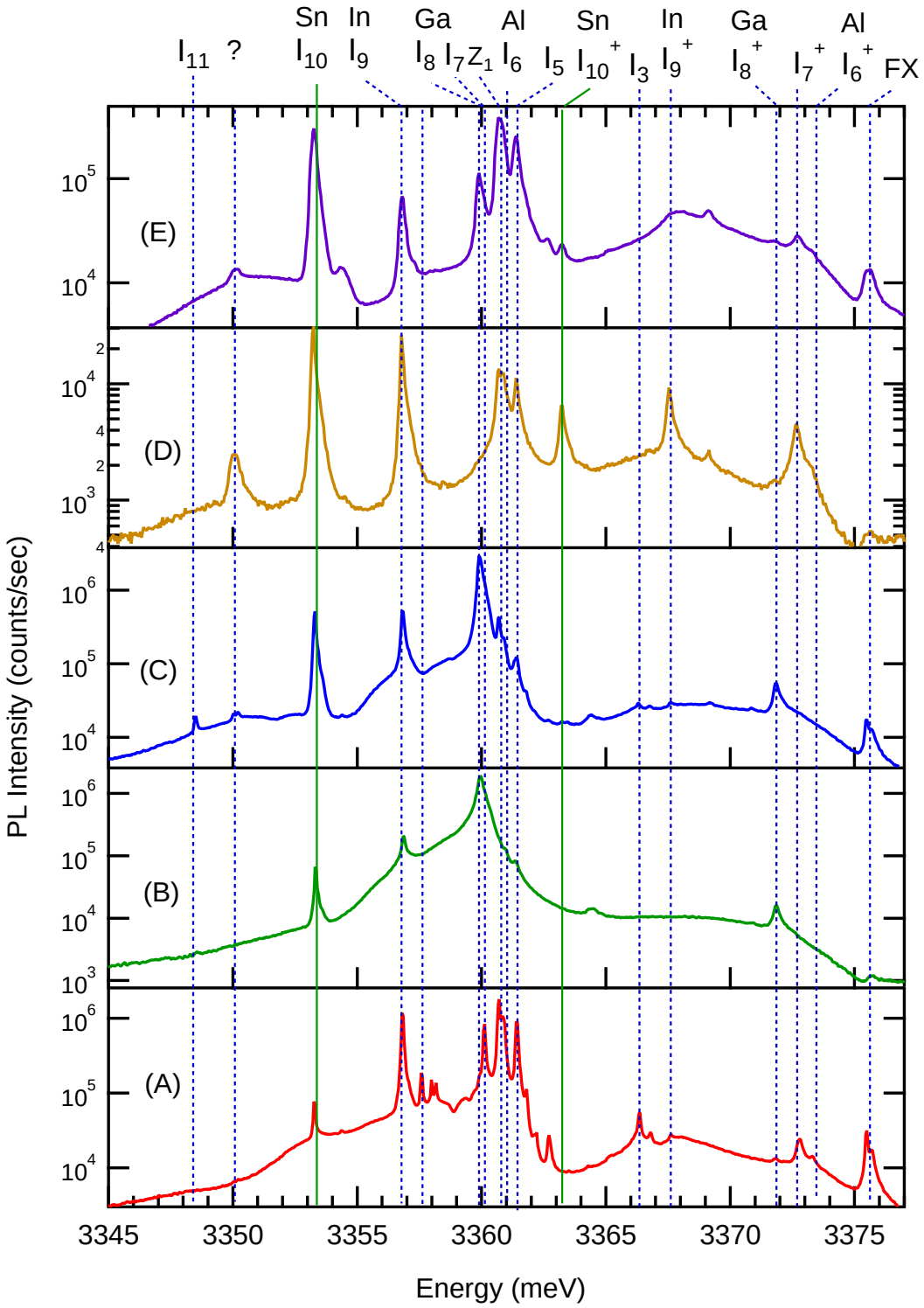

Figure 4.15: 4.2 K PL spectra of the undoped (A) and Sn doped (B-E) CVT grown ZnO single crystals.

The samples with significant I_{10} doping tend to have a feature at 3363.2 meV labeled I_{10}^{+} in Fig. 4.15, which was previously attributed to the $D^{+}X$ transition of I_{10} [30] however in that work the chemical origin of I_{10} was not yet known.

4.4.1.1 Thermalization behavior of the I_{10} transition

The temperature-dependence of the I_{10} transition should cast more light on the nature of this transition. Fig. 4.16-right shows the I_9 and I_{10} transitions at the range of temperature between 4 to 45 K. I_{10} line follows thermalization behavior similar to I_9 and its intensity falls steadily with increasing temperature. This is characteristic of the ground state of a bound-exciton transition.

Fig. 4.16-left shows the integrated line intensity of the I_9 and I_{10} transitions as a

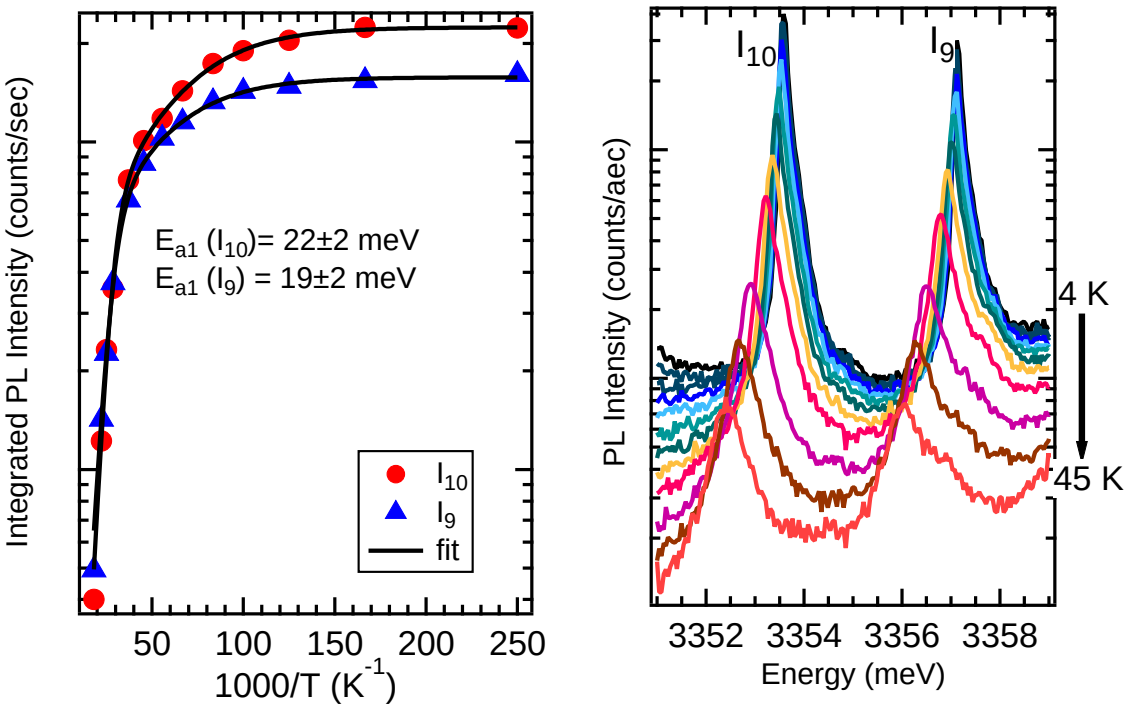

Figure 4.16: (right) PL spectra of the Sn-doped sample at different temperatures from 4.2 K to 45 K and (left) Temperature-dependent integrated PL intensity of I_9 and I_{10} lines.

function of temperature. The integrated PL intensity is fitted using Eq. 1.7 and the thermal activation energies are 19±2 meV and 22±2 meV for I_9 and I_{10}, respectively. These values are close to the respective spectroscopic binding energies of the I_9 and I_{10} transitions of 18.8 and 22.4 meV. This confirms that the I_{10}-line is associated with shallow impurity centers.

Fig. 4.17 shows the spectral shift of the I_8, I_9, I_{10} and Y lines as a function of temperature in the range of 4.2-45 K. The solid lines are least-square fits to the experimental data. The

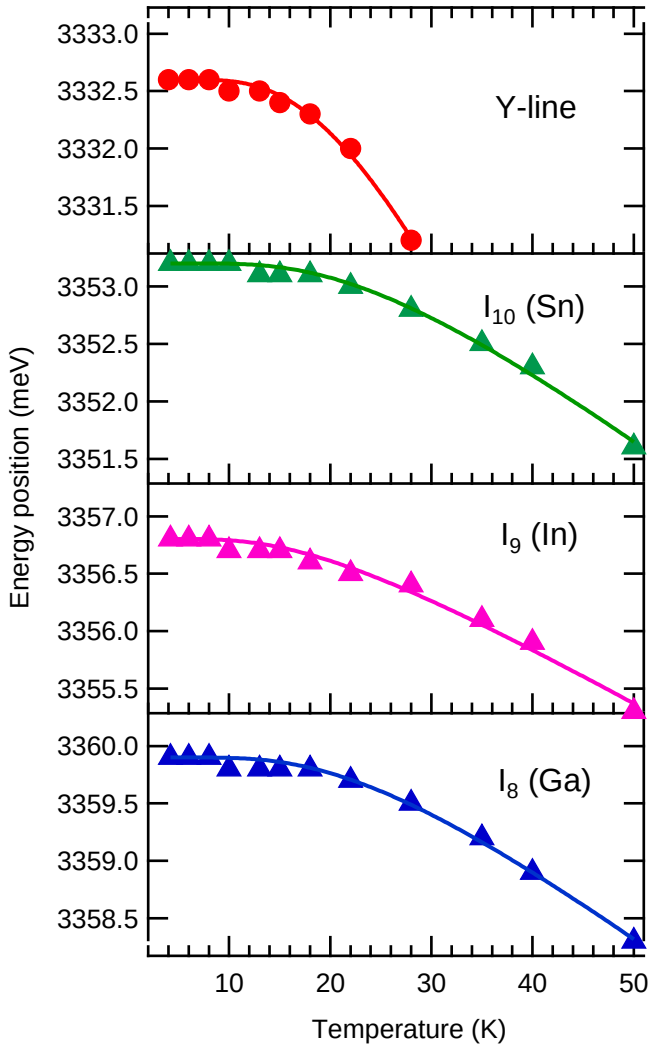

Figure 4.17: Temperature-dependent energy positions of the I_8, I_9, I_{10} and Y lines. Solid lines are fits to the data points using Eq.4.5.

fitting equation (Eq. 4.5) is obtained using a model by Viña et al. [99] based on a Bose-Einstein model which gives more reliable description in the low temperature range. The fitting parameters are listed in Table 4.5 for each transition.

$$E(T) = E_0 - \frac{\alpha}{\exp(\frac{\Theta}{T}) - 1} \tag{4.5}$$

Table 4.5: Summary of the fitting parameters used in Eq. 4.5.

Transition	α (eV/K)	Θ (K)
I_8	5.4 ± 0.9	74 ± 5
I_9	3.0 ± 0.6	56 ± 6
I_{10}	5.6 ± 0.8	76 ± 5
Y-line	17 ± 3	72 ± 5

where E_0 is the emission energy at $T = 0$ K, α is a parameter associated with electronâĂŞphonon coupling, and Θ is the effective phonon temperature. The solid lines in the figure represent the least squares fits to the data points. It is evident from the Fig. 4.17 that shallow bound-excitons exhibit different energy shift as a function of temperature compared to the deeply bound-excitons (Y-line) in the temperature range from 4.2 to 45 K. In the case of shallow D^0X transitions a decrease in the localization energy is reported which is explained by the screening of the impurity potential caused by the increasing free carrier concentration with increasing temperature [38]. In contrast to Y-line which has a smaller thermalization behavior compared to other shallow impurities, I_{10} transition is behaving like other shallow bound-excitonic transitions. This confirms that the impurity responsible for the I_{10} line is a shallow donor defect with a central cell potential similar to the group-III donors.

4.4.2 Two-electron-satellites and Haynes rule

Fig. 4.18 shows the D^0X and TES energy region for one of the Sn-doped samples. In the TES region, there are In (2s) and (2p) transitions at 3312.1 and 3307.5 meV, respectively along with two other transitions at 3301.1 and 3294.7 meV which are assigned to 2s and 2p levels of Sn donors. These are close to the previously reported 2p transition of the I_{10} line [23]. Knowing the position of the 2p line we can estimate the donor binding energy of 71.1 meV for I_{10} which is close to the value of 72.6 meV obtained earlier [23].

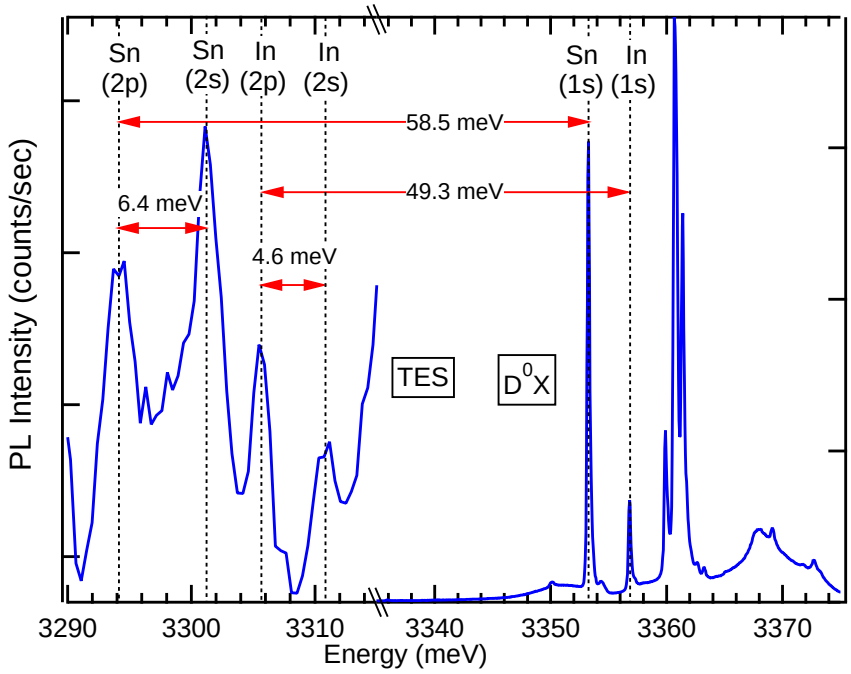

Figure 4.18: D^0X and TES region in the PL spectra of Sn-doped ZnO samples.

In order to obtain more information about the origin of Sn impurity in ZnO and compare it with other impurities in ZnO, their corresponding localization energy vs. donor binding energy (Haynes rule plot) is shown in Fig. 4.19. Ge [65] and Y-line are also included in this graph. 2s-2p splittings for these donors are also shown in this figure which indicates a similar systematic increase in central cell correction for the 2s donor state. It is clear that the Sn-related donor conforms very well to these trends. Note that In and Sn have the same core electronic structure.

While I_{10} is very similar to the known shallow single donors from group-III, it is in strong contrast to Ge, another previously studied group-IV impurity, which has a donor-bound exciton emission at 3324 meV [65]. Ge exhibits a similar final state donor binding energy but a much deeper exciton localization energy, as evident from Fig. 4.19-(a). Similar behavior is observed for the Y line defect at 3332.6 meV, suggesting a similar possible origin. A detailed microscopic model for these transitions is not yet available.

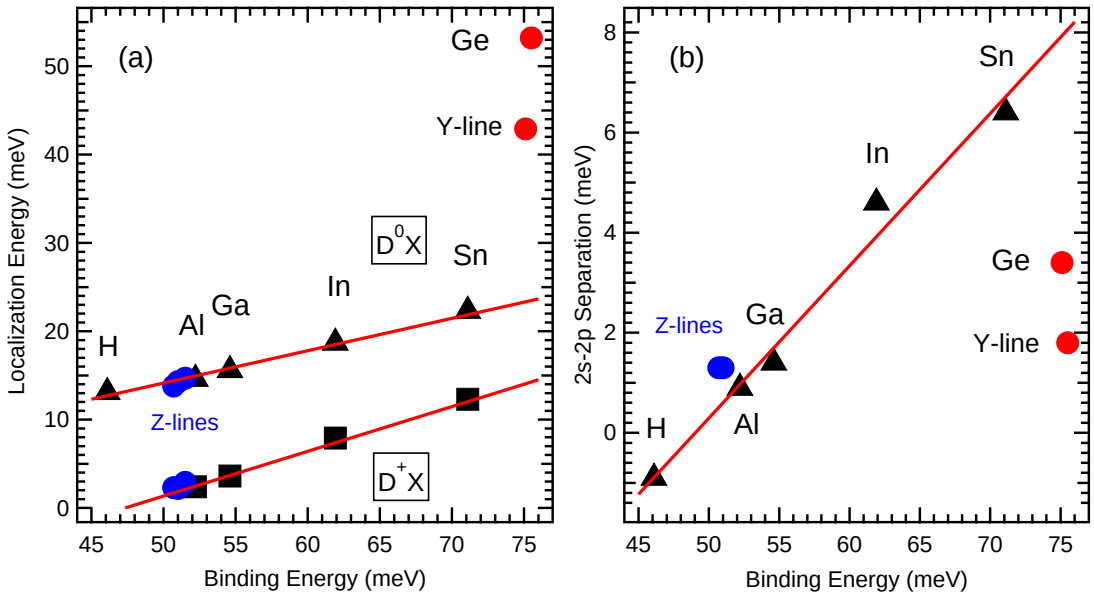

Figure 4.19: Dependence of the (a) D^0X and D^+X localization energies and (b) TES energy separation ($E_{2p} - E_{1s}$) on the donor binding energies. The values for Ge are taken from Ref. [65].

4.4.3 Discussion

The I_{10} transition was previously observed in Na- and Li-doped ZnO crystals while its origin was not identified [23]. PL measurements on ZnO crystals implanted with the radioactive impurity ^{117}Ag by Cullen et al. resulted in the appearance of the I_{10}-line which was absent in the primary sample [64]. Radioactive ^{117}Ag decays into radioactive ^{117}In, and then to stable ^{117}Sn which resulted in the appearance of the I_{10} line in the PL spectrum. Based on the observation of its corresponding TES lines at 3294.7 and 3301.1 meV, it is verified to be a D^0X transition with a binding energy of 71.1 meV.

Sn is a group-IV impurity and since it occupies the Zn site, it should be a double donor with two extra electrons per Sn atom. We can rule out an isolated Sn_{Zn} double donor since it is not expected to have 2s/2p excited final states because of the expected pairing of the electron spins. It is likely that Sn is partially compensated by acceptors and therefore acts as a single donor. Ge is also a group-IV element and has been studied as an impurity in ZnO [65, 71]. It was shown that Ge acts in a similar way to the Y-line in ZnO regarding its thermalization behavior and the fact that neither follow Haynes rule. They deeply bind excitons in ZnO and were considered to be related to structural defects.

In contrast Sn acts as a shallow donor. This is supported by its thermalization behavior since its thermal activation energy is on the order of its spectroscopic energy. In addition, it follows the Haynes rule like other shallow impurities. Previously, Wagner et al. [38] had shown that different thermalization behavior of Y-line with lower thermal activation energy was due to the fact that only one particle (hole) was dissociated thermally. In contrast to that, I_{10}-line had thermal activation energies in order of its localization energy which means exciton was bound to this defect center as a whole quasiparticle. It is also worth mentioning that, unlike the Ge and Y-lines, excitons can bind to ionized Sn centers and form I_{10}^{+} at 3363.2 meV.

According to the previous reports on Li- and Na-doped ZnO single crystals and the appearance of the I_{10} transition in their PL spectra [23], we speculate that the I_{10} center contains Li or Na. One model for I_{10} could be the formation of a Sn-Li nearest neighbor double donor-acceptor pair, which would act as a single donor. Li diffusion of Sn-doped ZnO single crystals could cast more light to the nature of this defect.

4.5 Conclusion

In this chapter the effect of intentional carbon and Sn-doping on the PL spectra of ZnO was studied. Neutral and ionized D^0X features related to group-IV dopants, C and Sn, in ZnO were observed. ZnO NWs co-doped with C and H were grown by MOVPE. High-resolution PL studies of these doped ZnO NWs at 4.2 K reveal four strong shallow donor-bound exciton transitions, which we named as Z-lines and which dominate the excitonic PL intensity at high dopant concentrations.

The presence of hydrogen as a co-dopant greatly increases the PL intensity, but does not result in excitonic hydrogen related PL emission. The dependence of exciton localization energy on donor binding energy follows the same trends as the group-III donors (I_6, I_8, and I_9) but what is not clear so far is the reason that carbon-doping leads to multiple lines in the PL spectra associated with the Z-line.

D^+X transitions of these Z-lines were also identified by correlation of PL intensity with the corresponding D^0X transitions. PL studies on post annealed samples reveal that the Z-lines are stable even after heating at 900 °C, which argues against the possibility of H being one of the impurities in the complex. The appearance of DAP and (e-A^0) emission at 3308.8 and 3236.7 meV is a clear evidence of distinct acceptors.

Two distinct acceptors with binding energies of 133±5 and 181±5 meV are confirmed by varying the excitation power and temperature, and by time resolved measurements. The 3236.7 meV peak is only observed in the presence of CCl_4 and is identified as a DAP transition corresponding to an acceptor binding energy of 181±5 meV. This is very close to previous reports of intentionally nitrogen-doped ZnO, and suggests that the CCl_4 precursor leads to the decomposition of N_2O to more reactive forms which incorporate in the NWs.

The 3308.8 meV emission is strongest in ZnO nanowires co-doped with CCl_4 and H_2 and is assigned to a previously reported (e,A^0) transition. The absence of DAP emission in the carbon-hydrogen co-doped samples, along with a strong (e,A^0) transition suggests a possible p-type behavior in these samples, or at least a high degree of compensation.

The optical properties of ZnO single crystals doped with Sn impurities were investigated. We found enhanced intensity of the I_{10} transition in intentionally Sn-doped samples. It is noteworthy that the variations in Sn-doping observed by PL are not attributed to changes in the SnO_2 precursor concentration, but rather to variations in the incorporation of Sn in different parts of the growth chamber due to variations in the temperature and other local growth conditions.

The temperature and energy level dependence of the Sn-related D^0X transitions show strong similarities with other shallow donors but they are in strong contrast to the behavior of Ge-related D^0X complexes and the defect related Y-line luminescence centers in ZnO. Two-electron-satellites and donor-bound exciton transitions were observed in agreement with previous studies where the origin of the I_{10} peak was unknown. Our results add support to a previous defect model for I_{10} consisting of substitutional Sn_{Zn} complexed with a single shallow acceptor impurity for example Li or Na [23, 30].

Chapter 5

Study of Sb-Doped ZnO Nanowires

5.1 Introduction

The study of group-V elements of the periodic table like N, P, As and Sb in ZnO is important because of the possibility of realizing p-type conduction. In theory, substitution of oxygen by these elements could lead to p-type ZnO. Most work has focused on nitrogen because of its close match in atomic radius to oxygen, however, it is now known that substitutional nitrogen behaves as a very deep acceptor [100]. As a result a great deal of effort has focused on heavier group-V elements like P, As, and Sb. However, the ionic radii of these elements are much larger than that of oxygen and it is believed to be very difficult to dope them on O sites. Wahl et al. [14] have shown using electron emission channeling experiments that Sb prefers to occupy the Zn site rather than O site. In order to explain apparent p-type conduction in Sb-doped ZnO, first principle calculations were performed that indicate that Sb_{Zn} can form a complex with two zinc vacancies (V_{Zn}) forming an acceptor complex ($Sb_{Zn} - 2V_{Zn}$) [101].

It has also been shown by Liu et al. [102] that Sb can behave as a donor in ZnO and lead to n-type conductivity. As part of this thesis, carefully controlled Sb doping of ZnO NWs was performed and a new feature was conclusively identified as due to shallow Sb donors based on the observation of a new D^0X transition in Sb-doped NWs.

This chapter will be concerned with the identification of this Sb-related transition by means of temperature and dopant concentration dependent PL measurements, along with magneto-PL to investigate the defect type of this transition. Part of this work is published in *Appl.Phys.Lett.* 102, 132105 (2013).

5.2 Morphology of the Sb-doped nanowires

Fig. 5.1 shows edge view SEM images taken from samples grown under identical growth conditions (explained in Chapter 2) with different concentrations of Sb doping in the source gas ranging from 3.8 to 76.4 nmol/min. The undoped sample has relatively uniform NWs with almost no tapering. The average length and diameter are in the range 1-2 μm and 160-200 nm, respectively. Increasing the TMSb flow rate induced a reduction in the length of the wires and increased the lateral growth.

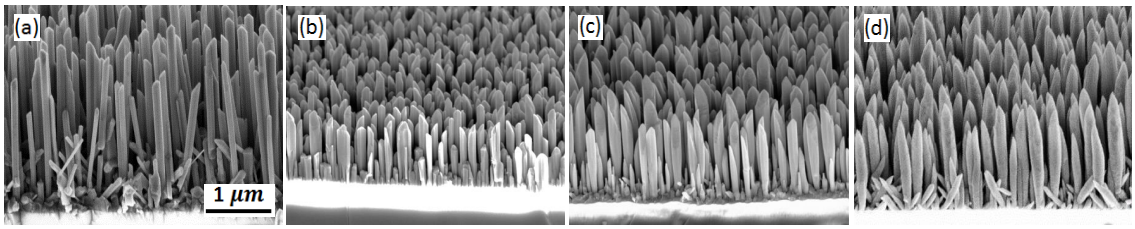

Figure 5.1: Effect of Sb doping on the morphology of ZnO NWs (a) undoped and (b) 19.1 (c) 38.2 and (d) 76.4 nmol/min Sb doped.

High-resolution X-ray diffraction measurements confirm that the NWs are highly oriented along the c-axis even at the highest doping level. No Sb related secondary phases were observed in any of these samples by XRD.

5.3 Optical Characterization of the Sb-doped nanowires

5.3.1 Effect of Sb doping on the excitonic region in the PL spectrum

Fig. 5.2 shows the PL spectra of the undoped and Sb doped NWs at $T = 4.2$ K. The PL spectrum of the undoped NWs is shown here for reference. Similar to the PL spectra of the undoped samples in the previous chapters, strong I_8 and I_9 transitions are seen at their conventional spectroscopic positions with narrow linewidths as low as 0.20 meV. The other lines in the spectra are all identified according to the discussions in the previous chapters. As we add a very small amount of Sb (3.4 nmol/min) we observe a new transition at 3364.3 meV along with other transitions present in the undoped spectra. This transition which is absent in the undoped ZnO NWs is observed for the first time in ZnO doped with Sb.

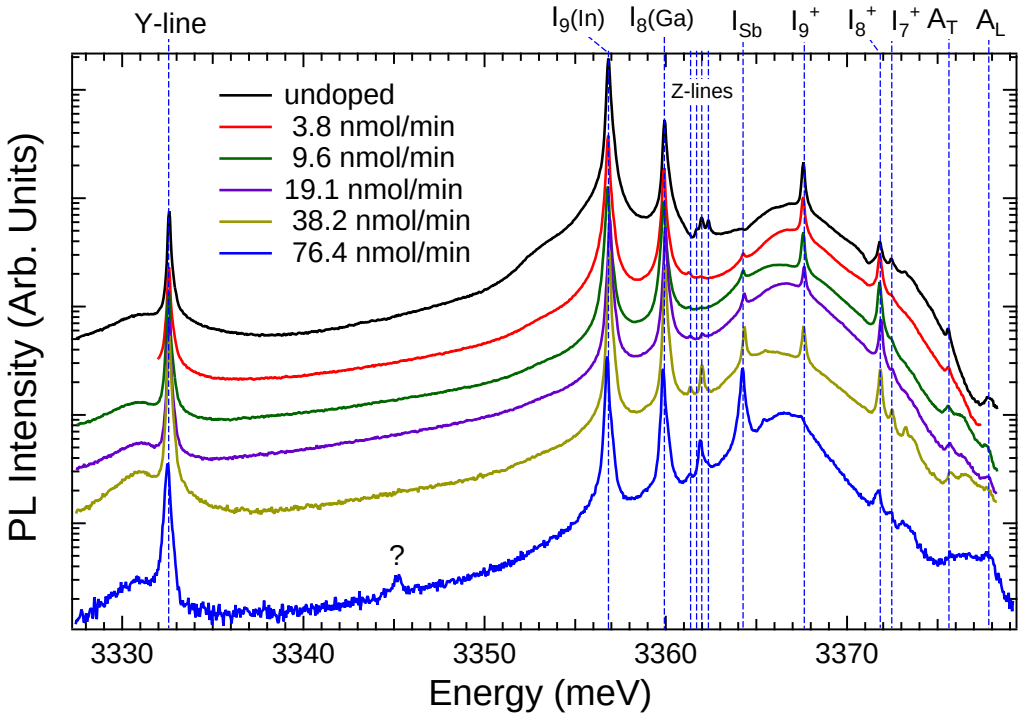

Figure 5.2: Effect of Sb doping on the PL spectra of the ZnO NWs at $T = 4.2$ K. The PL spectra are shifted in the y-axis for clarity.

Fig. 5.2 shows a systematic correlation between the intensity of this new transition and the Sb flow rate. At the highest doping level (76.4 nmol/min), the PL spectrum decreases in intensity while the intensity of the new transition becomes comparable to the residual I_8 and I_9 transitions. Nanowires with higher Sb flow rates showed no PL emission. The intensity of the 3364.3 meV transition scales with TMSb which suggests that this emission line is associated with excitons bound to Sb related impurities and we label it I_{Sb} for the rest of this work. It is worth mentioning that based on PL studies on radioactive ^{117}Ag implanted ZnO single crystals, Cullen et al. [64] also observed this Sb related emission at 3364.3 meV and published a report at the same time as our initial report.

Our room temperature Raman scattering measurements of the higher level of Sb doped NW samples show carbon related D and G modes at 1356 and 1598 cm^{-1}. As we discussed previously in the case of group-IV dopants the onset of the D and G modes correlates with the decrease of the overall PL emission.

PL of the 38.2 and 76.4 nmol/min Sb-doped ZnO NWs showed a slight increase in the intensity of one of the Z-line transitions (I_{Z4}, 3362.0 meV) compared with the undoped

NWs. As we showed in Chapter 4, the Z-lines are due to carbon impurities in ZnO. At higher Sb concentrations it is possible that carbon incorporation originates from the TMSb source.

Post annealing treatment of the 76.4 nmol TMSb doped ZnO NWs at 700 °C and 800

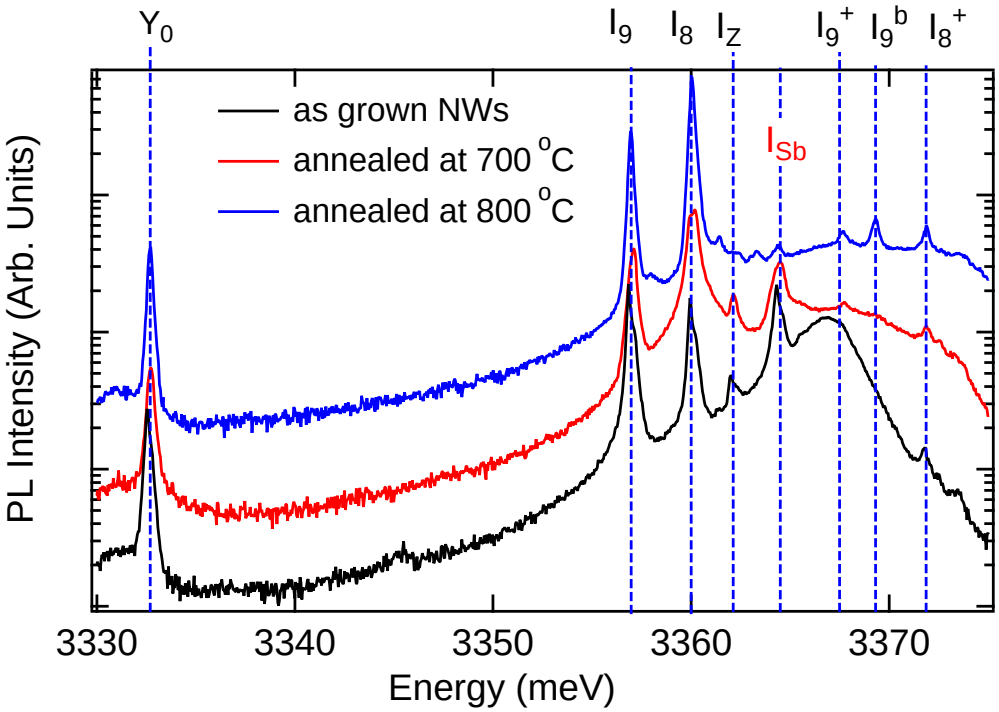

Figure 5.3: Effect of post annealing on the I_{Sb} transition in sample with 76.4 nmol/min Sb doping. The PL spectra are offset in y-axis for clarity.

°C in a 3 SLM flow of N_2O for 10 min resulted in different behavior of the I_{Sb} transition compared to the other transitions as shown in Fig. 5.3. The I_{Sb} transition decreased in intensity by 15% and 95% with annealing at 700 °C and 800 °C, respectively. However, the intensity of the I_8 and I_9 transitions increased with annealing relative to I_{Sb}. This behavior is very similar to the behavior of the hydrogen D^0X (I_4) transition observed in bulk ZnO single crystals [23] and indicates that the Sb related impurity causing the I_{Sb} transition is not thermally stable over 700 °C. We discuss this defect complex in more detail in Section 5.3.3.

To investigate the effect of H co-doping at higher Sb concentrations on the PL spectra, we have grown a series of Sb and H co-doped ZnO NWs with a fixed flow of 20 sccm Sb while varying H_2 flow from 2 sccm to 25 sccm. Fig. 5.4 shows 4.2 K PL spectra of the

undoped, 20 sccm Sb and Sb- and H- co-doped samples. H co-doping was found to result in a strong enhancement of PL in Sb-doped samples at higher concentrations. Note that the

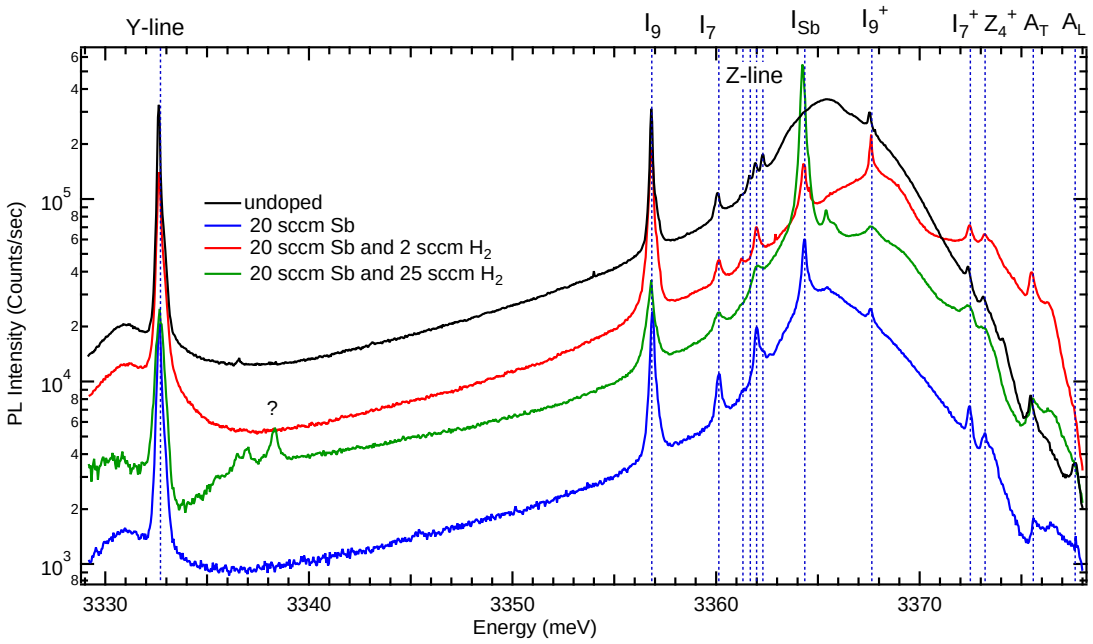

Figure 5.4: Effect of post annealing on the I_{Sb} transition in sample with 76.4 nmol/min Sb doping. The PL spectra are offset in y-axis for clarity.

sample with 20 sccm of TMSb and 25 sccm of H_2 resulted in I_{Sb} being the dominant PL peak in this sample, with peak intensity comparable to the undoped samples. This increase in PL intensity is similar to the behavior observed for carbon doping and suggests that a similar mechanism is at work.

5.3.1.1 Temperature-dependent PL

Temperature-dependent PL measurements were performed for the 76.4 nmol/min Sb doped ZnO NWs to understand the thermalization behavior of the I_{Sb} transition. Fig. 5.5 shows the PL spectra of the Sb-doped ZnO nanowires as a function of temperature. By increasing the temperature from 4.2 K to 60 K, the intensity of I_{Sb} falls steadily which is similar to the thermalization behavior of other neutral donor bound-exciton transitions I_8 and I_9. This is a characteristic of the ground state of a bound-exciton transition. If the I_{Sb} transition belonged to one of the excited states of one of the D^0X (Ga and In) transitions, the PL intensity should first increase with temperature and then fall rapidly with further increase

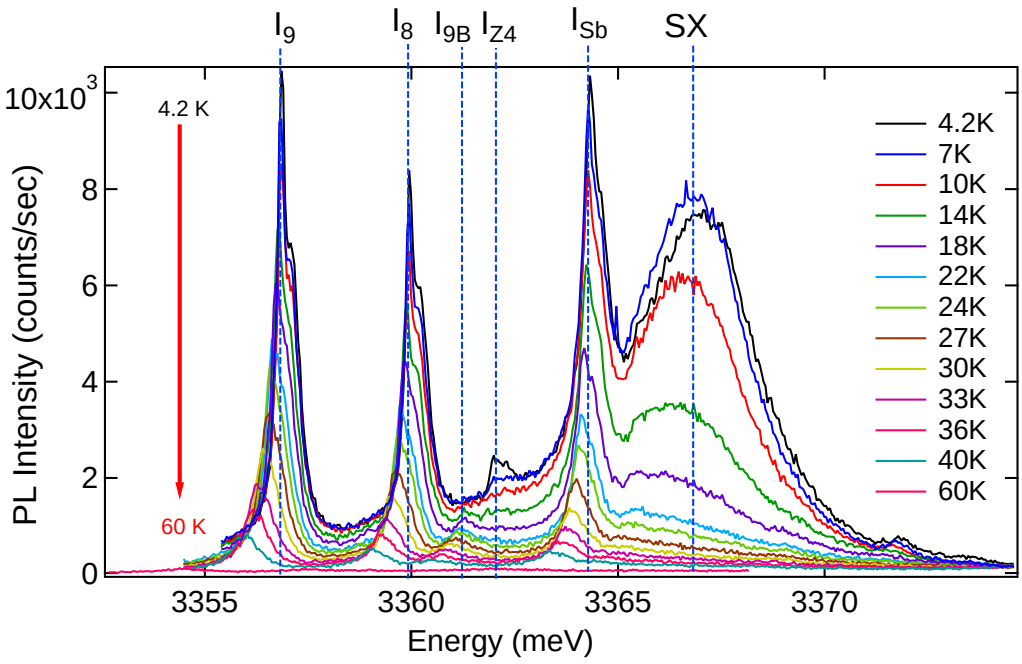

Figure 5.5: PL spectra of the 76.4 nmol/min Sb doped ZnO NWs as a function of temperature (from 4.2 K to 60 K).

Table 5.1: Thermal activation energies obtained from the temperature-dependent PL measurements.

BX	E_1 (meV)	E_2 (meV)	C_1	C_2	E_{loc} (meV)
I_8	2.7 ± 0.7	13.9 ± 1.7	3	746	15.6
I_9	3.1 ± 0.5	19.8 ± 1.9	2	1781	18.7
I_{Sb}	2.0 ± 0.4	14.7 ± 1.9	2	694	11.2

in temperature [60]. Therefore the thermalization data rules out the possibility that the observed I_{Sb} line is due to the I_8^B excited state transition of Ga which would occur at a similar energy. Such an excited state would have a low intensity at 4.2 K, however, in contrast with the observations shown in Fig. 5.5.

Fig. 5.6 shows the integrated line intensity of the I_8, I_9 and I_{Sb} transitions as a function of temperature. The integrated PL intensity is fitted using the simplified Boltzmann statistics model given in the chapter 1. Table 5.1 lists a summary of the fitting parameters. The activation energies of the I_9, I_8 and I_{Sb} are close to the accepted spectroscopic values as expected for D^0X transitions.

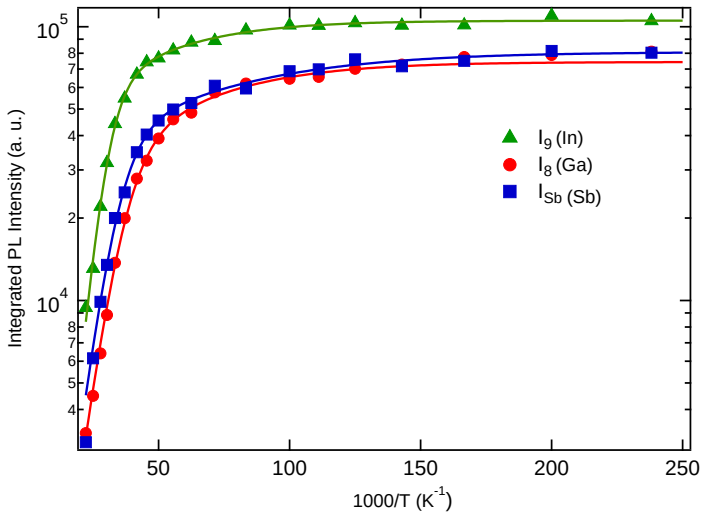

Figure 5.6: Temperature-dependence of integrated PL intensity of I_8(Ga), I_9(In) and I_{Sb} transitions. Solid lines represent fits using a simplified Boltzmann statistics model.

5.3.1.2 Two electron satellites and Haynes rule

As we discussed in Chapter 2, the D^0X transitions of the donors are often accompanied by their two electron satellites (TES). However, in the case of the Sb doped samples we could not observe any evidence of TES. In Fig. 5.7 the D^0X energy vs. $E_{2p} - E_{1s}$ has been plotted along with its linear fit for Al, Ga, and In donors in our ZnO NWs. Assuming that the Sb donor obeys Haynes rule, we can estimate the E_{2p}-E_{2s} energy by interpolating from Fig. 5.7 based on the measured D^0X energy for I_{Sb}. We have estimated the $E_{2p} - E_{1s}$ energy difference for the I_{Sb} transition as 31.6 meV which is shown as a blank data point in this figure. This value gives the estimated TES (2p) energy position of the Sb related donor at 3332.7 meV, which is very close to the Y_0 transition (3332.6 meV). Since there is a strong Y_0-line in the PL spectra of all Sb-doped samples, the TES transition of Sb related donors will be completely suppressed and hence it is not surprising that we could not observe any Sb related TES.

Recently, photoluminescence excitation measurements using a tunable UV source consisting of a LED lamp coupled to a grating spectrometer has been performed on our Sb doped sample by undergraduate student Katrina Stirling, and they confirmed the presence of the TES of Sb line at 3334.7 meV. The LED wavelength was fixed at the energy position of the Sb transition, I_{Sb}, exciting the sample while the PL signal was being collected by the PMT detector. The advantage of this measurement is that the Y-line is not excited, since

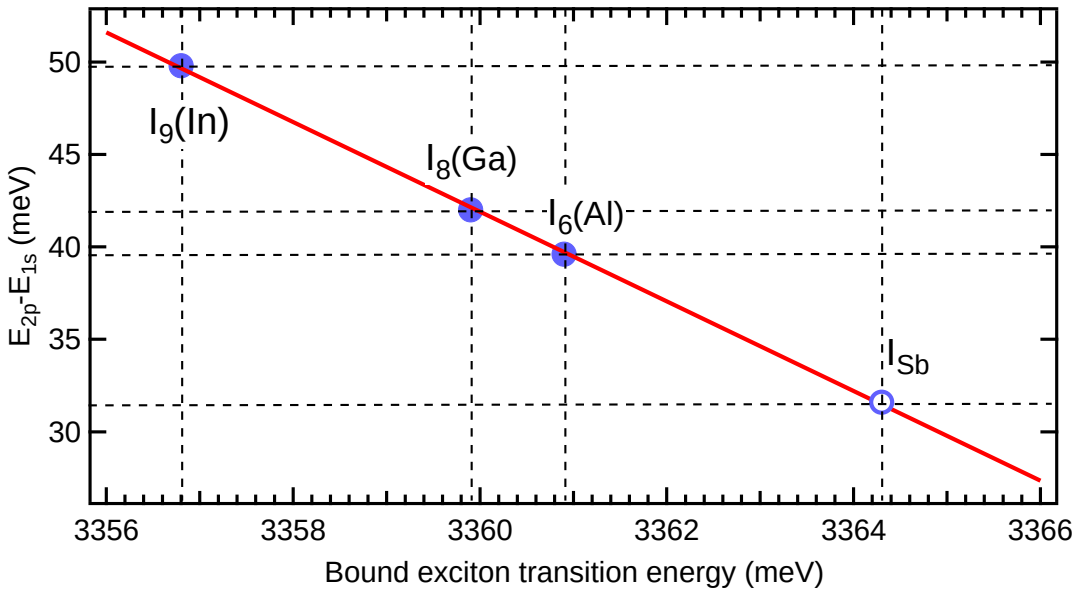

Figure 5.7: D^0X and TES energy separation ($E_{2p} - E_{1s}$) vs. D^0X energy position. The I_{Sb} data point in this figure is not based on a measured TES energy position but is extrapolated from the three known donors, I_6, I_8 and I_9.

the excitation is resonant. Fig. 5.8 shows the PL spectra in the TES/Y-line region with two different excitation sources. Using resonant excitation with the LED source, the Y-line is completely suppressed and the Sb TES is resolved at 3334.7 meV.

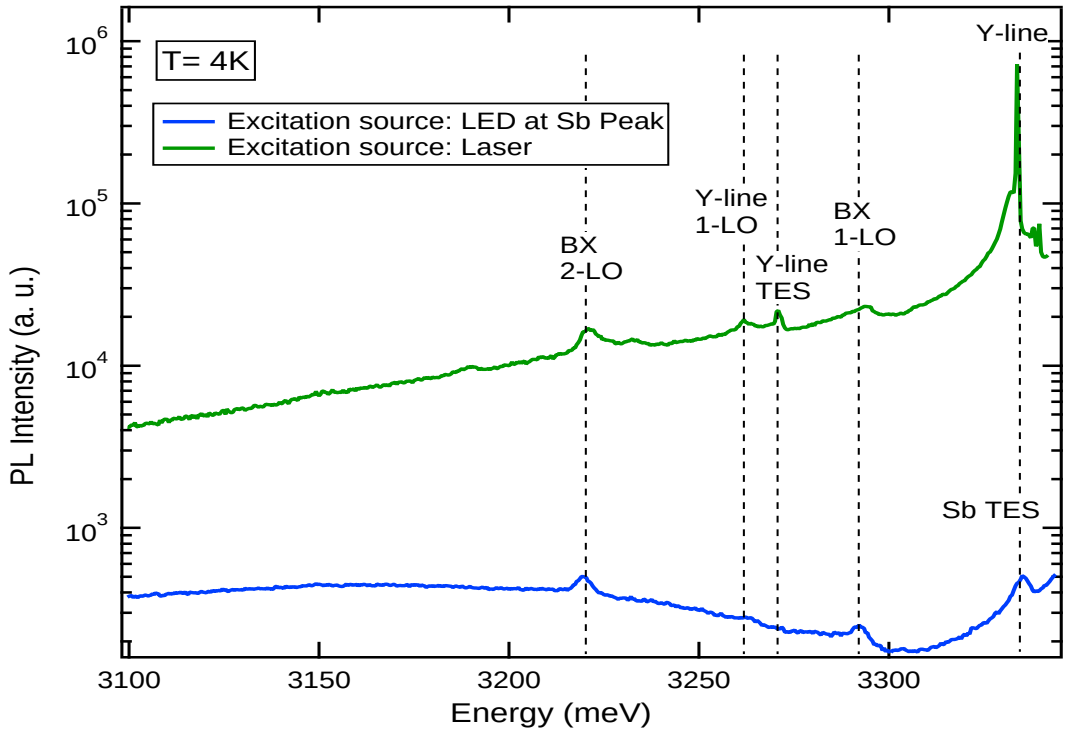

Figure 5.8: PL spectra of Sb doped ZnO NWs using two different excitation sources. Data was provided by our summer student, Katrina Stirling.

The donor binding energy can be estimated from the relation $E_D = (E_{1s} - E_{2p}) + 12.6$ meV [23]. Hence the estimated donor binding energy of the Sb related donor is 42.2 meV. The EMA donor binding energy in ZnO is calculated to be 50.15 meV [23]. This value is shown as the vertical green line in the Fig. 5.9. Therefore the binding energy of the Sb donor is significantly shallower than the EMA value, implying a significant negative central cell potential. This is the shallowest known donor in ZnO.

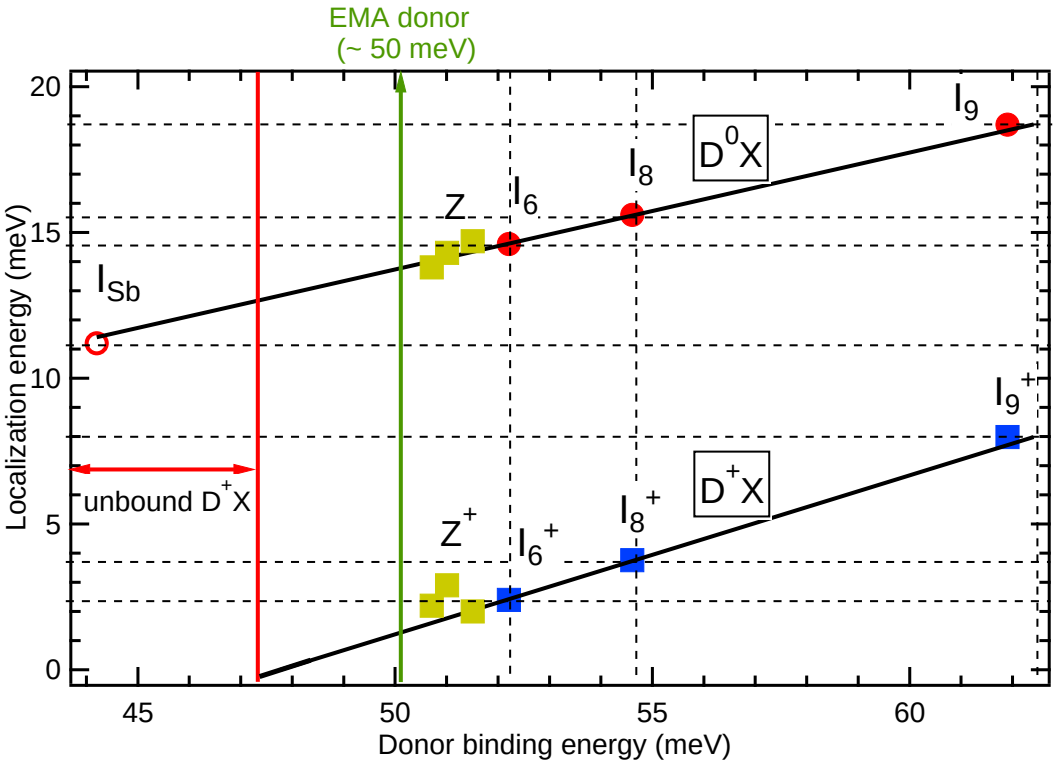

Figure 5.9: Relation between localization energy and donor binding energy for the three common group-III donors and Z-lines. Data are extrapolated to the estimated donor binding energy responsible for the I_{Sb} transition. For D^+X, the Sb complex should have no bound state in agreement with observation.

While our measurements so far are consistent with the observation of a D^0X peak, we have seen no evidence of a D^+X peak in these samples. The donor binding energies, E_D usually scale linearly with their respective localization energies (E_L) of both D^0X and D^+X transitions (Haynes rule). In Fig. 5.9 we have plotted the localization energy of D^0X and D^+X transitions vs. donor binding energy for the In, Ga and Al donors. Linear fits to the experimental data are also shown in this figure. The extrapolated linear fit of D^+X suggests that excitons will not be bound to ionized donors for donor binding energies <47.3 meV and therefore it is reasonable that no D^+X is observed for the Sb donor. Such behavior was observed previously for the hydrogen D^0X transition, I_4 [30] which also has a negative central cell correction, corresponding to a donor binding energy of 46.1 meV [23].

5.3.2 Zeeman spectroscopy measurements

Magneto PL measurement is a useful tool to distinguish the charge state of bound excitons. As explained in Chapter 1, D^0X and A^0X transitions show a linear splitting under an applied magnetic field perpendicular to the crystal c-axis while D^+X transitions exhibit a nonlinear splitting of transition lines [49, 50]. It is also possible to distinguish A^0X from D^0X by the thermalization of the Zeeman split luminescence lines [24, 30, 103, 104]. Previous magneto PL studies on ZnO has clearly shown that I_6^+, I_8^+ and I_9^+ are due to the recombination of excitons bound to ionized donors and I_6, I_8 and I_9 are due to the recombination of excitons bound to neutral donors [24, 77, 105].

In order to investigate further the origin of the I_{Sb} transition in ZnO NWs, we did magneto PL on our Sb-doped sample at the Technical University of Berlin. The sample geometries for this work are illustrated in Fig. 5.10.

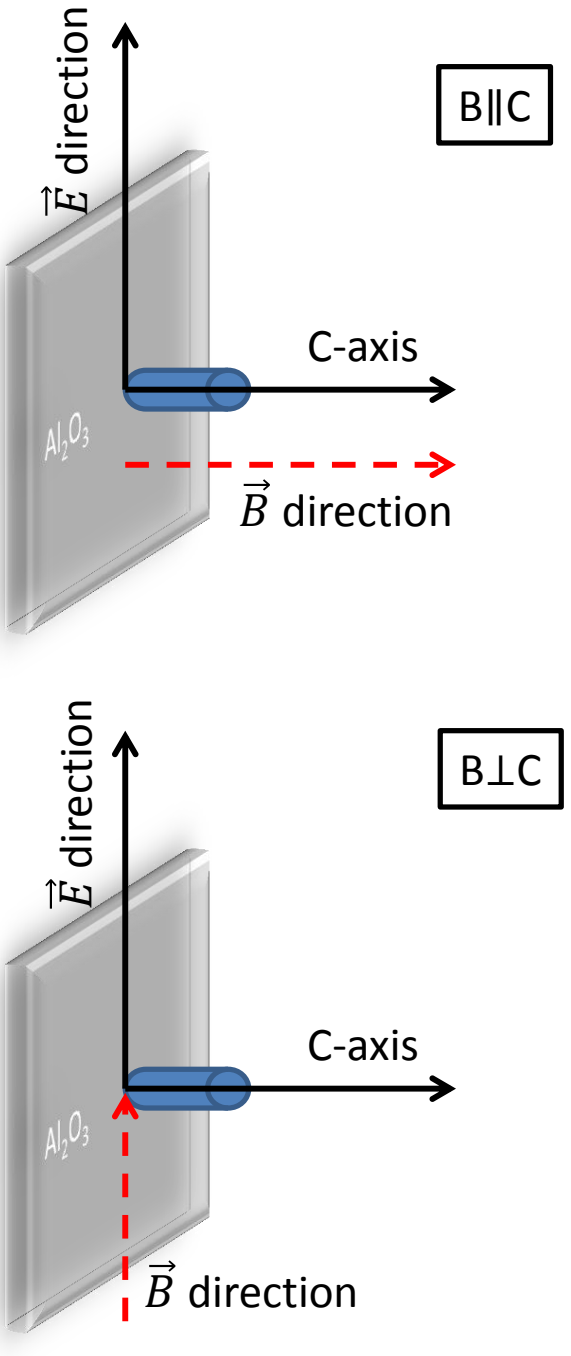

Figure 5.10: ZnO NWs geometry in an applied magnetic field indicating the magnetic field direction with respect to the c-axis and PL electric vector direction.

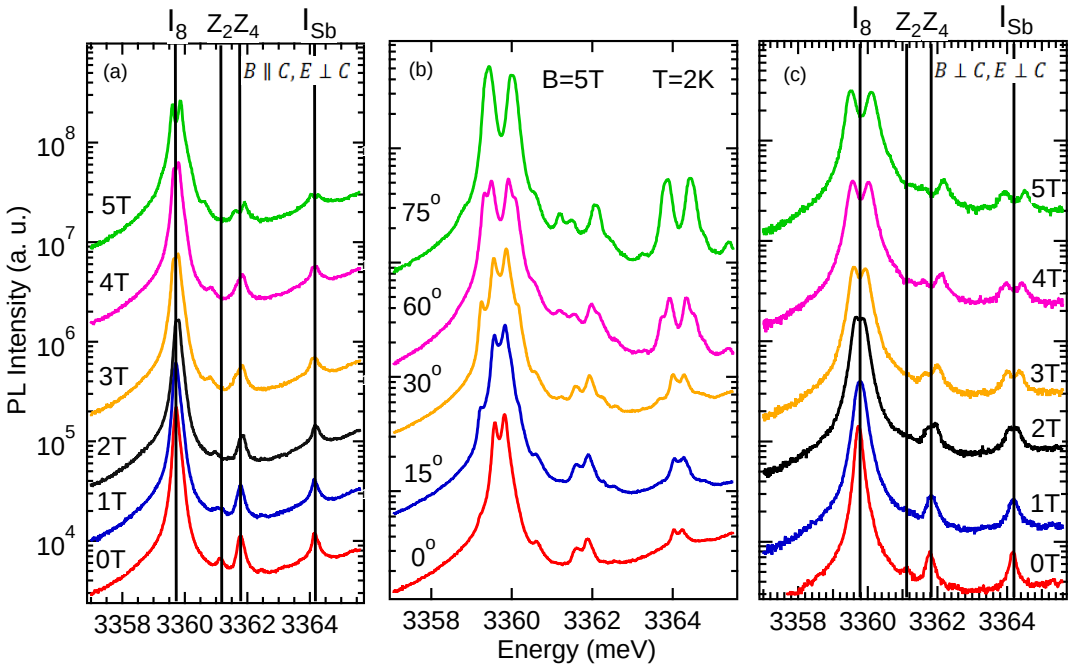

Figure 5.11: Zeeman splitting of neutral bound excitons I_8 and I_{Sb} in (a) Faraday ($B \parallel k$) configuration, (b) MPL for different angles θ between B direction and c-axis at $B = 5$ T and (c) Voigt ($B \perp k$) configuration. Vertical lines show the position of transitions at zero-field.

The PL spectra were recorded at $T = 2$ K in Faraday ($B \parallel k$) configuration (Fig. 5.11-a), Voigt ($B \perp k$) configuration (Fig. 5.11-c) and at different angles between B and c-axis of the sample (Fig. 5.11-b). In these measurements the maximum magnetic field B is 5 T. All the spectra are shifted vertically for clarity and are taken in the same spectral range. The angle dependent measurements started at $B \parallel k$ ($\theta = 0$) and ended at $\theta = 75^{o}$ with respect to the C-axis at a fixed magnetic field of 5 T. The observed Zeeman splitting in these measurements depends on the selected configuration and the type of defects (e.g. D^0X or D^+X). We have only shown the D^0X region in this figure which is limited to the I_8 and I_{Sb} transitions. In this section we only focus on the excitons bound to Ga and Sb donors.

The small Zeeman splittings of I_8 and I_{Sb} in the Faraday configuration are shown in Fig. 5.11-a. Two additional peaks appear when θ is nonzero. Fig. 5.11-c shows a clear linear splitting of the I_8 and I_{Sb} lines into two distinct components under magnetic field in the Voigt configuration. Both split components maintained equal intensity which indicates no thermalization behavior between them.

Fig. 5.12 shows the Zeeman splitting of the D^+X region of the spectrum in Faraday configuration (a), for different angles of θ between the magnetic field direction B and the

crystal c-axis (b), and in the Voigt configuration (c). Three transitions are observed in the zero field splitting which are assigned I_7^+ and I_8^+. Under an applied magnetic field, D^+X transitions split nonlinearly which differentiates them from D^0X transitions. It is interesting that in our ZnO NWs, we have observed this nonlinear splitting starting at zero-field and it is explained in the next section. This new split component at the lower energy side of the I_8^+ transition is named I_{8L}^+. Its intensity increases with magnetic field in the Voigt configuration. In the case of the I_7^+ transition, the corresponding split components overlap with I_8^+ which makes it difficult to resolve them.

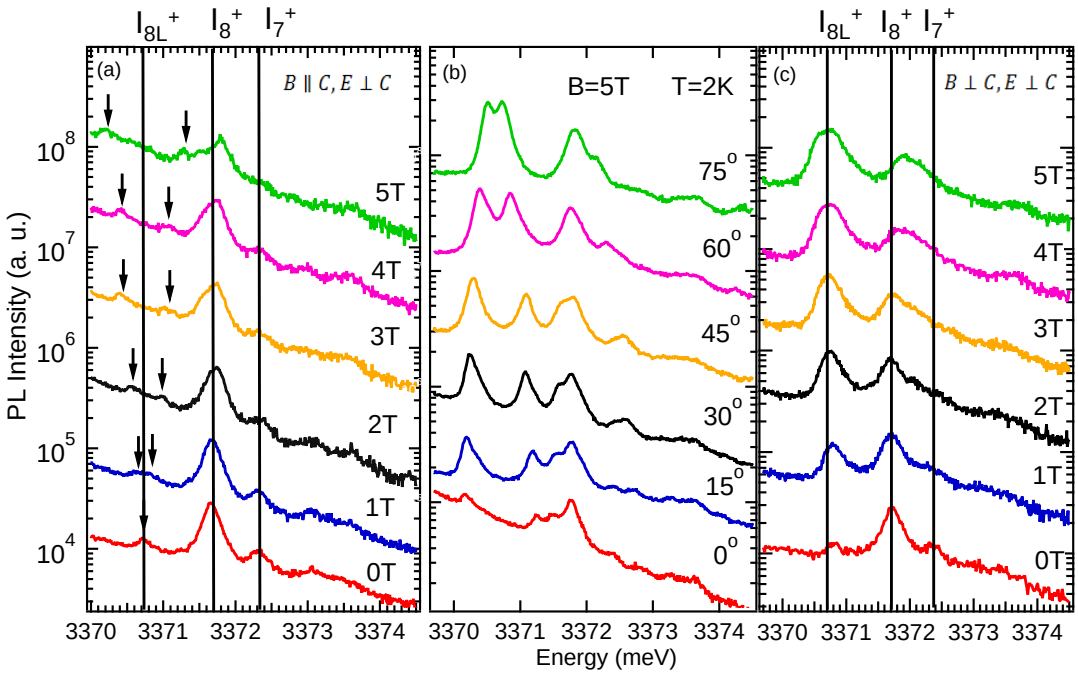

Figure 5.12: Zeeman splitting of D^+X transitions I_8^+ and I_7^+ in (a) Faraday ($B \parallel k$) configuration, (b) arbitrary angles between the magnetic field B and the c-axis and (c) Voigt ($B \perp k$) configuration. Vertical lines show the position of transitions at zero-field.

5.3.2.1 Analysis of the Zeeman data

The magneto-PL data presented in the previous section will be analyzed here using the Zeeman splitting theory presented in Chapter 1. Data points presented in Fig. 5.13 and Fig. 5.14 in this section are from Lorentzian fits of the corresponding transitions under a magnetic field in different configurations. In a D^0X transition the magnitude of the splitting under an applied magnetic field is determined by the g-factor of the electron in the final (D^0) state, and the hole in the initial (D^0X) state.

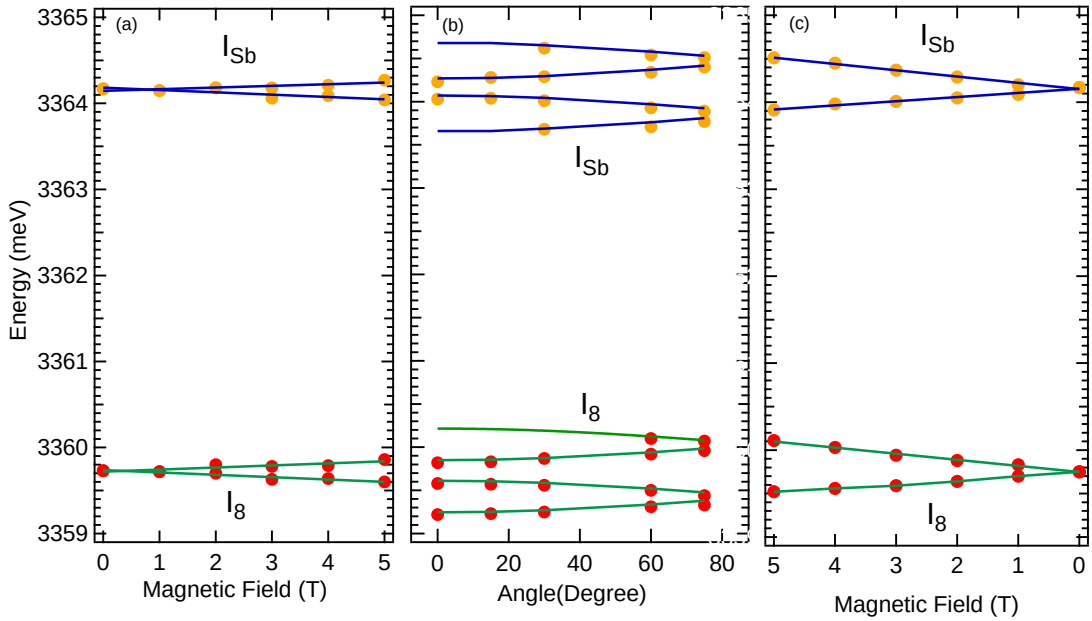

Figure 5.13: Zeeman splitting of D^0X transitions I_8 and I_{Sb} in (a) Faraday configuration, (b) arbitrary angles between the magnetic field B and the c-axis and (c) Voigt configuration. The solid lines are the fits to the data as discussed in the text.

In the Voigt configuration ($B \perp k$) the D^0X initial state splitting is due to the splitting of the unpaired particle (hole) and is small since g_h factor is highly anisotropic and vanishes when $B \perp k$. The final state consists of a positively charged ion and an electron. Thus the splitting observed in Fig. 5.11-c is almost completely due to the splitting of the ground state.

As it can be seen from Fig. 5.13 the I_{Sb} transition follows the same behavior as the I_8 line under an external magnetic field and undergoes a linear splitting, which confirms the neutral charge state for this D^0X transition. When the angle θ between the applied magnetic field and the crystal c-axis changes, additional Zeeman components which were forbidden at $\theta = 0$ appear. The four observed Zeeman line energies are given by:

$$E^{\pm} = E_0 \pm \frac{1}{2}(g_e + g_h)\mu_B B \qquad \text{(Outer Zeeman pair)} \tag{5.1}$$

$$E^{\pm} = E_0 \pm \frac{1}{2}(g_e - g_h)\mu_B B \qquad \text{(Inner Zeeman pair)} \tag{5.2}$$

From Fig. 5.13-b it can be seen that as the angle θ changes from 90^o to 0^o the splitting of the inner transitions decreases and the splitting of the outer Zeeman transitions increases.

Table 5.2: Electron and hole g-factors of D^0X transitions in this work and other references.

BX	g_e	$g_h^{\parallel}$	$g_h^{\perp}$	reference
I_8	1.96	-1.28	0.18	This work
I_8	1.92	-1.24	0.08	[24]
I_{Sb}	1.97	-1.29	0.21	This work
I_9	1.98	-1.36	0.1	[105]

This behaviour can be explained by the anisotropy of the hole g-factor which changes with angle θ. The experimental data have been fitted by Eq. 5.1 and 5.2 for the different angles between the magnetic field and c-axis and shown by the solid lines. The fitting has given the values for electron and hole g-factors in different transitions as listed in the Table 5.2. There is good agreement between our results and previously reported g-factors for I_8 [24, 77, 105].

Comparing the Zeeman splitting in the Faraday and Voigt configurations it can be seen that the splitting is smaller in the Faraday configuration. This is due to the negative hole g-factor ($g_h^{\parallel}$) and ($\left|g_h^{\parallel}\right| < g_e$). This indicates that the holes involved in the excitons bound to Ga donors and Sb are from the A-valence band (Γ_7) and not the B-valence band (Γ_9) [105]. It is also noteworthy that the Zeeman splitting of I_{Sb} is not consistent with a D^+X transition which would have a nonlinear splitting under an applied magnetic field perpendicular to the C-axis.

As we mentioned in section 1.5.1.1 earlier, D^0X transitions can be distinguished from A^0X transitions by the thermalization of the Zeeman split luminescence lines in external magnetic fields. For D^0X transition in the Voigt configuration ($B \perp k$) the $g_h^{\perp}$ is small and the splitting is caused by the g_e of the final state which does not thermalize since its occupation is strictly determined by the quantum mechanical transition strength. Thus, in this configuration, equal intensities of the Zeeman split transition lines of D^0X transition are expected, which are independent of the temperature. Therefore, by increasing the magnetic field at low temperature, a constant intensity ratio in the case of D^0X transition is expected. However, in the case of an A^0X transition the splitting of the excited state is given by the g_e in the initial state (Fig. 1.10). As a consequence, at low temperatures the intensity of the high-energy Zeeman split component should be smaller than the low energy component due to thermalization and is expected to increase with temperature.The ratio of the Zeeman

split lines is given by

$$\frac{I_{up}}{I_{down}} = \exp\left(-\frac{\Delta E}{k_B T}\right) \tag{5.3}$$

where ΔE is the energy splitting of the two component.

Our results (Fig. 5.11-(c)) show negligible thermalization of the Zeeman-split lines for the Voigt configuration. Based on the measured temperature of 2 K, the Boltzmann fraction of the upper state for an energy splitting of 0.6 meV at B =5 T should be 0.03 according to Eq. 5.3, which is clearly much lower than the observed ratio of approximately 1. This is additional confirmation that I_{Sb} is a D^0X transition and not an A^0X transition.

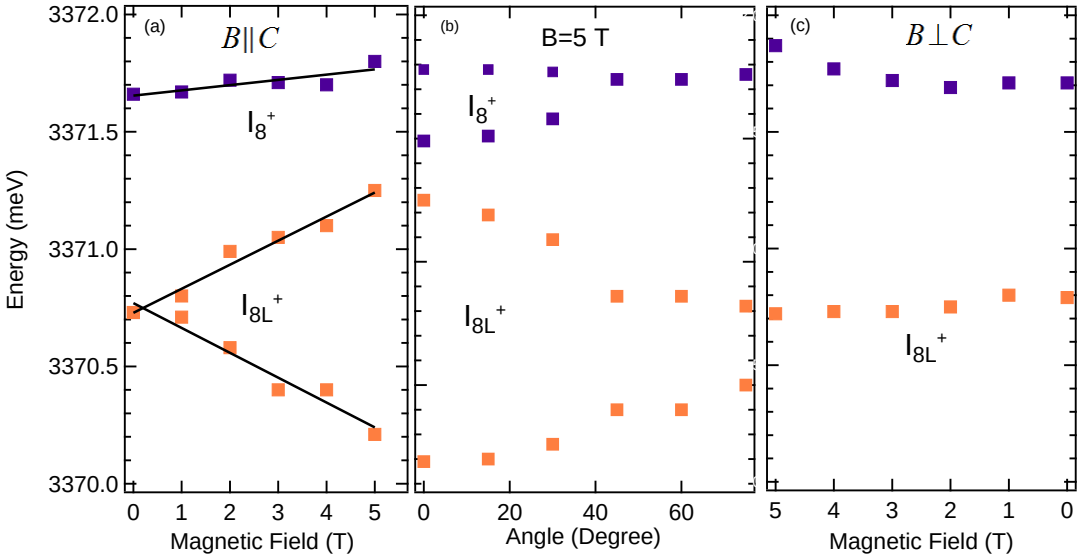

Figure 5.14: Zeeman splitting of neutral bound excitons I_8^+ in (a) Faraday configuration, (b) arbitrary angles between the magnetic field B and the c-axis and (c) Voigt configuration. The solid lines are just to guide the eyes.

Next I investigate the magnetic field dependence of known D^+X transitions I_8^+ and I_7^+ in order to compare them with that of the I_{Sb} line. In order to clearly identify the position of the transitions shown in Fig. 5.12, they are fitted by Lorentzian. The peak positions are plotted in Fig. 5.14 as a function of magnetic field (Fig. 5.14-a,c) and angle θ between the magnetic field and the crystal C-axis (Fig. 5.14-b). Here we only focused on the I_8^+ transition and not I_7^+ since its intensity was not enough to resolve it at higher magnetic fields.

At $B = 0$ a new transition is observed at 3370.79 meV which is at the lower energy side of the I_8^+ transition labeled I_{8L}^+. As shown in the diagram in Fig. 1.11, when $B = 0$,

this transition is only allowed for ($E \parallel C$). The reason that we observe it even for $E \perp C$ polarization can be explained by the fact that some of the wires in the sample are tilted in a way that satisfies this condition at zero magnetic field. This transition is clearly seen in the Voigt configuration and is attributed to the $\Gamma_{1,2}$ exciton states as discussed in chapter 1. The resulting components, I_8^+ and I_{8L}^+, remain nearly unsplit in $B \perp c$.

The value of zero-field splitting of these two exciton states is 0.92 meV which is in good agreement with previously reported values in ZnO [24, 34]. This splitting is not observed in the zero-field splitting of the D^0X since the spins of the paired particles (i.e. the two electrons) in the initial state are anti parallel. The energy positions of the I_8^+ components are not very clear due to overlap with the lower component of I_7^+ transition. This nonlinear splitting of the D^+X transition clearly differentiates them from D^0X transitions.

5.3.3 Discussion

Comparing Sb and other dopants so far we have studied in ZnO, it can be concluded that Sb forms the shallowest donor yet observed in ZnO based on the position of its excitonic transitions in the PL spectrum. Due to the high formation energy, it is unlikely for Sb to reside on the O site [101]. Electron emission channeling experiments by Wahl et al. [14] has confirmed that the Zn site is clearly preferred for Sb incorporation. It was previously shown by Johnston et al. [71] that As atoms also occupy Zn sites in ZnO. In general, large size group-V impurities in ZnO do not act like simple O-substituted acceptors. As a group-V impurity on the Zn site, Sb_{Zn} would be a triple donor with three positive charges on its ionized core. It is unlikely that such a highly charged defect would exist in isolation in ZnO, which is known to exhibit a variety of native charged defects.

Annealing experiments showed that the Sb-related transition reduces in intensity after annealing which might provide evidence to support the complex nature of this defect. A neutral donor could be produced by pairing Sb_{Zn} and some intrinsic defects in the crystal, such as a nearby Zn-site vacancy. Zn vacancies are known to be double acceptors in ZnO [11].

Limpijumnong et al. [101] proposed a model based on first principle calculations that Sb_{Zn} could induce two Zn vacancies in the lattice. They proposed that a triple donor paired with two double acceptors should result in a single acceptor, which was used to explain the origin of p-type in Sb-doped ZnO (fig. 5.15-(c)).

On the other hand we have proposed that pairing a triple donor with a single double

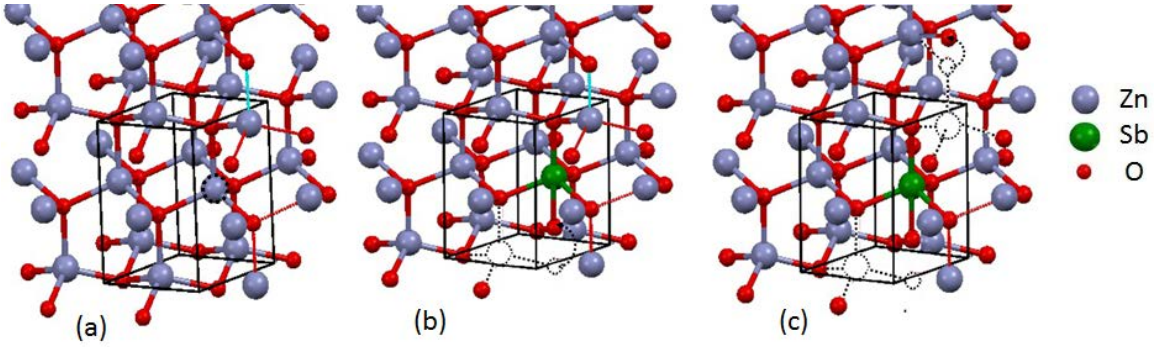

Figure 5.15: Schematic atomic structure of ZnO (a) without Sb impurity, (b) with Sb_{Zn}-V_{Zn} and (c) with Sb_{Zn}-$2V_{Zn}$ adapted from Ref. [101].

acceptor would result in a single donor [106]. In this picture the Sb atom can donate its three electrons and V_{Zn} can accept two electrons, forming Sb_{Zn}-V_{Zn} which acts like a donor. Fig. 5.15-(b) shows a schematic diagram of a possible Sb_{Zn}-V_{Zn} defect which could result in shallow donor behavior. Liu et al. [102] studied MBE grown Sb-doped ZnO and found that Sb can behave as a donor, leading to n-type conductivity. In order to verify the conductivity of our Sb doped ZnO NWs electrical measurements are required. In addition, it would be interesting to prepare Sb-doped samples using electron irradiation to investigate the role of Zn vacancies on the electrical and optical properties

5.4 Conclusion

Presented in this section are the results from PL and magneto PL measurements of the Sb doped ZnO NWs with a wide range of dopant concentrations. We have shown for the first time the formation of an Sb related D^0X transition at 3364.3 meV, which is the shallowest among the D^0X transitions so far observed in ZnO. This transition thermalizes in a manner similar to In and Ga D^0X transitions. It is unlikely that I_{Sb} belongs to excited state transitions (hole from B-valence band) because of its thermalization behavior. This also is confirmed by magneto PL results. Extrapolation of the D^+X binding energy vs. donor binding energy indicates that excitons should not bind to ionized Sb related donors in agreement with observation. Sb donor followed the Haynes rule despite the fact that it is not a substitutional donor like group-III donors in ZnO. However, its estimated binding energy is significantly smaller than the EMA energy. Similar behavior was reported previously for hydrogen related donors in ZnO [23].

Magneto PL measurements confirm that this transition is related to excitons bound to Sb related neutral donor centers and rules out the possibility that I_{Sb} is due to a A^0X transition. Our optical results support the recent electrical data of Liu et al., who showed an increase in electron concentration in Sb-doped ZnO thin films [102]. One possible form of the Sb-related complex can be a Sb_{Zn}-V_{Zn} pair which is expected to act as a single donor.

Chapter 6

Conclusion and Perspectives

6.1 Conclusion

We have investigated in detail the low temperature optical properties of ZnO NWs doped systematically with different impurities. In the study of group III impurities we investigated the effect of indium, aluminum and gallium doping on the optical and morphological properties of ZnO NWs over a wide range of doping concentrations using organometallic In, Al and Ga dopants. High-resolution PL spectra of D^0X transitions taken at 4.2 K revealed sharp linewidths (as low as 0.17 meV) and peak energies very close to those of bulk ZnO were obtained for lightly doped ZnO NWs, confirming the absence of substrate induced strain and revealing the high crystalline quality of the ZnO NWs. We have clearly identified the D^+X transitions of different dopants by intensity correlation with corresponding D^0X transitions. We revised the energy position of the Al related transition I_6^+ to 3373.1 meV in contrast with previous reports for bulk crystals. We also have identified the D^+X transition related to the I_7 line at 3372.5 meV. We clearly distinguished between the I_7 (at 3360.1 meV) and I_8 (at 3359.9 meV) transitions by careful doping of NWs with Ga.

We have clearly observed the evolution of TES transitions of the Al, Ga and In donors with increasing dopant concentrations. This allowed us to precisely estimate the donor binding energies. We have also identified phonon replicas of group III dopants unambiguously in our doped ZnO NWs.

At higher doping levels an asymmetric broadening in D^0X PL transition was observed with a tail at the lower energy side for group III dopants. We have developed a model based on the pairing of donor impurities in the shell region of the highly doped NWs to

explain this in Ga doped ZnO NWs. Based on our model we could estimate the donor concentration in ZnO NWs. Electrical transport measurements confirmed the increase in doping concentration.

PL studies of ZnO NWs co-doped with C and H at 4.2 K revealed four strong D^0X transitions, which we named as Z-lines and they dominated the excitonic PL intensity at high dopant concentrations. We showed that the presence of hydrogen as a co-dopant can greatly increase the PL intensity, but did not result in hydrogen related PL emission, I_4. PL studies on post annealed samples reveal that the Z-lines are stable even after heating at 900 °C, which argues against the possibility of H being one of the impurities in the complex. The observation of very intense green luminescence from these C and H co-doped NWs suggests the presence of Zn_i and O_v. We speculate that Z-lines are complexes containing carbon atoms with native defects, such as Zn_i and O_v. Two electron satellite transitions of these Z-lines were identified and used to estimate their donor binding energies. D^+X transitions of these Z-lines were also identified by correlation of PL intensity with the corresponding D^0X transitions.

Two distinct acceptors with binding energies of 133 ± 5 and 181 ± 5 meV are confirmed by varying the excitation power and temperature, and by time resolved measurements in carbon doped ZnO NWs. These binding energies are close to GaN:Mg acceptor binding energy, indicating that p-doping is at least in principle possible in ZnO. The 3236.7 meV peak is only observed in the presence of CCl_4 and is identified as a DAP transition corresponding to an acceptor binding energy of 181 ± 5 meV. The 3308.8 meV emission is the strongest in ZnO nanowires co-doped with CCl_4 and H_2 and is assigned to a previously reported (e,A^0) transition.

We have studied PL of unintentionally doped and Sn-doped ZnO single crystals grown by the chemical vapor transport method. Doped samples showed greatly increased emission from the I_{10} bound exciton transition that was recently proven to be related to the incorporation of Sn impurities based on radio-isotope studies [64]. Temperature dependent PL measurements of the I_{10} reveal a behavior that is similar to other shallow donors in ZnO. D^+X and TES transitions of the I_{10} transition are unambiguously identified and yield a donor binding energy of 71 meV. In contrast to Ge donors in ZnO, the binding energy for Sn follows the linear relation between binding and localization energies similar to group III donors confirming the shallow nature of this defect center which is attributed to a Sn_{Zn} double donor compensated by an unknown single acceptor such as Li or Na [23, 64].

Finally, PL and magneto PL measurements of Sb doped ZnO NWs with a wide range of dopant concentrations was studied in this work. We have shown for the first time the formation of an Sb related D^0X transition at 3364.3 meV, which is the shallowest among the D^0X transitions so far observed in ZnO[1]. This transition thermalizes in a way similar to group III donors. Extrapolation of D^+X binding energy vs. donor binding energy indicates that excitons will not bind to ionized Sb related donors. Sb donor followed the Haynes rule despite the fact that it is not a substitutional donor like group III donors in ZnO.

Magneto PL measurements confirm that this transition is related to excitons bound to Sb related neutral donor centers and rules out the possibility of I_{Sb} being due to A^0X transitions.

Estimated binding energies for group III and IV donors follow the empirical Haynes rule. The fact that the Sb related donor has a negative central cell correction is not explained. Previous reports have confirmed that Sn and Sb substitute for Zn sites in the ZnO lattice [14, 71, 97] and we have speculated that they make complexes with other defect impurities (Li and V_{Zn}, respectively) to compensate their charge. The fact that Sb and Sn have such widely different central cell corrections (negative vs strongly positive) argues to a fundamental difference in the nature of their compensating defects. Sn and Sb have many similarities with the group III donors, including obeying the same trend of D^0X binding energy vs. donor binding energy (Haynes rule) , as well as agreement between exciton localization energy and thermalization energies, in contrast to other less well understood defects such as Ge or the Y-line [38, 71].

6.2 Future work

In this thesis we primarily studied NWs grown by the MOVPE method. We grew very high quality crystals but high doping concentrations caused a change in the NWs morphology and also caused the PL intensity to drop which we concluded was due to carbon contamination. More studies should be done on the morphology change of the doped NWs as well as efforts to control their doping concentrations and reproducibility. It will be also useful to grow more uniformly undoped NWs and study the effect of the length and diameter size of the NWs on their PL spectra.

[1] concurrent with our report of this transition Cullen et al. [64] reported the same line in sample implanted with radioisotopes

We speculated on the nature of defects that could make complexes with Sb_{Zn} and Sn_{Zn} to make them donors. Electron irradiation and annealing experiments on Sb-doped ZnO NWs under different conditions, may provide more insight about the role of vacancies in the Sb donor complex by likely intentional generation of Zn vacancies. Atom probe tomography measurements is also another useful tool to investigate the Sb incorporation in Sb-doped NWs. Co-doping of Sn-doped samples with group I elements such as Li or Na could provide more information about the Sn donor complex.

Magneto PL experiments are a useful tool to identify the charge type of impurities in ZnO. Here we highlight the gaps not yet filled by previous Zeeman investigations in ZnO including Sn and carbon-doped samples to further investigate the I_{10}, I_{10}^{+}, Z-lines and their corresponding $D^{+}X$ transition.

PL excitation (PLE) spectroscopy with a tunable UV source is also another tool to give insight into the nature of the new defects found in this work. PLE could be used to identify the excited states (if any) of the Z-lines, Sb and Sn related transitions.

Time-resolved PL measurements would allow for further investigation of the new transitions (Z-lines and Sb) and would enable comparison with known group III transitions.

Micro or nano PL measurements on single NWs would give more insight into the uniformity of the doping distribution in the NWs.

More detailed electrical characterization is needed to verify the conductivity of the doped NWs and enable further improvements of their growth conditions to get high quality conductive NWs. Also, Seebeck measurement could be performed on single NWs that are suspected of being p-type (Sb doped, C-doped).

Bibliography

[1] K. Ellmer, A. Klein, and B. Rech. *Transparent conductive zinc oxide: basics and applications in thin film solar cells*, volume 104. Springer Science & Business Media, 2007.

[2] G. Perillat-Merceroz, F. Donatini, R. Thierry, P. Jouneau, P. Ferret, and G. Feuillet. Structural recovery of ion implanted ZnO nanowires. *J. Appl. Phys.*, 111(8):083524, 2012.

[3] C. Klingshirn, J. Fallert, H. Zhou, J. Sartor, C. Thiele, F. Maier-Flaig, D. Schneider, and H. Kalt. 65 years of ZnO research–old and very recent results. *Phys. Status Solidi (b)*, 247(6):1424–1447, 2010.

[4] Ü Özgür, Y. I. Alivov, C. Liu, A. Teke, M. Reshchikov, S. Doğan, V. Avrutin, S. J. Cho, and H. Morkoc. A comprehensive review of ZnO materials and devices. *J. Appl. Phys.*, 98(4):041301, 2005.

[5] C. F. Klingshirn, A. Waag, A. Hoffmann, and J. Geurts. *Zinc oxide: from fundamental properties towards novel applications*, volume 120. Springer Science & Business Media, 2010.

[6] D. G. Thomas. The exciton spectrum of zinc oxide. *J. Phys. Chem. Solids*, 15(1-2): 86–96, 1960.

[7] C. Merz, M. Kunzer, U. Kaufmann, I. Akasaki, and H. Amano. Free and bound excitons in thin wurtzite GaN layers on sapphire. *Semicond. Sci. Technol.*, 11(5):712, 1996.

[8] D. C. Look, J. W. Hemsky, and J. R. Sizelove. Residual native shallow donor in ZnO. *Phys. Rev. Lett.*, 82(12):2552, 1999.

[9] C. G. Van de Walle. Defect analysis and engineering in ZnO. *Physica B: Condensed Matter*, 308:899–903, 2001.

[10] A. Janotti and C. G. Van de Walle. Oxygen vacancies in ZnO. *Appl. Phys. Lett.*, 87 (12):122102, 2005.

[11] X. J. Wang, L. S. Vlasenko, S. J. Pearton, W. M. Chen, and I. A. Buyanova. Oxygen and zinc vacancies in as-grown ZnO single crystals. *J. Phys. D: Appl. Phys.*, 42(17): 175411, 2009.

[12] J. Sann, J. Stehr, A. Hofstaetter, D. M. Hofmann, A. Neumann, M. Lerch, U. Haboeck, A. Hoffmann, and C. Thomsen. Zn interstitial related donors in ammonia-treated ZnO powders. *Phys. Rev. B: Condens. Matt.*, 76(19):195203, 2007.

[13] K. Johnston, M. O. Henry, D. McCabe, E. McGlynn, M. Dietrich, E. Alves, and M. Xia. Identification of donor-related impurities in ZnO using photoluminescence and radiotracer techniques. *Phys. Rev. B*, 73(16):165212, 2006.

[14] U. Wahl, J. G. Correia, T. Mendonça, and S. Decoster. Direct evidence for Sb as a Zn site impurity in ZnO. *Appl. Phys. Lett.*, 94(26), 2009.

[15] U. Wahl, E. Rita, J. G. Correia, A. C. Marques, E. Alves, and J. C. Soares. Direct evidence for As as a Zn-site impurity in ZnO. *Phys. Rev. Lett.*, 95(21):215503, 2005.

[16] S. Lautenschlaeger, S. Eisermann, G. Haas, E. A. Zolnowski, M. N. Hofmann, A. Laufer, M. Pinnisch, B. K. Meyer, M. R. Wagner, J. S. Reparaz, et al. *Phys. Rev. B*, 85(23):235204, 2012.

[17] A. Zeuner, H. Alves, J. Sann, W. Kriegseis, C. Neumann, D. M. Hofmann, B. K. Meyer, A. Hoffmann, U. Haboeck, M. Straßburg, et al. In *Phys. Status. Solidi C*, number 4, 2004.

[18] F. Reuss, C. Kirchner, T. Gruber, R. Kling, S. Maschek, W. Limmer, A. Waag, and P. Ziemann. Optical investigations on the annealing behavior of gallium-and nitrogen-implanted ZnO. *J. Appl. Phys.*, 95(7):3385–3390, 2004.

[19] N. Hanèche, A. Lusson, C. Sartel, A. Marzouki, V. Sallet, M. Oueslati, F. Jomard, and P. Galtier. Optical characterization of nitrogen-and antimony-doped ZnO thin layers grown by MOVPE. *Phys. Status Solidi (b)*, 247(7):1671–1674, 2010.

[20] J. L. Lyons, A. Janotti, and C. G. Van de Walle. Why nitrogen cannot lead to p-type conductivity in ZnO. *Appl. Phys. Lett.*, 95(25):252105, 2009.

[21] D. F. Croxall, R. Ward, C. A. Wallace, and R. C. Kell. Hydrothermal growth and investigation of Li-doped zinc oxide crystals of high purity and perfection. *J. Cryst. Growth*, 22(2):117–124, 1974.

[22] Y. Chen, D. M. Bagnall, H. Koh, K. Park, K. Hiraga, Z. Zhu, and T. Yao. Plasma assisted molecular beam epitaxy of ZnO on c-plane sapphire: growth and characterization. *J. Appl. Phys.*, 84(7):3912–3918, 1998.

[23] B. K. Meyer, H. Alves, D. M. Hofmann, W. Kriegseis, D. Forster, F. Bertram, J. Christen, A. Hoffmann, M. Straßburg, M. Dworzak, et al. Bound exciton and donor-acceptor pair recombinations in ZnO. *Phys. Status Solidi B-Basic Research*, 241(2): 227–230, 2004.

[24] A. V. Rodina, M. Strassburg, M. Dworzak, U. Haboeck, A. Hoffmann, A. Zeuner, H. R. Alves, D. M. Hofmann, and B. K. Meyer. Magneto-optical properties of bound excitons in ZnO. *Phys. Rev. B*, 69(12):125206, 2004.

[25] D. C. Reynolds, D. C. Look, B. Jogai, C. W. Litton, T. C. Collins, M. T. Harris, M. J. Callahan, and J. S. Bailey. Strain splitting of the Γ5 and Γ6 free excitons in ZnO. *J. Appl. Phys.*, 86(10):5598–5600, 1999.

[26] M. R. Wagner, H. W. Kunert, A. Machatine, A. Hoffmann, P. Niyongabo, J. Malherbe, and J. Barnas. Bound and free excitons in ZnO. optical selection rules in the absence and presence of time reversal symmetry. *Microelectron. J.*, 40(2):289–292, 2009.

[27] C. F. Klingshirn. *Semiconductor optics*. Springer Science & Business Media, 2012.

[28] V. Heine. *Group theory in quantum mechanics: an introduction to its present usage*. Courier Corporation, 2007.

[29] W. R. Lambrecht, A. V. Rodina, S. Limpijumnong, B. Segall, and B. K. Meyer. Valence-band ordering and magneto-optic exciton fine structure in ZnO. *Phys. Rev. B*, 65(7):075207, 2002.

[30] B. K. Meyer, J. Sann, S. Lautenschläger, M. R. Wagner, and A. Hoffmann. Ionized and neutral donor-bound excitons in ZnO. *Phys. Rev. B*, 76(18):184120, 2007.

[31] D. C. Look, D. C. Reynolds, C. W. Litton, R. L. Jones, D. B. Eason, and G. Cantwell. *Appl. Phys. Lett.*, 81(10):1830–1832, 2002.

[32] A. Tsukazaki, A. Ohtomo, T. Onuma, M. Ohtani, T. Makino, M. Sumiya, K. Ohtani, Shigefusa F. Chichibu, S. Fuke, Y. Segawa, et al. Repeated temperature modulation epitaxy for p-type doping and light-emitting diode based on ZnO. *Nat. Mater.*, 4(1): 42–46, 2005.

[33] E. Przeździecka, E. Kamińska, I. Pasternak, A. Piotrowska, and J. Kossut. Photoluminescence study of p-type ZnO: Sb prepared by thermal oxidation of the Zn-Sb starting material. *Phys. Rev. B*, 76(19):193303, 2007.

[34] D. C. Reynolds, C. W. Litton, and T. C. Collins. Zeeman effects in the edge emission and absorption of ZnO. *Phys. Rev.*, 140(5A):A1726, 1965.

[35] S. Muller, D. Stichtenoth, M. Uhrmacher, H. Hofsass, C. Ronning, and J. Roder. Unambiguous identification of the PL-I_9 line in zinc oxide. *Appl. Phys. Lett.*, 90(1): 12107–12107, 2007.

[36] M. Schilling, R. Helbig, and G. Pensl. Bound exciton luminescence of Ar- and Al-implanted ZnO. *J. Lumin.*, 33(2):201–212, 1985.

[37] J. R. Haynes. Experimental proof of the existence of a new electronic complex in silicon. *Phys. Rev. Lett.*, 4(7):361, 1960.

[38] M. R. Wagner, G. Callsen, J. S. Reparaz, J. Schulze, R. Kirste, M. Cobet, I. A. Ostapenko, S. Rodt, C. Nenstiel, M. Kaiser, et al. Bound excitons in ZnO: Structural defect complexes versus shallow impurity centers. *Phys. Rev. B*, 84(3):035313, 2011.

[39] Y. P. Varshni. Temperature dependence of the energy gap in semiconductors. *Physica*, 34(1):149–154, 1967.

[40] L. Wang and N. C. Giles. Temperature dependence of the free-exciton transition energy in zinc oxide by photoluminescence excitation spectroscopy. *J. Appl. Phys.*, 94:973–978, 2003.

[41] K. W. Liu, M. Sakurai, and M. Aono. Indium-doped ZnO nanowires: Optical properties and room-temperature ferromagnetism. *Journal of Applied Physics*, 108(4): 043516, 2010.

[42] K. Thonke, T. h. Gruber, N. Teofilov, R. Schönfelder, A. Waag, and R. Sauer. *Physica B: Condensed Matter*, 308:945–948, 2001.

[43] A. Zeuner, H. Alves, D. M. Hofmann, B. K. Meyer, A. Hoffmann, U. Haboeck, M. Strassburg, and M. Dworzak. *Phys. Status Solidi B*, 234(3):R7–R9, 2002.

[44] J. Fallert, R. Hauschild, F. Stelzl, A. Urban, M. Wissinger, H. Zhou, C. Klingshirn, and H. Kalt. Surface-state related luminescence in ZnO nanocrystals. *J. Appl. Phys.*, 101(7):073506, 2007.

[45] M. Schirra, R. Schneider, A. Reiser, G. M. Prinz, M. Feneberg, J. Biskupek, U. Kaiser, C. E. Krill, K. Thonke, and R. Sauer. *Phys. Rev. B*, 77(12):125215, 2008.

[46] D. Bimberg, M. Sondergeld, and E. Grobe. Thermal dissociation of excitons bound to neutral acceptors in high-purity GaAs. *Phy. Rev. B*, 4(10):3451, 1971.

[47] D. Block, A. Herve, and R. T. Cox. Optically detected magnetic resonance and optically detected endor of shallow indium donors in ZnO. *Phys. Rev. B*, 25(9):6049, 1982.

[48] D. M. Hofmann, A. Hofstaetter, F. Leiter, H. Zhou, F. Henecker, B. K. Meyer, S. B. Orlinskii, J. Schmidt, and P. G. Baranov. Hydrogen: a relevant shallow donor in zinc oxide. *Phys. Rev. Lett.*, 88(4):045504, 2002.

[49] D. G. Thomas and J. J. Hopfield. Optical properties of bound exciton complexes in cadmium sulfide. *Phys. Rev.*, 128(5):2135, 1962.

[50] D. G. Thomas and J. J. Hopfield. Bound exciton complexes. *Phys. Rev. Lett.*, 7(8): 316, 1961.

[51] The photomultiplier tube. URL `https://commons.wikimedia.org/wiki/File:Photomultipliertube.svg`.

[52] C. F. Brucker, T. W. McDaniel, and M. C. Gupta. Handbook of photonics, 1997.

[53] W. I. Park, Y. H. Jun, S. W. Jung, and G. C. Yi. Excitonic emissions observed in ZnO single crystal nanorods. *Appl. Phys. Lett.*, 82(6):964–966, 2003.

[54] J. Zhong, S. Muthukumar, Y. Chen, Y. Lu, H. Ng, W. Jiang, and E. L. Garfunkel. Ga-doped ZnO single-crystal nanotips grown on fused silica by metalorganic chemical vapor deposition. *Appl. Phys. Lett.*, 83(16):3401–3403, 2003.

[55] S. Lin, H. He, Z. Ye, B. Zhao, and J. Huang. Temperature-dependent photoluminescence and photoluminescence excitation of aluminum monodoped and aluminum-indium dual-doped ZnO nanorods. *J. Appl. Phys.*, 104(11):114307, 2008.

[56] C. W. Heitsch. New evidence for free aih. *Nature*, 195:995–996, 1962.

[57] W. I. Park. Controlled synthesis and properties of ZnO nanostructures grown by metalorganic chemical vapor deposition: A review. *Met. Mater. Int.*, 14(6):659–665, 2008.

[58] M. R. Wagner, T. P. Bartel, R. Kirste, A. Hoffmann, J. Sann, S. Lautenschläger, B. K. Meyer, and C. Kisielowski. Influence of substrate surface polarity on homoepitaxial growth of ZnO layers by chemical vapor deposition. *Phys. Rev. B*, 79(3):035307, 2009.

[59] K. Narita. A model for exciton bound to a donor pair in silicon. *Solid State Commun.*, 29(3):299–301, 1979.

[60] B. K. Meyer, J. Sann, S. Eisermann, S. Lautenschlaeger, M. R. Wagner, M. Kaiser, G. Callsen, J. S. Reparaz, and A. Hoffmann. Excited state properties of donor bound excitons in ZnO. *Phys. Rev. B*, 82(11):115207, 2010.

[61] Michel Lannoo. *Point defects in semiconductors I: theoretical aspects*, volume 22. Springer Science & Business Media, 2012.

[62] H. Alves, D. Pfisterer, A. Zeuner, T. Riemann, J. Christen, D. M. Hofmann, and B. K. Meyer. Optical investigations on excitons bound to impurities and dislocations in ZnO. *Optical Materials*, 23(1):33–37, 2003.

[63] B. K. Meyer, J. Sann, D. M. Hofmann, C. Neumann, and A. Zeuner. Shallow donors and acceptors in ZnO. *Semicond. Sci. Technol.*, 20(4):S62, 2005.

[64] J. Cullen, D. Byrne, K. Johnston, E. McGlynn, and M. O. Henry. Chemical identification of luminescence due to Sn and Sb in ZnO. *Appl. Phys. Lett.*, 102(19):192110, 2013.

[65] J. Cullen, K. Johnston, E. McGlynn, M. O. Henry, D. Dunker, D. R. Yakovlev, and M. Bayer. Uniaxial stress and Zeeman spectroscopy of the 3.324 ev Ge-related photoluminescence in ZnO. *Phys. Rev. B*, 87(16):165202, 2013.

[66] S. Tan, X. Sun, Z. Yu, P. Wu, G. Lo, and D. Kwong. p-type conduction in unintentional carbon-doped ZnO thin films. *Appl. Phys. Lett.*, 91(7):072101, 2007.

[67] K. Tang, S. Gu, S. Zhu, J. Liu, H. Chen, J. Ye, R. Zhang, and Y. Zheng. Suppression of compensation from nitrogen and carbon related defects for p-type N-doped ZnO. *Appl. Phys. Lett.*, 95(19):192106, 2009.

[68] N. H. Nickel, F. Friedrich, J. F. Rommeluère, and P. Galtier. Vibrational spectroscopy of undoped and nitrogen-doped ZnO grown by metalorganic chemical vapor deposition. *Appl. Phys. Lett.*, 87(21):1905, 2005.

[69] J. L. Lyons, D. Steiauf, A. Janotti, and C. G. Van de Walle. Carbon as a shallow donor in transparent conducting oxides. *Physical Review Applied*, 2(6):064005, 2014.

[70] Joon Won Park, Dong Hak Kim, Suk-Ho Choi, MC Lee, and D Lim. The role of carbon doping in ZnO. *J. Korean Phys. Soc.*, 57(6):1482–1485, 2010.

[71] K. Johnston, J. Cullen, M. O. Henry, E. McGlynn, and M. Stachura. Evidence for As lattice location and Ge bound exciton luminescence in ZnO implanted with As 73 and Ge 73. *Phys. Rev. B*, 83(12):125205, 2011.

[72] S. Kim, D. K. Lee, S. H. Hong, S. H. Eom, H. T. Oh, S. Choi, H. N. Hwang, and C. C. Hwang. High-efficient ultraviolet emission in phonon-reduced ZnO films: The role of germanium. *J. Appl. Phys.*, 103(2):3514, 2008.

[73] D. H. Fan, Z. Y. Ning, and M. F. Jiang. Characteristics and luminescence of Ge doped ZnO films prepared by alternate radio frequency magnetron sputtering. *Appl. Surf. Sci.*, 245(1):414–419, 2005.

[74] T. Zheng, Z. Li, J. Chen, K. Shen, and K. Sun. Transitions of microstructure and photoluminescence properties of the Ge/ZnO multilayer films in certain annealing temperature region. *Appl. Surf. Sci.*, 252(24):8482–8486, 2006.

[75] A. K. Das, P. Misra, and L. M. Kukreja. Effect of Si doping on electrical and optical properties of ZnO thin films grown by sequential pulsed laser deposition. *J. Phys. D: Appl. Phys.*, 42(16):165405, 2009.

[76] S. Lautenschlaeger, J. Sann, N. Volbers, B. K. Meyer, A. Hoffmann, U. Haboeck, and M. R. Wagner. Asymmetry in the excitonic recombinations and impurity incorporation of the two polar faces of homoepitaxially grown ZnO films. *Phys. Rev. B*, 77(14): 144108, 2008.

[77] M. R. Wagner, J. Schulze, R. Kirste, M. Cobet, A. Hoffmann, C. Rauch, A. V. Rodina, B. K. Meyer, U. Röder, and K. Thonke. Γ 7 valence band symmetry related hole fine splitting of bound excitons in ZnO observed in magneto-optical studies. *Phys. Rev. B*, 80(20):205203, 2009.

[78] E. V. Lavrov, F. Herklotz, and J. Weber. Identification of two hydrogen donors in ZnO. *Phys. Rev. B*, 79(16):165210, 2009.

[79] Suk-Ho Choi, D. Lim, J. W. Park, D. H. Kim, and M. Lee. The role of carbon doping in ZnO. *J. Korean Phys. Soc.*, 57:1482, 2010.

[80] J. G. Liu, S. L. Gu, S. M. Zhu, K. Tang, X. D. Liu, H. Chen, and Y. D. Zheng. The influences of O/Zn ratio and growth temperature on carbon impurity incorporation in ZnO grown by metal-organic chemical vapor deposition. *Journal of Crystal Growth*, 312(19):2710–2717, 2010.

[81] Gary G DeLeo, W Beall Fowler, and George D Watkins. Electronic structure of hydrogen-and alkali-metal-vacancy complexes in silicon. *Physical Review B*, 29(4): 1819, 1984.

[82] C. G. Van de Walle. Hydrogen as a cause of doping in zinc oxide. *Phys. Rev. Lett.*, 85(5):1012, 2000.

[83] A. Janotti and C. G. Van de Walle. Hydrogen multicentre bonds. *Nat. Mater.*, 6(1): 44–47, 2007.

[84] Z. Zhang, D. C. Look, R. Schifano, K. M. Johansen, B. G. Svensson, and L. J. Brillson. Process dependence of H passivation and doping in H-implanted ZnO. *J. Phys. D: Appl. Phys.*, 46(5):055107, 2013.

[85] P. H. Kasai. Electron spin resonance studies of donors and acceptors in ZnO. *Phys. Rev.*, 130(3):989, 1963.

[86] G. Xiong, K. B. Ucer, R. T. Williams, J. Lee, D. Bhattacharyya, J. Metson, and P. Evans. Donor-acceptor pair luminescence of nitrogen-implanted ZnO single crystal. *J. Appl. Phys.*, 97(4):043528, 2005.

[87] D. G. Thomas, J. J. Hopfield, and W. M. Augustyniak. *Phys. Rev.*, 140(1A):A202, 1965.

[88] E. Zacks and A. Halperin. *Phys. Rev. B*, 6(8):3072, 1972.

[89] F. Mohammadbeigi, E. S. Kumar, S. Alagha, I. P. Anderson, and S. P. Watkins. *J. Appl. Phys.*, 116(5):053516, 2014.

[90] S. Jianfeng, T. Chunjuan, N. Qiang, W. Changqing, and F. Zhuxi. Variation of N acceptor energy induced by Al–N codoping in ZnO films. *J. Alloys Compd.*, 500(1): 5–8, 2010.

[91] M. Schirra, R. Schneider, A. Reiser, G. M. Prinz, M. Feneberg, J. Biskupek, U. Kaiser, C. E. Krill, R. Sauer, and K. Thonke. Acceptor-related luminescence at 3.314 eV in zinc oxide confined to crystallographic line defects. *Physica B: Condensed Matter*, 401:362–365, 2007.

[92] D. Tainoff, B. Masenelli, P. Mélinon, A. Belsky, G. Ledoux, D. Amans, C. Dujardin, N. Fedorov, and P. Martin. Competition between exciton-phonon interaction and defects states in the 3.31 ev band in ZnO. *Phys. Rev. B*, 81(11):115304, 2010.

[93] I. Pelant and J. Valenta. *Luminescence spectroscopy of semiconductors*. Oxford University Press, 2012.

[94] S Strauf, SM Ulrich, P Michler, J Gutowski, T Böttcher, S Figge, S Einfeldt, and D Hommel. Analysis of time-resolved donor-acceptor-pair recombination in MBE and MOVPE grown GaN: Mg. *Phys. Status Solidi B-Basic Research*, 228(1/2):379–383, 2001.

[95] P. Bäume, S. Strauf, J. Gutowski, M. Behringer, and D. Hommel. Analysis of time-resolved donor-acceptor-pair spectra of ZnSe: Li and ZnSe: N. *J. Cryst. Growth*, 184: 531–535, 1998.

[96] Z. N. Urgessa, J. R. Botha, M. O. Eriksson, C. M. Mbulanga, S. R. Dobson, S. T. Djiokap, K. F. Karlsson, V. Khranovskyy, R. Yakimova, and P. Holtz. Low temperature near band edge recombination dynamics in ZnO nanorods. *J. Appl. Phys.*, 116 (12):123506, 2014.

[97] E. Rita, E. Alves, U. Wahl, J. G. Correia, A. J. Neves, M. J. Soares, and T. Monteiro. Optical doping of ZnO with Tm by ion implantation. *Physica B: Condensed Matter*, 340:235–239, 2003.

[98] C. D. Corolewski, N. S. Parmar, K. G. Lynn, and M. D. McCluskey. Hydrogen-related complexes in Li-diffused ZnO single crystals. *J. Appl. Phys.*, 120(3), 2016.

[99] L. Vina, S. Logothetidis, and M. Cardona. Temperature dependence of the dielectric function of germanium. *Phys. Rev. B*, 30(4):1979, 1984.

[100] J. L. Lyons, A. Janotti, and C. G. Van de Walle. Why nitrogen cannot lead to p-type conductivity in ZnO. *Appl. Phys. Lett.*, 95(25):252105, 2009.

[101] S. Limpijumnong, S. Zhang, S. Wei, and C. Park. Doping by large-size-mismatched impurities: the microscopic origin of arsenic-or antimony-doped p-type zinc oxide. *Phys. Rev. Lett.*, 92(15):155504, 2004.

[102] H. Liu, N. Izyumskaya, V. Avrutin, Ü. Özgür, A. B. Yankovich, A. V. Kvit, P. M. Voyles, and H. Morkoç. Donor behavior of Sb in ZnO. *Journal of Applied Physics*, 112(3):033706, 2012.

[103] M. Strassburg, A. Rodina, M. Dworzak, U. Haboeck, I. L. Krestnikov, A. Hoffmann, O. Gelhausen, M. R. Phillips, H. R. Alves, A. Zeuner, et al. Identification of bound exciton complexes in ZnO. *Phys. Status Solidi (b)*, 241(3):607–611, 2004.

[104] H. Jiang. *III-Nitride Semiconductors: Optical Properties*, volume 1. CRC Press, 2002.

[105] L. Ding, B. K. Li, H. T. He, W. K. Ge, J. N. Wang, J. Q. Ning, X. M. Dai, C. C. Ling, and S. J. Xu. Classification of bound exciton complexes in bulk ZnO by magnetophotoluminescence spectroscopy. *J. Appl. Phys.*, 105(5):053511, 2009.

[106] E. S. Kumar, F. Mohammadbeigi, S. Alagha, Z. Deng, I. P. Anderson, T. Wintschel, and S. P. Watkins. Optical evidence for donor behavior of Sb in ZnO nanowires. *Appl. Phys. Lett.*, 102(13):132105, 2013.

[107] G. Fanchini, A. Tagliaferro, G. Messina, S. Santangelo, A. Paoletti, and A. Tucciarone. Vibrational properties and microstructure of reactively sputtered hydrogenated carbon nitrides. *J. Appl. Phys.*, 91:1155–1165, 2002.

Appendix A

Growth Information

Table **??** provides a summary of the growth information of the samples studied in this thesis. The units of flow rates are in standard cubic centimeter per minute (sccm) and nmol/min for all dopants except hydrogen and Sn.

Details of growth information of different samples studied in this thesis.

Sample#	Doping	Flow (sccm)	Flow (nmol/min)	Bubbler T (^{o}C)	Bubbler P (Torr)	Zn Bubbler T,P (^{o}C,Torr)	Mole ratio (cm^{-3}) (gas phase)
H515	undoped	-	-	-	-	-5,1600	-
H529	Al	2	-	-	-	-5,1600	-
H530	Al	5	-	-	-	-5,1600	-
H531	Al	10	-	-	-	-5,1600	-
H532	Al	20	-	-	-	-5,1600	-
H806	undoped	-	-	-	-	-20,800	-
H831	Ga	2	0.007	-80	1600	-20,800	2.6E+16
H832	Ga	5	0.02	-80	1600	-20,800	8.3E+16
H835	Ga	20	0.07	-80	1600	-20,800	2.6E+17
H836	Ga	50	0.16	-80	1600	-20,800	7.5E+17
H839	Ga	100	0.32	-80	1600	-20,800	1.1E+18
H841	Ga	200	0.64	-80	1600	-20,800	2.2E+18
H454	undoped	-	-	-	-	-5,1600	-
H456	In	5	1	-40.7	800	-5,1600	1.5E+19
H457	In	20	4.4	-40.7	800	-5,1600	6.5E+19
H413	In	2	21	-5	800	-5,1600	3.1E+20
H414	In	5	53	-5	800	-5,1600	7.8E+20
H416	In	10	106	-5	800	-5,1600	1.6E+21
H417	In	20	213	-5	800	-5,1600	3.1E+21
H778	undoped	-	-	-	-	-20,800	-
H779	C	2	0.008	-	-	-20,800	-
H780	C	5	0.06	-	-	-20,800	-
H781	C	10	0.25	-	-	-20,800	-
H782	C	20	1.25	-	-	-20,800	-
H794	C,H	10,2	0.25	-	-	-20,800	-
H795	C,H	10,10	0.25	-	-	-20,800	-
H796	C,H	10,50	0.25	-	-	-20,800	-
H823	C,H	25,50	2.3	-	-	-20,800	-
H798	C,H	40,50	10	-	-	-20,800	-
H821	C,H	47,50	30	-	-	-20,800	-
H800	C,H	50,50	50	-	-	-20,800	-
A	undoped	-	-	-	-	CVT	-
B	Sn	-	-	-	-	CVT	-
C	Sn	-	-	-	-	CVT	-
D	Sn	-	-	-	-	CVT	-
E	Sn	-	-	-	-	CVT	-
H459	undoped	-	-	-	-	-5,1600	-
H460	Sb	2	3.8	-80	1950	-5,1600	5.6E+20
H461	Sb	5	9.6	-80	1950	-5,1600	1.4E+21
H462	Sb	10	19.1	-80	1950	-5,1600	2.8E+21
H463	Sb	20	38.2	-80	1950	-5,1600	5.6E+21
H464	Sb	50	76.4	-80	1950	-5,1600	1.1E+22
H465	Sb	2	123	-40	1950	-5,1600	1.8E+22
H466	Sb	5	307	-40	1950	-5,1600	4.5E+22

Appendix B

Raman Spectra

Room temperature Raman measurements were performed in a back-scattering geometry. Spectra were excited using the 514.4 nm line of an Ar-ion laser with a power of 30 μW focused on the NWs. The spot size was 0.5 μm.
Two broad vibrational modes related to carbon sp^2 clusters at 1356 and 1598 cm^{-1} were observed. These modes are known as carbon D and G modes.[107] As seen in Fig. **??** increasing the carbon doping concentration increases the intensity of these modes increase in the Raman spectra. Fig. **??** shows how adding hydrogen to the carbon-doped samples during the growth affects the Raman spectra. As seen in this figure the D and G modes are eliminated from the Raman spectrum of the carbon and hydrogen co-doped ZnO NWs.
Fig. **??** shows the Raman spectra of undoped and highly Sb-doped ZnO NWs. As mentioned in chapter 5, high Sb dopant concentrations led to a loss of PL intensity which was attributed to carbon point defects. The Raman spectra also shows the emerging of carbon related D and G modes in highly Sb doped samples.

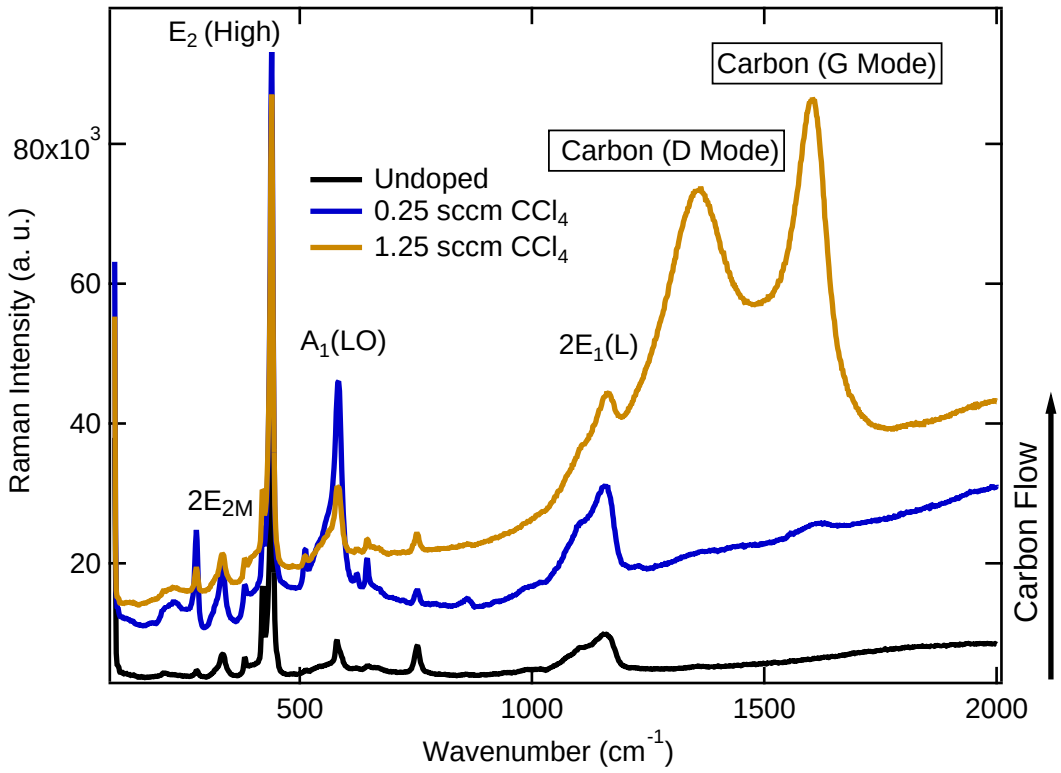

Effect of carbon doping on the room temperature Raman spectra of ZnO NWs.

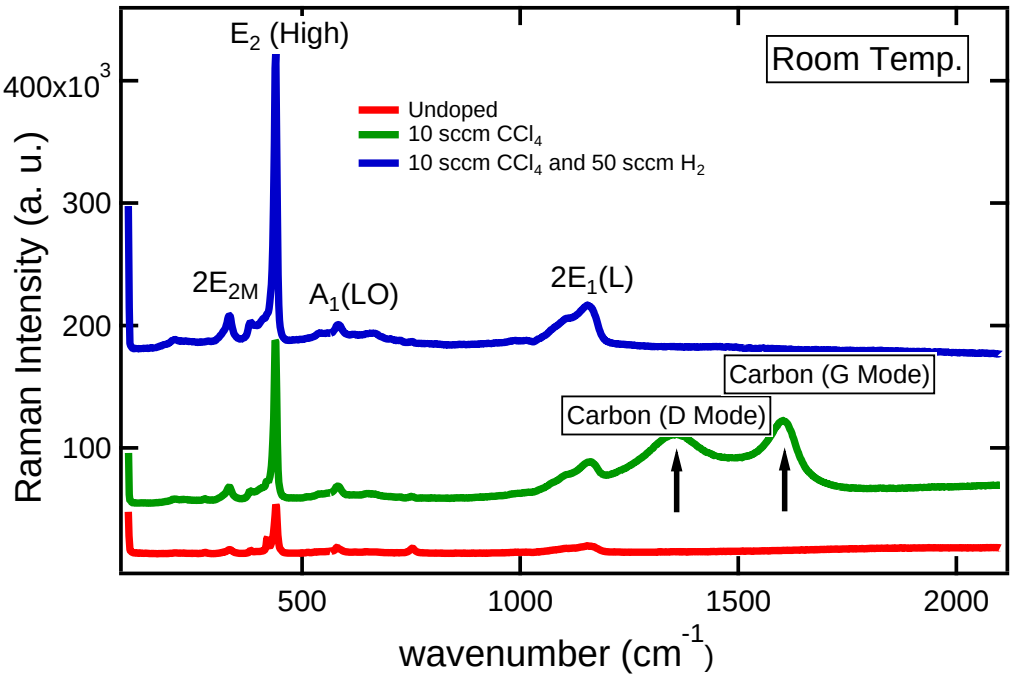

Room temperature Raman spectra of undoped and carbon/hydrogen doped ZnO NWs.

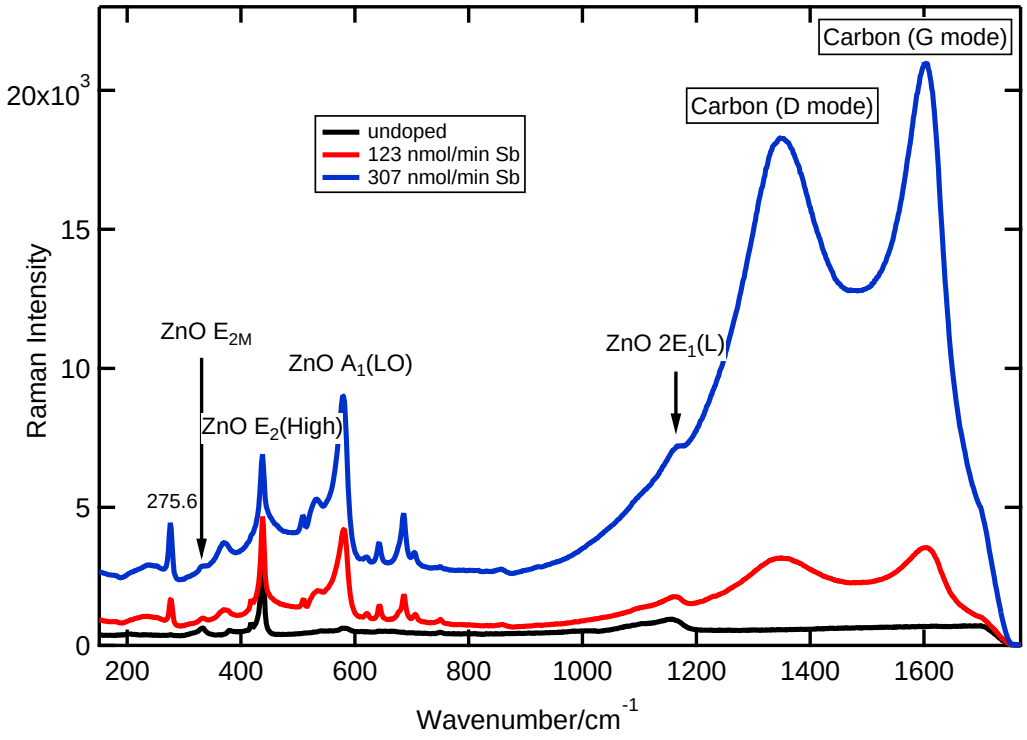

Room temperature Raman spectra of undoped and Sb doped ZnO NWs.

Appendix C

Thermalization Behavior

Fig. **??** shows the integrated PL intensity versus inverse temperature for Z_2 and Z_3 transitions of carbon and hydrogen-doped ZnO NWs. The fits have been done using Eq. 1.7. For more details see section 4.2.3.

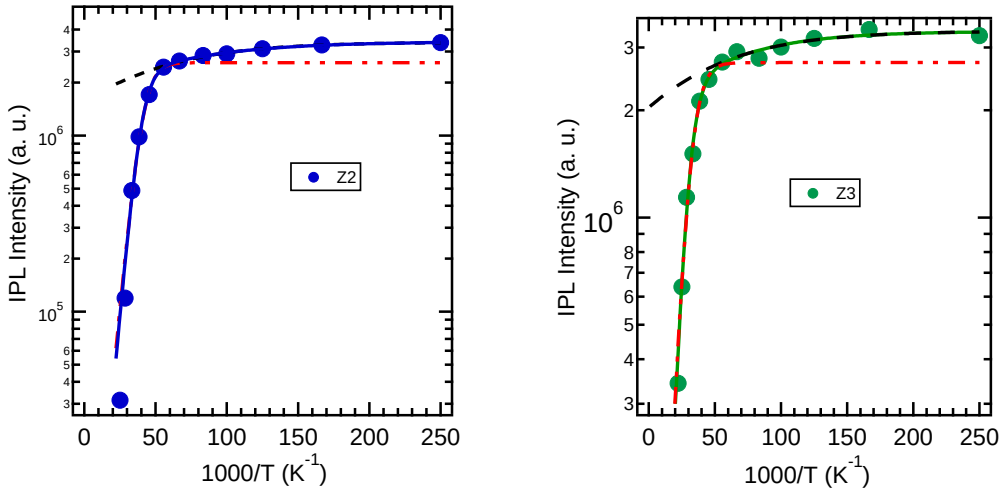

Temperature-dependent PL data and fits for Z_2 and Z_3 lines.

A summary of activation energies for Z_2 and Z_3 lines.

transition	energy (meV)	E_{a1} (meV)	E_{a2} (meV)
Z_2	3361.2	1.5 ± 0.3	17.7 ± 1.3
Z_3	3361.7	1.7 ± 0.8	16.9 ± 2.4